Detonation Equation of State at LLNL, 1993

P. C. Souers and L. C. Haselman, Jr.

Energetic Materials Center
Lawrence Livermore National Laboratory
March 1, 1994

DISCLAIMER

DISCLAIMER

Portions of this document may be illegible in electronic image products. Images are produced from the best available original document.

Table of Contents

Summary

1. Conclusions

Our conclusions, based on the available data, are as follows.

1. Careful terminology regarding detonation points is needed. We distinguish between the spike pressure (P_k), the measured jump-off or supracompression pressure (P_p), the Cylinder Test JWL pressure (P_j), the adiabat pressure (P_a), the Chapman-Jouget (C-J) pressure (P_{cj}), and the sonic point pressure (P_n). The C-J pressure requires true thermodynamic equilibrium and may exist only in a thermochemical code. The adiabat pressure is the actual nonequilibrium start of the Principal Adiabat in an explosive of infinite size and at steady state. The sonic pressure is the start of an adiabat for an explosive neither at infinite size nor at steady state. At present, the term "C-J" covers all of these pressures in an indiscriminate way.

2. The low-effort method of deriving cylinder JWLs using PETN as the standard plus three to five smoothed data points from the unknown explosive works within the accuracy of data obtained from the streak camera. However, Fabry-Perot interferometry is at all times during the shot more accurate for velocities than is the streak camera—Fabry data, therefore, should be taken to long times. Nonetheless, the streak camera will always be valuable as an record of the distance. The ratio of the two methods is a good measurement of the overall validity of the shot.

3. The homogeneous explosives run with the LLNL cylinder method produces total detonation energies in agreement of $1 \pm 4\%$ with calorimetric experiment.

4. The LLNL Cylinder JWL equation of state (EOS) contains two important assumptions: (1) the energy of detonation at a given volume is nearly constant for a wide variety of JWL parameters and (2) the kinetic and detonation energies have the same proportionality for all explosives. A simple cylinder model suggests that the first assumption is good to $\pm 2\%$ for $1 < v < 0$ for velocities known to ± 0.015 mm/μs. The second assumption is probably correct within a few percent as shown by near-constant, cylinder wall-pushing efficiencies.

5. The JWL formalism provides different answers according to how the coefficients are derived; no correlation is evident among the resulting constants. The Urtiew / Hayes proposal to set A, B, and C proportional to $\rho_o D^2$,

and at the same time, confine the other constants appears unsuccessful. The use of a look-up table for describing the adiabats is a possible solution, but these tables have not been calibrated across different experiments.

The same plate velocity data have a scatter of ± 0.02 mm/μs according to where the data were found and how they were processed. This means that returning to a few good experiments with better statistical methods will be necessary to calibrate the JWLs more accurately.

6. Detonation pressure measurements (in GPa) for five, often-run explosives have been collected from various sources and are compared as follows:

	1-D plate, P_p		Cylinder			
	Jump-off velocity	Supra-compress	Jump-off velocity, P_p	Three-point, JWL fit, P_j	Haselman compression, P_p	TIGER BKWR P_{cj}
LX-14	35 ± 2		37 ± 3	38 ± 2	36	35
PBX-9404	39 ± 2	38 ± 2	34 ± 5	38 ± 2	37 to 39	36
PETN	32 ± 4	31 ± 2	$31^* \pm 3$	32 ± 2		31
RX-26-AF		34 ± 2	36 ± 2	34 ± 2	32.5	32
LX-17	34	32 ± 2	32 ± 4	26 ± 1	30	27

a. PETN, with an adiabat pressure determined by supracompression as 31 ± 2 GPa, is a good standard explosive. The C-J–derived relation $\partial U_s/\partial u_p \longrightarrow 0$ was seen in this case.

b. Detonation pressures for LX-14 and PBX-9404 are consistent by all sources. TIGER is always low in its calculation.

c. LX-17 has a low, 26- to 27-GPa adiabat pressure as given by the Cylinder Test and the Ignition & Growth model. The larger detonation pressure seen in plates may be caused by a failure of the impedance-match equation.

d. For three explosives, $\partial U_s/\partial u_p$ did not approach zero in supracompression. Nonequlibrium behavior with an absence of the C-J condition is a possible reason.

7. The most accurately measurable quantity, after the detonation velocity, is the total detonation energy. Continued detonation calorimetry is important.

8. The percent of cylinder detonation energy that appears as the kinetic energy of wall motion is proportional to the cylinder pressure/ energy ratio (P_j/E_o). The JWL detonation volume (v_j), is inversely proportional to P_j/E_o so that more efficient explosives push back with heated gaseous products. The spring constant for the pushing back is $\rho_o D^2$.

9. The TIGER thermochemical code predicts absolute detonation energies only to ±10% for homogeneous explosives at a given relative volume. The total detonation energies may be predicted within ±6%. TIGER should not be used to set JWLs directly, although there is sometimes no choice but to do so.

Specifically, BKWR produces its detonation energies only by a 10% correction that involves PETN. Its C-J temperatures are also 1000 K too low, but it predicts the C-J pressures closely. BKWS fixes both problems by resetting the constant temperature, Q, but the spread of detonation energies is broader. JCZ3 delivers better energy values, but the v = 2 values are consistently too high and thus the v = 4 and v = 7 results are usually used for comparison. CHEQ's energy values are no better, and the program takes too much time for production calculations. Both JCZ3 and CHEQ calculate temperatures correctly but are 5 to 10% low in C-J pressure and have no library for aluminum and other metals. All versions of TIGER are strongly library-dependent, and the code is not robust.

10. CHEQ postulates adiabat shapes, albeit assuming perfect equilibrium. A study of TATB suggests that the diamond-graphite transition will change the detonation energy enough for experimental verification but that the N_2-H_2O phase transition will not. CHEQ has done its job of introducing new ideas. Modeling of nonequilibrium behavior may be the next step.

11.The Ignition & Growth model is the only theory model that incorporates kinetics. Because of inadequate documentation and lack of upgrades to the programming, it has not received the appreciation and attention it deserves. LX-17 could be converted into a standard explosive for this model.

12. Few cylinder runs on composite explosives produce infinite diameter results that can be compared with those of TIGER. Possible standards include HMX with 10% or less fine aluminum powder and 65% HMX/30% potassium perchlorate. Four very large ANFO shots provide infinite diameter data, but the distance to steady state is about a meter. More work is needed to find composite standards.

13. The less than 1% explosive-accuracy touted by code-runners is really precision. Absolute knowledge of the adiabat is about 3 to 5% at high pressures

and 30% or less at low pressures with the adiabat starting point unknown by 2 to 3 GPa.

14. The lack of predictive capability in composite explosives is extensive. Only two composites might serve as standards in a 100-mm cylinder test. Four types of ANFO are described for which the infinite-diameter detonation velocity has been obtained. It is not possible to unravel size effects from the inherent inability to burn.

2. Suggestions for Experiment

Experimental explosives work should benefit from some of these findings.

1. Fabry-Perot interferometry should be used on all cylinder shots and run out to long times. Work-to-date suggests that 40-μs fabry times will provide sufficient light and allow considerable time slippage for starting the film. The streak camera should be maintained for total displacement.

2. All cylinder tests with nonideal explosives should include the end-on measurement of detonation front curvature as standard. This inexpensive method would have provided vast data on nonideality had it been rigorously applied. It appears to work even with gels possessing surfaces difficult to make flat.

3. A flat-plate "test" should be formalized and run as a fast and inexpensive way of getting JWLs at a fraction of the cost of a cylinder test. A good combination with a 25-mm diameter is 10-mm thickness of explosive and 10 mil (250 nm) of either copper or tantalum run out to 1.5 μs or more. A 20-mm/20-mil combination run to 3 μs would produce similar results, but a 50-mm diameter would be needed.

4. The lack of reproducibility in many plate and cylinder shots that are supposedly the same means that an important level of detail is unknown to us. Improved quality control is needed.

Experiments that would provide needed information are described.

1. The classic test for the spike and adiabat pressure is to measure and analyze the jump-off velocities as a function of plate thickness for thicknesses less than and exceeding the reaction zone. A limited amount of data was assembled for LX-17 in this work, and more is needed.

2. The available lithium fluoride data were not analyzed for this work. The use of a crystal "plate" impedance matched to the explosive offers the possibility of direct read-out of the adiabat pressure. This work needs to be developed.

3. Direct measurement of pressure and volume would supplant the relative derivation of EOSs by cross comparison of code results and "standards"—this appears never to have been done. Present gauges are said to be accurate to ±1.5%. Unfortunately, this is probably not good enough to distinguish between CHEQ and cylinder JWL results between the adiabat point and $v \sim 1.2$. From $v = 1.5$ on, direct measurement might now work. The task of relating constant-pressure gas-gun or diamond-anvil work to an adiabat remains to be done.

4. The detonation point is poorly known, only to ±3 GPa in most cases. Supracompression experiments offer the best means of finding this point. Future experiments should include pressure-gauge measurements and detailed work near the adiabat point and below, where nonequilibrium effects may be seen.

5. Direct temperature and chemical species measurement are needed. Ignition & Growth people expected this work to be completed long ago, but it has not happened. There is a limit to what can be surmised by pushing metal. Eventually, the true innards of detonation must be studied.

3. Suggestions for Code Work

1. At the very least, TIGER needs to be reworked. It needs a more robust solver and C-J point seeker. More work needs to be done on renormalization, including detonation energy as an input along with detonation velocity and assumed C-J pressure and temperature.

2. If we must use the old TIGER code, a complete parameter study and renormalization is needed. The reset would be to C-J pressure, detonation velocity, and detonation energy for several often-used explosives, both ideal and nonideal. At this time, either BKW or JCZ3 appears to be a possible choice for this refit. Should JCZ3 be chosen, it needs to be extended to aluminum and other metals.

3. A production model containing Ignition & Growth–type kinetics is needed. M. Murphy has suggested the use of a faster, two-term model for detonation and a U_s-u_p unreacted Hugoniot. The model could be further simplified by changing the temperature-dependent, reacted JWL to a regular

JWL. A programmed burn with changing detonation vs distance would be useful for initiation.

4. It is time to create a new thermochemical model based on chemical kinetics of the product gases. This will force the consideration of real reactions and processes and start the search for their rates. Such a model would add the missing ingredient of nonequilibrium effects. It is especially needed for composite explosives, where size effects and run-to-detonation cannot be guessed.

Chapter 1. Introduction

1. The Problem of Equation of State

The science of explosives often appears to be merely a collection of opinions. Experiments are difficult and expensive, and there is little university research in this area. Also, the motion of a piece of metal, which is the primary source of data, can be described by different paths in phase space, and thus, rival models compete for validity. Finally, the totally programmatic orientation of the field has led to poor documentation and a virtual absence of critical review.

The purpose of this report is to draw together recent LLNL data on detonation equations of state (EOS), to summarize our current understanding of the field, and to suggest new and predictive avenues of work.

A detonation EOS describes the pressure, P, of an explosion as a function of volume, v, energy, E, and perhaps, temperature. Also present may be a set of rate equations that link one EOS to another. These rates, while not strictly part of the EOS, are so entwined with it that the sum of the pressure/volume information and the rates form a *de facto* EOS. The resulting combination is entered in a hydrodynamics code (hydrocode) to calculate the motion of something as a function of time. Generally, EOSs have been cobbled together for whatever calculation currently suits programmatic needs, with the justification that the dearth of fundamental knowledge makes ad hoc modeling the only practical approach. Ultimately, an EOS should have scientific underpinning and fit a wide and well-understood selection of cases. Unfortunately, this has too often been neglected.

The process by which an EOS is obtained is as important as the result itself. An EOS is easier to accept if the following conditions are met:

1. Measured data are included in the EOS before the hydrocode run. This is important because a variety of data tests an EOS more stringently than does a single experiment. New EOSs are rarely checked against old data and can, in fact, be used to correct errors that occur elsewhere in the calculation and are not associated with the explosive.

2. The EOS is as complex as the quality and quantity of the measured data that support it—which is why the humble JWL is so popular.

3. The EOS is created by a numerical procedure rather than by the operator. This approach removes much of the opinion input and forces a reproducible process.

4. A standard is used. A standard is a special explosive with properties better understood than most. The standard provides the scientist with a comparison on which a large amount of work has been done.

5. Adequate documentation and ease of operation. The more complicated the EOS becomes, the more important is this requirement. Given that documentation is generally poor in the explosives' field, the JWL again wins in this category.

The ideal EOS might be obtained from a CHEQ-like program and include reaction kinetics, which independently have been fit to a large collection of Hugoniots, all of which have been documented. The program would generate all points in the two-dimensional (2-D) pressure-volume (P-v) space. It could then be simplified into a 2-D table input or more likely, into a one-dimensional (1-D) (with only the Principle Adiabat) input for the hydrocode. This example shows that we often erroneously consider the final input to the hydrocode to be the EOS, apart from the database that generated it.

Three examples will be considered; all are main topics of this report. The first is the LLNL Cylinder JWL, placed in its present form by John Kury. The JWL is a simple P, v, E equation for the Principal Adiabat. The approach uses a 1.763-g/cc PETN standard for which the JWL is believed, although the pedigree could be upgraded. The cylinder wall velocities of other explosives are converted into detonation energies by velocity-squared comparisons with PETN. The results are JWLs, which are used and supported in all codes because of their simplicity. The EOS for a new explosive is the process of obtaining the final JWL from cylinder data before the hydrocode is run. Although the description sounds simple, it actually took two decades for this EOS to be derived, and it has not been compactly described until this report. The simplicity of the JWL explains its longevity.

The second example is the Look-Up Table described below. This is the Principal Adiabat in P, v, E form but arranged in a table with interpolation between points. Its advantage is that it gives a Principal Adiabat unconstrained by an analytic form (e.g., a JWL) that does not conform to physical reality. The thermochemical code CHEQ supplies the input. The major weakness is that the CHEQ output is not, for several reasons, necessarily accurate. Thus, operator intervention is necessary to correct the table, and the validity of the table is again dependent on operator judgement and the quality of the database. Considerable work needs to be done to validate the tables.

The third example is Ignition & Growth (I&G or Reactive Flow). Usually, two temperature-dependent JWLs are used, one for the unreacted explosive and one for the reaction products. Sometimes, a third JWL is added

to represent reaction products further along in time. A set of time-dependent rate equations link the EOSs. For nonideal explosives, kinetics must be accounted for if detonation is to be accurate. For initiation, the time dependence cannot be ignored. At present, I&G is the only model with these features.

I&G has not fared well in production at LX-17–oriented LLNL. It is a complicated EOS, used generally by experts, and it is not well-supported in the codes. It runs up to ten times slower in a hydrocode than does the JWL version. Its input contains no experimental data, and the constants are generated by the operator as he/she runs successive hydrocodes. The output does not implicitly show detonation velocity. Despite the enormous output on LX-17, this explosive has never been converted into a standard. No review articles describe I&G, and no user-friendly computer features have been invented. Finally, LX-17 is only slightly nonideal, and the JWL or the table can be adjusted to make up the difference. A explosive like ANFO is so highly nonideal that I&G is absolutely necessary.

Significant practical problems are associated with I&G. Because I&G attempts to explicitly describe the detonation front, the zoning for a problem must reflect this. Thus, the running time for a problem is prohibitive for anything but the simplest problems. Also, the large number of empirically derived constants does not inspire confidence in the fundamental validity of the model. For these reasons, I&G has been confined to a small set of special case problems and has not been tested in larger and more complex configurations.

2. Notes Regarding This Work

A. Detonation Points. In writing this report, we found the term "C-J point" to be used indiscriminately. Al Nichols argues that the C-J point is the true thermodynamic equibrium point at which temperature becomes defined in the reaction products behind the shock wave. It holds for an explosive of infinite diameter and at steady state. In this light, a C-J point is probably obtained only in a thermochemical code. All other points are different and must be defined. Here, a list of various detonation points are defined in terms of their pressures.

P_k. This is the first, high-pike pressure seen in the thin-plate test or used in the I&G code. It results from the initial compression of the unburned or partly burned explosive. As the reaction continues, this pressure drops down the Rayleigh Line toward a detonation point where it diverges onto the Principal Adiabat.

P_a. The adiabat pressure is the point at which a steady-state, large-size explosive leaves the Rayleigh Line and commences its journey down the Principal Adiabat. True thermodynamic equilibrium has not been proved, but no obvious size effect is known. This point is a practical but special characteristic of a bulk explosive and is what many people call the "C-J" point. This is also the point at which the burn fraction equals 1 in the I&G code. Because this is a special point, special efforts must be made with any experiment to show that the data describe an adiabat point and not just a detonation point containing other effects.

P_p. The plate pressure is obtained from plate experiments using the algebraic impedance-match equation as defined in Chapter 5. Jump-off velocity (for a plate or cylinder) or supracompression with a plate may be used. When the plate is thin, the pressure seen is P_k for a near-ideal explosive. When the thickness of the plate is equal to the reaction zone, the pressure is thought to be P_a for a near-ideal explosive. The latter may become the initial pressure in a plate-derived JWL.

P_j. The Cylinder Test JWL pressure is obtained using a three-point fit to the wall velocity data. It is not considered to be a true C-J point.

P_{cj}. In C-J theory, the C-J pressure is the equilibrium pressure at the rear of the reaction zone. It is the initial pressure obtained in a thermochemical code, perhaps the only place that true equilibrium exists. It is likely about 2 GPa below the adiabat pressure, where nonequilibrium effects occur.

P_n. The sonic pressure is the point at which the products move onto the Principal Adiabat for an explosive known not to be in thermodynamic equilibrium because (1) the explosive is at steady state but not at large-diameter or (2) the detonation has not reached steady state. Virtually all composites fall into this group.

B. Rankine-Hugoniot Equations. These equations for the conservation of mass, momentum, and energy assume a piston-driven shock wave, a situation only found explicity for an ideal explosive in a gas-gun experiment with a heavy sabot. The equations nevertheless are used everywhere. They are:

$$\text{Mass: } \rho_o D = \rho_p (D - u_p) \qquad (1)$$

$$\text{Momentum: } P_p - P_o = -D\,dm/dt + dm/dt(D - u_p), \qquad (2)$$

where ρ_0 and ρ_p are the densities of the initial unburned explosive and the burned products, P_p is the detonation pressure, P_0 is the initial pressure (essentially zero), D is the detonation velocity, u_p is the explosive particle velocity, m is mass, and t is time. The two equations may be combined to form the shock impedance relation

$$P_p = \rho_0 D u_p. \tag{3}$$

Energy conservation leads to the Hugoniot equation:

$$\text{Energy: } E_2 - E_1 = (P_2 + P_1)(v_1 - v_2) / 2, \tag{4}$$

where E is energy, v is relative volume, and the subscripts refer to any two points on the curve. Unlike Eqs. (1) and (3), Eq. (4) is too general to be used by itself. In thermochemical codes, the energy of detonation is dumped into the product gases at 1 atm. Then, the Hugoniot is traced out, using Eq. (4) and various thermodynamic descriptions of the products.

C. Units. Mbar units and certain other units are found thoughout this report. Conversions may be made as follows:

Pressure:	Mba —> GPa	multiply by 100	
Energy:	Mbar·cc/cc —> kJ/cc	multiply by 100.	(5)

A calorie becomes a joule when it is multiplied by 4.184. TIGER gives atmospheres for pressure. A mega-atmosphere (Matm) becomes a GPa when it is multiplied by 101.325.

Pressure in the Rankine-Hugoniot momentum relation is maintained, luckily, with the following "mongrel" equality:

$$\text{GPa} = (\text{g/cc})\,(\text{mm}/\mu\text{s})^2. \tag{6}$$

Pressure and energy may be compared using

$$\text{GPa} = \text{kJ/cc}. \tag{7}$$

D. Detonation energy is presented as a positive number in this text. It is usually negative in chemical thermodynamic literature because the reaction is exothermic.

E. The data listed in this report come from a mixture of internal sources, including detailed files from the Cray, the Cylinder Handbook, and loose pages in the shot folders. The resources were not available to process the data in a systematic, statistical way. It may be possible to obtain more detail by mining the old data with more care. Many explosives are referred to many times in Chapters 2 to 8. See the Appendix for compositions and details of these explosives. Finally, all persons mentioned here without a footnote are LLNL employees.

Chapter 2. EOS Description

1. Definition of the JWL

The (standard) JWL (for Jones, Wilkins, and E. L. Lee) is the most used EOS at LLNL. The JWL is a coupled set of equations. From the initial v = 1 condition, the detonation compresses the explosive to the detonation volume, v_j. The straight line that connects these two points in P-v space is called the Rayleigh line. It is given by

$$P = \rho_o D^2 (1 - v), \tag{1}$$

where P is pressure, D is the detonation velocity, and v is the relative volume. At the detonation point, we have

$$v_j = 1 - P_j/\rho_o D^2. \tag{2}$$

The detonation velocity, D, is measured, and the detonation pressure, P_j, is estimated. From this, v_j is determined. At the detonation point, the slope of the pressure is

$$dP_j/dv_j = -\rho_o D^2. \tag{3}$$

This may be recast into the variable γ_j given by

$$\gamma_j = -d\ln P_j / d\ln v_j = \rho_o D^2 v_j / P_j, \tag{4}$$

which is generally expected to lie between 2.6 and 3.0. Also,

$$v_j = \gamma_j / (\gamma_j + 1), \tag{5}$$

$$\gamma_j = v_j / (1 - v_j), \tag{6}$$

and

$$P_j = \rho_o D^2 / (\gamma_j + 1). \tag{7}$$

For one initial cubic centimeter of explosive, the total energy of compression to the detonation point , E_c, is

$$E_c = \rho_o D^2 (1 - v_j)^2 / 2 = P_j^2 / 2\rho_o D^2. \quad (8)$$

At the detonation point, the compressed explosive suddenly transforms into hot gaseous reaction products, which then expand along the adiabat with a pressure, P_s, such that

$$P_s(v) = A\exp(-R_1 v) + B\exp(-R_2 v) + Cv^{-(1+\omega)}. \quad (9)$$

This equation may be integrated, assuming constant entropy, by $-P_s dV$ to obtain

$$E_s(v) = (A/R_1)\exp(-R_1 v) + (B/R_2)\exp(-R_2 v) + C/\omega v^{\omega} \quad (10)$$

E_s is a positive number, which decreases from the detonation point, $E_s(v_j)$, to zero for infinite volume of the detonation products. Note that E_s is a total energy and is different from the thermal energy found elsewhere in the temperature-dependent JWL. In order to obtain the energy of detonation at volume v, $E_d(v)$, we need to subtract the energy of compression from the energy of the adiabatic expansion:

$$E_d(v) = [E_s(v_j) - E_s(v)] - E_c. \quad (11)$$

If all energies on the right side of the equation are positive, E_d will be negative at small volumes and positive for larger volumes of practical significance. (We have noted that this physics convention is opposite from the chemical convention, which sets exothermic reactions as negative.) E_d is zero at the point where the adiabat energy output equals the energy put in by compression. This usually occurs not at v = 1, but at about v = 0.92. The energy of detonation at infinite volume is a positive number, E_o:

$$E_o = E_s(v_j) - E_c, \quad (12)$$

so that

$$E_d(v) = E_o - E_s(v). \quad (13)$$

For $v \longrightarrow \infty$, $E_s(v) \longrightarrow 0$, and $E_d(\infty) \longrightarrow E_o$, the infinite volume energy of detonation.

The derivative is

$$dP_s / dv = -\rho_o D^2 = -R_1 A \exp(-R_1 v) - R_2 B \exp(-R_2 v) - (\omega + 1) C v^{-(\omega + 2)}, \quad (14)$$

which may be converted to γ by multiplying it by $-(v/P_s)$.

One can eliminate C between Eqs. (9) and (10) to obtain this form of the pressure adiabat, which is identical to Eq. (9):

$$P_S = A(1 - \omega/R_1 v)\exp(-R_1 v) + B(1 - \omega/R_2 v)\exp(-R_2 v) + \omega E_S/v \quad (15)$$

Eq. (15) is the form of the JWL used in codes. At the detonation point, P_s, E_s, and v are all known. One then slightly increases the volume by Δv. By using Eq. (15) with the new v and the old E_s, P_s can be calculated. Then, E_s is adjusted by

$$E_s(\text{new}) \sim E_s - P_s \Delta v. \quad (16)$$

By moving in steps of $\Delta v = 0.001$ or less, the form of the analytical equation Eq. (15) is reproduced. A code then inputs A, B, R_1, R_2, ω, D, and E_0. The detonation point value of E_s is calculated from E_0 so that C is not needed.

The JWL is popular because it can be integrated easily and the integral converges even to $v \longrightarrow \infty$, which removes the need of selecting a real endpoint for the expansion process. However, a cutoff at 1 atmosphere is actually the physical endpoint.

2. Look-Up Tables

Certain features of the JWL may be questioned. First, it seems reasonable that $\gamma = -\partial \ln P / \partial \ln v$ should be constant or decreasing at the detonation point. Instead, it rises in the JWL from the detonation point to a maximum at about v = 1. The rising γ is caused by the "A" term of the JWL , which dominates near the detonation point. An exponential divided by its derivative is a constant, so the volume term in γ dominates. A second JWL problem is the double peak in γ caused by the presence of the two exponentials. The presence of phase transitions between graphite/diamond and nitrogen/water may further complicate the adiabat.

An alternative to the JWL is the Look-Up Table, where γ may be designed to suit. Such a table could list P_s and v point by point, but the table is built instead on the function f(v) and the adiabat energy in the form

$$P_s(v) = f(v)\, E_s(v) / v. \quad (17)$$

This equation has been placed in both 1-D and 2-D codes. In these codes, P_s, E_s, f, and v are all known at the detonation point. Then, v is increased by Δv and a new f is calculated using either a function or the Look-Up Table. Using the new v and f and the old E_s, a new P_s is calculated using Eq. (17). E_s is then adjusted downward by

$$E_s(\text{new}) \sim E_s - P_s \Delta v. \tag{18}$$

With small volume increments of 0.001 or less, the adiabat is reproduced.

We consider some of the properties of the function f. The derivative of Eq. (17) is

$$\frac{\partial P_s}{\partial v} = \frac{E_s}{v}\frac{\partial f}{\partial v} + \frac{f}{v}\frac{\partial E_s}{\partial v} - \frac{fE_s}{v^2}. \tag{19}$$

We multiply both sides by $-v/P_s$ and substitute $\partial E_s/\partial v = -P_s$ in Eq. (17) to obtain

$$\gamma = -\partial \ln P_s/\partial \ln v = f + 1 - \partial \ln f / \partial \ln v. \tag{20}$$

One may use the definition of γ and its integral to obtain pressure by integration with

$$\ln P_s = \int \frac{\gamma dv}{v}. \tag{21}$$

The integration will be numerical with

$$\Delta \ln P_s = (\gamma/v)\Delta v + \text{sum of previous terms}, \tag{22}$$

where we start at the detonation point—where P_s and E_s can be set. We then integrate both to lower and higher volumes. Finally, we use Eq. (17) to obtain E_s. An advantage is that γ changes slowly with v so that we can use a large volume differential (0.001 to 0.01, depending on v), and we will still get a good answer. Hence, the integration may even be done on a large spreadsheet.

The meaning of f may be further explored. At large volumes, the JWL pressure is

$$P_s = C / v^{1+\omega}, \tag{23}$$

and the adiabat energy is

$$E_s = C / \omega v^{\omega}. \quad (24)$$

Then, by Eq. (17),

$$f = \omega \quad (25)$$

at large volumes.

The function f can be put into an analytical format as well. PETN of 1.763 g/cc can be described from its JWL using

$$f \sim 10\exp(-2.5v^{0.25}) + 0.57. \quad (26)$$

From CHEQ, the fit is

$$f \sim 11\exp(-2.45v^{0.50}) + 0.285. \quad (27)$$

A similar EOS has been recently put forth by W. C. Davis.[1] His equation is

$$P_s = (E_s / v)\{g - 1 + F(v)\}. \quad (28)$$

The same ratio of P_s/E_s appears, with F(v) used to make the function change as it should. He also has extended his function of the off-adiabat case. Here, and above, the intent is to use the ratio P_s/E_s and create a slowly changing function over the many decades of pressure and energy.

3. References

1. W. C. Davis, "Equation of State for Detonation Products," presented at the Tenth International Detonation Symposium, Boston, MA, July 12–16, 1993.

Chapter 3. Deriving Cylinder JWLs

1. Description of the Cylinder Test

The Livermore Cylinder Test has long been the means of obtaining the JWL.[1–5] The precisely machined cylinder is made of OHFC copper. Two wall thicknesses are used: one is 1/20th the inner diameter (half-wall) and the other is 1/10th the inner diameter (full-wall). The full wall, which is easier to machine, came first. The explosive inside is initiated at the bottom and detonates upward, blowing out the copper walls into an inverted funnel. The elastic/plastic properties of the copper allow the wall to deform elastically up to nearly three times the original diameter. A horizontal slit is focused at a given point on the cylinder to measure the wall motion perpendicular to the cylinder axis with a streak camera. The cylinder wall displacement is measured as a function of time, with two cameras taking pictures of both sides for a total of four records. The wall velocity is then calculated at three standard distances of 6, 12.5, and 19 mm of cylinder wall displacement for a 12.7-mm inner radius. In addition to the streak cameras, two Fabry-Perot interferometers, set 180° apart, measure opposite-wall velocities directly at an angle, Θ_p, of $7° \pm 0.2°$ to the cylinder axis, and also at the height of the observation slit. The Fabry beam does not hit the point seen by the streak camera, but is rotated around the cylinder at the same height (about 3–5 mm).

Most cylinders used in this report are 1 or 2 in. in diameter. They are 300 mm long with inner radii of 12.7 and 25.4 mm. The 1-in. cylinder is a standard in that all data are scaled to this size. For a 12.7-mm radius, a half-wall thickness is 1.27 mm, so the outer radius is 13.97 mm. The full-wall thickness is 2.54 mm, so the outer radius is 15.24 mm. The observation slit for the streak camera or Fabry is 210 mm from the base of the cylinder. The pins to measure detonation velocity are set 90 and 290 mm from the base. It is assumed that the detonation velocity has reached steady state by 90 mm and that the detonation front is steady at 210 mm.

A 4-in. cylinder is sometimes used for nonideal explosives. This cylinder has an inner diameter of 50.8 mm and can be half- or full-wall. The cylinder is 1000 mm long with the observation slit at 710 mm. The detonation velocity pins are set 380 and 990 mm from the bottom of the cylinder. The largest , the 8-in. cylinder, has an inner diameter of 203 mm and a length of 1220 mm.

The initiation train at the bottom of a 25-mm cylinder starts with an SE-1 (PETN) detonator with a bridge wire. This ignites a 12.7- × 12.7-mm tetryl cylindrical pellet and drives a plane-wave lens of PBX9501/TNT that enters a 12-mm-thick booster pad of Comp B (detonation pressure 29 GPa) or Detasheet (18–20 GPa). Comp B is 63 wt% RDX, 36% TNT, and 1% wax. Detasheet

EL-506C is 63 wt% PETN, 8% nitrocellulose, and the plasticizer 29% ATBC (acetyl-tributyl citrate).

A thin, 0.25-mm stainless steel sheet is the final barrier to the bottom of the cylinder. The lens, booster pad, and steel sheet overlap the outer edge of the cylinder for all sizes except the largest. The lenses in use are the P-16 (40.6-mm or 1.6-in. diameter), the P-22 (560-mm or 2.2-in. diameter), the P-40 (102-mm or 4.0-in. diameter), and the P-78 (198-mm or 7.8-in. diameter). The current PBX9501/TNT lenses are from Los Alamos National Laboratory (LANL) and replace an older Comp B/Baratol version used until about 1992. The variation in flatness is thought by L. Shaw to be about ±30 ns for a 1-in.-diameter lens. F. Helm believes the variation to be about ±60 ns for a 4-in. lens.

The data are always listed as scaled to a 25-mm- (1-in.-) diameter cylinder. To scale down from a 51-mm- (2-in.-) diameter cylinder, time and the increase in radius, $R - R_0$, are divided by 2. To scale from 102-mm (4-in.) cylinder, time and distance are divided by 4. Velocities are never divided. However, it is easy to combine a correct velocity with the wrong scaled time or distance.

Certain times must be considered in the Cylinder Test. In the smaller cylinders, the detonation wave that we measured at 210 mm will blow out the top of the cylinder 90 mm above. For 1.763 g/cc PETN, the detonation velocity is 8.274 mm/μs. We take the shock wave speed in copper as about 4.5 mm/μs. The rarefaction wave from the top of the cylinder will move back down the 90 mm to the slit position. The time we have for measurement is 31 μs, a long time for a 25-mm-diameter cylinder, but only 15.5 μs for a scaled-down, 51-mm cylinder.

Also, the detonator on the bottom is larger than the base of the cylinder; thus it drives the copper upward and also ignites the explosive. The detonation wave passes the slit 25.4 μs after detonation at the bottom. The shock wave coming up the copper starts at 4.5 mm/μs but degrades to the sound speed of 3.94 mm/μs with the wave spreading out spatially. For the 25-mm cylinder, the crest of the wave passes the slit at about 52 or 27 μs after the detonation wave. The crest of the wave passes the slit at only 13.5 μs for a 51-mm cylinder.

Suppose we had a weak explosive with a detonation velocity of only 5.5 mm/μs. The difference between the explosive and the copper is only about 1.5 mm/μs. In a 25-mm cylinder, the time for the top reflection to return to the slit is about 37 μs, but the bottom shock wave in the wall reaches the slit only 14 μs later. The effect of the rising wave in the copper wall does not appear to have been much considered.

The cylinder is an EOS "test" because it possesses a geometry that allows the approximate calculation of the relative volume of the gaseous detonation products, v. If we calculate a geometric volume, v_g, from the expansion of the cylinder, and if

$$v \sim v_g, \tag{1}$$

then we can use this volume in the JWL EOS.

What is measured is the outer radius, R, although we usually think of the explosive inside with an inner radius, S. Possible confusion of the two must always be kept in mind. The cylinder data have generally been measured at radial displacements, $R–R_0$, of 6, 12.5, and 19 mm, where R is the outer radius at time t and R_0 is the initial outer radius, taken as scaled to an initial inner radius of 12.7 mm. The radial displacements above have traditionally been associated with the rough relative volume values of 2, 4, and 7. From a geometric view of the cylinder, we might expect, if the gas pressure is all outward, that

$$v \sim (R / R_0)^2, \tag{2}$$

which produces values of 2.17, 3.94, and 6.23, respectively, for the radial displacements listed above. The use of Eq. (2) assumes that the wall thickness is constant with relative volume. We then examined our hydrocode output to correct for the expansion of the cylinder and the decrease in gas pressure as gas moves backward in the cylinder.[6] This adjusts the volumes to 2.2, 4.1, and 6.5 at 6, 12.5, and 19 mm, respectively.

2. How the LLNL Cylinder JWL Is Obtained

It would be possible to run hydrocodes for every cylinder ever fired and match the JWLs with the measured velocities. This would be extremely expensive, however, and it was long ago abandoned for the standard explosive. The standard used to be PBX-9404 but is now PETN at 1.763 g/cc. The JWL, listed in the next section, for PETN is taken as delivering believable energies. We list three special PETN points:

	Rel.	Velocity (mm/μs)		E_d
$R - R_0$ (mm)	Vol. v	PETN half-wall	PETN full-wall	PETN (kJ/cc)
6	2.2	2.09	1.58	6.51
12.5	4.1	2.28	1.72	7.87
19	6.5	2.38	1.78	8.55

(3)

One next obtains the measured outer wall velocities of a new explosive at the same values of $R - R_0$. At each volume, v, the expected energy of detonation of the new explosive, E_d, will be

$$E_d = \left(\frac{u}{u\,(PETN)}\right)^2 E_d\,(PETN). \tag{4}$$

where u is the cylinder wall velocity. Eq. (4) equates the square of the velocity, by way of kinetic energy, to the detonation velocity. This allows us to calculate three detonation energies at volumes of 2.2, 4.1, and 6.5 for explosive x.

The "three-point" method for obtaining a JWL uses the points at v = 2.2, 4.1, and 6.5. One sets up a small program that first calculates the detonation volume, v_j, from the Rayleigh Line, as described in Chapter 2. Then, the following three JWL equations are solved at the detonation point. $E_s(j)$ is the adiabat energy at the detonation point.

$$dP_j / dv_j = -\rho_o D^2 = -R_1 A\exp(-R_1 v_j) - R_2 B\exp(-R_2 v_j) - (\omega + 1)Cv_j^{-(\omega + 2)} \tag{5}$$

$$P_j = A\exp(-R_1 v_j) + B\exp(-R_2 v_j) + Cv_j^{-(1 + \omega)} \tag{6}$$

$$E_s(j) = (A/R_1)\exp(-R_1 v_j) + (B/R_2)\exp(-R_2 v_j) + C / \omega v_j^{\omega} \tag{7}$$

where

$$E_s(j) = P_j^2 / 2\rho_o D^2 - E_o. \tag{8}$$

If one estimates E_o, Pj, R_1, R_2, and ω, then Eqs. (5), (6), and (7) may be solved as a set of linear simultaneous equations using the method of determinants. One then adjusts the constants until the closest fit, usually 0.5 to 1%, is obtained with the PETN-modified energies. The operator has a major role in this process. From the value of D, the operator estimates P_j and E_o, so they start fairly close. The percent spread in the three measured points is observed. Then, minor changes are made until this spread is a minimum. Operator inertia keeps this from expanding to a larger parameter space. The resulting minimum may be a local one and a fitting routine may go far off-course to find a better answer, but the three-point process works very well in finding answers that appear right.

There are two major assumptions to the LLNL Cylinder EOS: (1) the uncertainties in the fixing of the JWL parameters do not greatly affect the energy of detonation and (2) the ratio of the energy of detonation/ velocity-squared is the same for all explosives. The first is considered below, and the second in Chapter 5.

3. Choosing the PETN Standard

PETN of density 1.760 to 1.765 g/cc is considered a suitable standard explosive because it has a very short reaction zone, does not form solid carbon,[7] and has nearly constant products in various conditions of confinement as found by calorimetry.[8] It is oxygen-rich and close to being an ideal explosive. The reaction zone has been estimated by L. Green to be less than 0.07 mm. The absence of carbon was surmised by B. Hayes from the low 100 mhos/m conductivity found at 400 to 2000 MHz in runs of up to 20 ns.[7] In contrast, the conductivity of liquid TNT rose to 10,000 mhos/m at 20 ns. Hayes estimated the carbon content in PETN to be only about 0.1 g/cc. The absence of solid carbon allows the PETN detonation energy to be measured with great accuracy. Ornellas' measured heat of detonation for confined 1.735 g/cc PETN was only 1.1% below that calculated from the products.[8] Unlike many explosives, this energy is the same with various wall materials and even for the unconfined detonation.

The JWL for PETN has received considerable attention. It was studied by Hornig et al. from the shocks sent into Plexiglas.[9] The standard JWL was generated using the 1-D hydrocode KOVEC from this work. Detonation pressures from 31.5 to 32.5 GPa were run, and it is impossible to make a final determination between them. Next, the Fabry data from PETN cylinder no. 511 were modeled in HEMP by J. Walton. The Fabry data were taken only for 6 μs, corresponding to a final $R - R_0$ of 11.5, and as discussed further in Chapter 5, it did not bear the correct ratio to the streak data. Two HEMP runs were plotted: the 31.5 GPa, $E_0 = -10.8$ kJ/cc standard and a 32.0 GPa, −10.1 kJ/cc model. The standard JWL appeared to fit the data, whereas the 32 GPa curve lay a few percent too high. Thus, the 31.5-GPa standard JWL was born. Supracompressed studies on PETN were added by Green, Holmes, and Kury, and the Hugoniot data fit the JWL of the adiabat by 6% at 80 GPa, 2.4% at 63 GPa, and 1.3% or less below 40 GPa.[10]

J. Kury and L. Green, who worked on the PETN standard, felt that its properties were known with considerable accuracy. They estimated the detonation pressure to be known to 2%, i.e., 31.5 ± 0.6 GPa, with ± 1.0 GPa at the 95% confidence level. They gave the detonation velocity for PETN at 1.763 g/cc as 8.274 ± 0.01 mm/μs. Thus, the cylinder-standard PETN constants were set to be[10]

A	1032.158 GPa
B	90.57014 GPa
C	3.72735 GPa
R_1	6.00
R_2	2.60

ω	0.57
P_j	31.5 GPa
D	8.274 mm/μs

(9)

Also, $v_j = 0.739008$, $\gamma_j = 2.83153$, and $E_o = 10.80$ kJ/cc. The large number of digits does not mean that they are significant; they are needed, however, to make the coupled equations come out right, regardless of whether C or E_o is used as a constant for calculation. Even a small round-off in a JWL constant can produce a large change in the calculated detonation energy.

Not all PETN sample densities are exactly 1.763 g/cc. On the basis of three densities from 1.26 to 1.76 g/cc, we find

$$D \sim \rho_o, \tag{10}$$

and for two densities at 1.5 and 1.76 g/cc

$$E_o \sim \rho_o. \tag{11}$$

It appears that the purity of old PETN may not have been as good as originally believed. A recent analysis has shown the presence of 3.8 wt% petrin, an analog in which one nitro group is replaced by a hydrogen, thereby creating a hydroxyl group.[11] This would be a less energetic molecule.

4. Accuracy of the JWL Energy of Detonation

Table 3-1 lists several JWLs for LX-14 and LX-17. The first two are from cylinders; the last are from other, high-compression experiments. The two cylinder JWLs are separated by at least a decade and have not been derived from the same wall and detonation velocity data. The detonation energies as calculated at v = 2.2, 4.1, and 6.5 are listed. The 1985, old-handbook cylinder[12] JWL and the No. 381 JWL for LX-14 were considered to be "in agreement" because they had the same value near v = 2.

Table 3-1 also shows that the LX-17 1985, old-handbook cylinder JWL[12] and the No. LH JWL are 2 to 3% low at all volumes. At the time, the difference was thought to be about 4%, and the cylinder was considered to be at fault. In fact, the differences are within the jitter seen with LX-14. If one redoes the cylinder JWL, the differences become worse, reaching –3 to –8%. The reason is that the three-point cylinder process produces a detonation pressure of about 26 to 27 GPa for LX-17, whereas the pressure measured in other experiments is higher.

It is interesting to reconstruct the thinking of the mid1980s when the LX-17 JWLs were constructed.[13] Ed Lee first constructed a cylinder JWL with a 27.5-GPa detonation pressure. This is the original analog of the 26.5 GPa version in Table 3-1. However, L. Haselman determined a value of 30 GPa based on experiments with compression to small volumes. Others, using the Sack EOS, came up with 33 to 34 GPa. Electric-gun plate shots were just starting in the High Explosives Applications Facility (HEAF) and were producing 32-GPa values. E. Lee took the 30 GPa Haselman value and modeled the early-time cylinder behavior, as shown in Fig. 3-1, with DYNA2D. A 30-GPa detonation pressure obviously fits the jump-off better than 26 GPa, but the 26-GPa JWL fits better at 4 μs. This behavior is caused by the nonideality of LX-17.

5. Uniqueness of the JWL Parameters for PETN

The well-known JWLs have been run over time and over various experiments. The code-runner remembers the results and adjusts the coefficients until the result is fairly accurate. Unfortunately, this process cannot be demonstrated later on nor can it be easily reproduced. The result is a lack of documented pedigree for the JWLs.

We may next ask how sensitive the JWL parameters are to a Cylinder Test. It is not easy to run large sets of hydrocodes because of the time requirement. An easier way is to use Ernie Baker's analytical cylinder code model.[14,15] This model, which runs instantly on a PC, is a set of mass-momentum-energy algorithms that approximate the physics. In Chapter 4, we derive the cylinder angles, where Θ_s is the angle of the fanning out of the wall. The radial velocity is $u_s = D\tan\Theta_s$, where D is the detonation velocity. Baker's model works by letting Θ_s increase, taking the radial velocity with it.

For 1.763 g/cc PETN, we ran various JWLs using Baker's Spherical Products (number 4) cylinder model. One obtains wall velocity as a function of the cylinder's change of radius, $(R/R_0)^2$. Thus, the velocity is zero when $(R/R_0)^2 = 1$. This, and the absence of a jump-off velocity, puts about 3% less energy into the analytical model. The Baker-model JWLs used to fit actual data are boosted by this amount as compared to cylinder JWLs. However, we are interested in the relative difference. We require the model to reproduce the experimental half-wall radial velocities of 2.09 mm/μs at v = 2.2 and 2.38 mm/μs at v = 6.5 within ±0.02 mm/μs. This is the precision of a real experiment, at least when streak cameras are used.

The results for 1.763 g/cc PETN are shown in Table 3-2. We see that the velocities may be accurately represented with detonation pressures that vary by 2.5 GPa (8%) or with total detonation energies, E_0, that vary by 1.2 kJ/cc (11%). In-between combinations of 4% change in P_j with 5% change in E_0 also

work. We see that the v = 2.2 and v = 6.5 detonation energies (proportional to the velocity-squared) cannot be distinguished from one another.

The wide assortment of parameters that fit should not disguise the gentle but real minimum that exists. A carefully done JWL fit finds this minimum fairly well so that the resulting detonation pressures and total energies are, in many cases, close to the measured ones. The energy, E_0, and the detonation velocity are the only accurately known quantities that can be found for a detonation. It is important for the physical reality of the JWL that its E_0 agree with the calorimetric value, even if we must adjust the other parameters somewhat. We see that this is easily achieved.

The Cylinder Test really works in the region $2 < v < 7$ with the detonation point being set by extrapolation, assuming the validity of the JWL function. As we see in Table 3-2, the detonation energies that look so similar at $2 < v < 7$ diverge at v = 1.5. In the past, a study of the cylinder jump-off led to the final adjustment of the JWL, but it can be more easily done now by adding a plate shot, which sees the low volume region. The JWLs of Table 3-2 include results from the LLNL 1-D code for a PETN thickness of 20 mm and a tantalum plate of 20 mils. The calculated velocities at jump-off and at the fifth dip at 1.3 μs are listed. We see that enough variability exists that the plate experiment could easily see the difference.

At this time, we cannot establish a solid pedigree for the PETN standard in terms of cylinder and plate shots. This must await further work in comparing hydrocode output.

6. Total Detonation Energy from the Cylinder and the Calorimeter

In setting the JWL, the total energy of detonation, E_0, is changed as if it were one of the variables. It is important to see how close these values come to experimental values. The measured heats of detonation, H_0(exptl), were taken from Ornellas, as listed in Table 3-3.[8] These values are compared with cylinder shots using almost but not quite the same explosive density. A linear adjustment is made to the heats using the density.

Ornellas' heats also contain the heat of condensation of the water, and we wish to use an energy in which the water is still a gas, even at room temperature. The energy of vaporization is

$$E_{water} = 44.016 \nu_{water} \rho_0 / M, \qquad (13)$$

where the molar energy of vaporization is 44.016 kJ/mole, ν_{water} is the number of mols of water found by Ornellas per mol of explosive, and M is the molecular weight of the explosive. This adjustment is negative and decreases the detonation energy because energy thought to be derived from detonation in the

calorimeter is really derived from water becoming liquid. In the case of dense PETN and HMX, this energy is 0.9 kJ/cc, or a large 8% effect.

Another, smaller adjustment is made for the positive PV energy, which is

$$E_{PV} = RT_o\nu_{total}\rho_o/M, \tag{14}$$

where R is the gas constant (8.3144 J/mol·K), T_o is 298 K, and ν_{total} is the total number of mols of products per mol of explosives as found by Ornellas. The final energy of detonation with water as a liquid is

$$E_o(exptl) = H_o(exptl) - E_{water} + E_{PV}. \tag{15}$$

The comparison of measured cylinder and JWL energies shown in Table 3-3 are quite good, so that E_o in the JWL is close to the actual measured energy. The agreement between calorimetric experiment and JWL cylinder derivation for these homogeneous explosives is

$$\% = 0.7 \pm 3.7\%. \tag{16}$$

It is worth reiterating that, after the detonation velocity, E_o is the most accurate experimental explosive number. Calorimetry remains a basic measurement for explosives.

Also, in Table 3-3, we calculate the total heat of detonation with the gaseous water (energy of detonation plus PV), H_o(exptl, gas). We next calculate this heat from

$$H_o(exptl, gas) = H_f(products, gas) - H_f(reactant). \tag{17}$$

The heat of formation of the explosive (reactant) is listed in the Appendix. The heats of formation for the products are for the gases, including water, and for CO_2, H_2O, HF, CH_4, and NH_3 are 392, 238, 269, 74.9, and 46.0 kJ/mol, respectively. The steps for calculation are (1) react all fluorine to HF, (2) react all oxygen to water, (3) react all carbon with remaining oxygen to CO_2 leaving unreacted carbon as the element, (4) react remaining hydrogen with carbon to methane, and (5) react remaining hydrogen with nitrogen to ammonia. The result for the 16 explosives in Table 3-3 is $12 \pm 13\%$ for the complete burning of carbon. By setting to an 80% burn to CO_2 with 20% CO, we have an agreement of

$$0 \pm 11\% \tag{18}$$

with the measured data. The broad band of uncertainty comes because we cannot guess ahead of time how efficient the burning of the carbon will be. HNS is the least efficient of all; BTF, NM, low density HMX, and TNT are also low. The most efficiency explosives are HNB, RX-23-AA, and high density HMX.

7. Approaching Perfect Gas Behavior

One means of establishing credibility for an EOS is to make it approach perfect gas behavior at large volumes. CHEQ meets this requirement, as can be found by calculating the compressibility, z, using

$$z = PvV_o/nRT, \tag{19}$$

where P in GPa, v is dimensionless, V_o is in cc/mol, n is dimensionless (mols/mol), and R (the Gas Constant) is 8.314×10^{-3} kJ/mol·K.. The parameter n is the number of moles of gas created per mole of explosive. In CHEQ, $z \longrightarrow 1$, as expected.

For adiabatic expansion, the change in entropy is

$$dS = 0 = C_v dT/T + RdV/V, \tag{20}$$

where C_v is the heat capacity at constant volume. If C_v is temperature-independent, then

$$T \sim V^{-R/C_v} \tag{21}$$

so that

$$\omega \sim R / C_v. \tag{22}$$

This is the source of making ω a constant at large volumes. If ω were the same for all explosives, we would fully understand one end of the EOS. The CHEQ code (see Chapter 8), with an adjusted adiabat energy, produces $\omega = 0.28$ for PETN at 1.763 g/cc and $\omega = 0.22$ for HNB at 1.965 g/cc. PETN from $500 < v < 1760$ (1 atm) cools from 520 to 360 K. HNB from $500 < v < 2960$ (1 atm) cools from 1050 to 710 K. Therefore, HNB is hotter, C_v is larger, and ω is smaller.

ω is, therefore, really a constant only at a defined 1 atmosphere temperature because C_v actually increases with temperature. For

$$C_v + A + BT, \tag{23}$$

Eq. (23) becomes

$$AlnT + BT = -RlnV, \qquad (24)$$

and no simple relation can be found. Including this would destroy the simplicity of the JWL. The result in practice is that the JWL ω, as derived from the cylinder for $2 < v < 7$, is larger than that calculated from CHEQ. Thus, ω for PETN is 0.57 in the JWL and 0.28 in CHEQ. ω for HNB has values of 0.28 in the JWL and 0.22 in CHEQ.

8. Generating Systematic JWL Constants

One of the disturbing results of the JWL is that the constants of different explosives show no apparent trends. This suggests that maybe too many constants are used and simplification is possible. However, the pressure and energy drop steeply from the detonation point, but change very slowly at large volumes. The transition from the A to the C term in the JWL is discontinuous, and for this reason, the B term was added to smooth it. A function that handles very different rates of change over 6 to 9 orders of magnitude is difficult to find.

Urtiew and Hayes made a clever attempt to unify the JWL situation.[16,17] They created dimensionless units based on the initial density times the square of the detonation velocity. Their relationships are

$$\begin{aligned}
&A/\rho_o D^2 = 5.35545 \\
&B/\rho_o D^2 = 0.094983 \\
&C/\rho_o D^2 = 0.0112292 \\
&R_1 = 4.41604 \\
&R_2 = 0.27R_1 \\
&\omega = 1/3 \\
&Pj/\rho_o D^2 = 0.2653 \\
&E_o/\rho_o D^2 = 0.204 - 0.0734\rho_o
\end{aligned} \qquad (25)$$

The results are shown below. We have taken the cylinder JWLs for 32 explosives and calculated the dimensionless constants.

	$A/\rho_o D^2$	$B/\rho_o D^2$	$C/\rho_o D^2$
Urtiew	5.355	0.095	0.011
average	5.518	0.095	0.017
st. dev	1.81	0.128	0.011
PETN	8.552	0.750	0.031
LX-17	8.925	0.157	0.013
LX-14	4.667	0.038	0.013
RX-26-AF	4.511	0.036	0.005

(26)

The average is close to the Urtiew/Hayes values, but the standard deviation is very large. PETN of 1.763 g/cc is far off, and we obtain E_o = 9.0 kJ/cc instead of the actual value of 10.3 kJ/cc or the JWL value of 10.8. The resulting PETN energies at the cylinder volumes of interest are about 10% low. In Chapter 5, we show that $\rho_o D^2$ is the spring constant for the compression of the explosive. It is not surprising that this value does not relate to the later time behavior of energy release, which depends on the kinetics of each reaction.

9. Variations of the JWL Function

Many attempts have been made to alter the form of the JWL. Most variations make it more complicated. The first of these is the temperature-dependent JWL used in the Ignition and Growth (I&G) model (see Chapter 7). It has the Gruneison form

$$P_s(v, T) = R_1 \exp(-R_5 v) + R_2 \exp(-R_6 v) + R_3 T/v. \qquad (27)$$

Although they are similar, this is a different equation from the regular JWL, which does not include temperature. Eq. (27) is a true Gruneison EOS, which is defined by[18,19]

$$P = P_o + \rho_o \omega(v) E_t(v,T) / v, \qquad (28)$$

where P_o is the pressure at 0 K and E_t is the thermal energy. Thus, we split the energies into the cold energy of compression and the energy solely involved in heating it.

The second, more complicated, form is that of E. L. Baker, which is called the JWLB EOS. In this form, the adiabat is given by[20,21]

$$P_s = \sum_i A_i\left(1 - \frac{\lambda}{R_i v}\right)\exp(-R_i v) + \frac{\lambda E_s}{v} + C\left(1 - \frac{\lambda}{\omega}\right)v^{-(\omega+1)}, \tag{29}$$

where

$$\lambda = \sum_i (A_{\lambda i} v + B_{\lambda i}) \exp(-R_{\lambda i} v) + \omega. \tag{30}$$

In addition to the detonation velocity and the usual detonation parameters, there are 16 constants in the JWLB EOS for octol. (The JWLB has been placed in DYNA2D and is available at LLNL.)

A more complex version of the JWL by E. Lee et al. seeks to make ω a function of volume.[22] The pressure adiabat is given by

$$P_s = A\exp(-R_1 v) + B\exp(-R_2 v) + C/v^{\omega+1} + av^2/(1 + bv^2)^2, \tag{31}$$

which adds two more constants.

A final version was designed by Miller and Guirguis for composite explosives in which energy comes out at long times.[23] The late energy caused by burning the aluminum is λQ. The JWL adiabat becomes

$$P_s = A(1 - \omega/R_1 v)\exp(-R_1 v) + B(1 - \omega/R_2 v)\exp(-R_2 v) + \omega(E_s + \lambda Q)/v, \tag{32}$$

where

$$d\lambda/dt = a(1-\lambda)^{1/2} P_s^{1/6}, \tag{33}$$

where a is a constant. Then,

$$\lambda = 1 - \frac{a^2}{4}\left[\int_0^t p^{1/6}(t)\, dt\right]. \tag{34}$$

Near the detonation point, the integral is large, and $\lambda \sim 0$. At long times, with P_s small, the integral is small, and λ is large. More energy is then added to the last term.

10. References

1. J. W. Kury, H. C. Hornig, E. L. Lee, J. L. McDonnel, D. L. Ornellas, M. Finger, F. M. Strange, and M. L. Wilkins, "Metal Acceleration by Chemical Explosives," *Proceedings of the Fourth Symposium (International) on Detonation,* White Oak, MD, October 12–15, 1965, pp. 3–12.

2. E. L. Lee, H. C. Hornig, and J. W. Kury, *Adiabatic Expansion of High Explosive Detonation Products,* Lawrence Livermore National Laboratory, Livermore, CA, UCRL-50422 (1968).

3. E. Lee, D. Breithaupt, C. McMillan, N. Parker, J. Kury, C. Tarver, W. Quirk, and J. Walton, "The Motion of Thin Metal Walls and the Equation of State of Detonation Products," *Proceedings of the Eighth Symposium (International) on Detonation,* Albuquerque, NM, July 15–19, 1985, pp. 613–624.

4. R. M. Doherty, J. M. Short and M. J. Kamlet, *Combus. Flame* **76,** 297 (1989).

5. H. Hornberg and F. Volk, *Propellants, Explosives, Pyrotechnics* **14,** 199 (1989).

6. P. C. Souers and J. W. Kury, *Propellants, Explosives, Pyrotechnics* **18,** 175 (1993).

7. B. Hayes. "On Electrical Conductivity in Detonation Products," *Proceedings Fourth Symposium (International) on Detonation,* White Oak, MD, October 12–15, 1965, pp. 595–601.

8. D. L. Ornellas, *Calorimetric Determinations of the Heat and Products of Detonation for Explosives: October 1961 to April 1982,* Lawrence Livermore National Laboratory, Livermore, CA, UCRL-52821 (1982), pp. 57–61.

9. H. C. Hornig, E. L. Lee, M. Finger, and J. E. Kurrle, "Equation of State of Detonation Products," *Proceedings Fifth Symposium (International) on Detonation,* August 18–21, 1970, Pasadena, CA, p. 503.

10. L. Green, N. Holmes, and J. Kury, "Shock Measurements on Explosives in the Supra-Compressive Region," presented at the Int'l Symposium on Pyrotechnics and Explosives, Beijing, China, October 12–15, 1987; Lawrence Livermore National Laboratory, Livermore, CA, UCRL-95461 (1987).

11. R. Clarkson, memo to R. Simpson, February 26, 1993.

12. B. M. Dobratz and P. C. Crawford, *LLNL Explosives Handbook,* Lawrence Livermore National Laboratory, Livermore, CA, UCRL-52997 (1985), pp. 8-21–8-23.

13. Memo from E. Lee to S. Cochran, November 28, 1985; the memories of J. Kury and C. Tarver.

14. E. L. Baker, *Modeling and Optimization of Shaped Charge Liner Collapse and Jet Formation,* U.S. Army Research, Development, and Engineering Center, Picatinny Arsenal, NJ, Report ARAED-TR-92019 (1993).

15. E. L. Baker, Picatinny Arsenal, NJ, private communication, 1993.

16. P. A. Urtiew and B. Hayes, *Empirical Estimate of Detonation Parameters in Condensed Explosives,* Lawrence Livermore National Laboratory, Livermore, CA, UCRL-JC-103219 (1990).

17. P. A. Urtiew and B. Hayes, "Parametric Study of the Dynamic JWL-EOS for Detonation Products," presented at the Third Int'l Lavrentiev's Readings Conference, Novosibirsk, USSR, September 10–14, 1990; Lawrence Livermore National Laboratory, Livermore, CA, UCRL-JC-103218 (1990).

18. D. O'Keeffe and J. D. Pastine, *Metallurgical Effects at High Strain Rates,* R. W. Rohde, B. M. Butcher, J. R. Holland and C. H. Karnes, eds. (Plenum, New York, 1973), pp. 157–169.

19. D. O'Keeffe, *J. Geophys. Research* **75,** 1947 (1970).

20. E. L. Baker, *An Explosives Products Thermodynamic Equation of State Appropriate for Material Acceleration and Overdriven Definition: Theoretical Background and Formulation,* ARDEC Report ARAED-TR-91013, Picatinny Arsenal, NJ (1991).

21. E. L. Baker and J. Orosz, *Advanced Warheads Concepts: An Advanced Equation of State for Overdriven Detonation,* ARDEC Report ARAED-TR-91007, Picatinny Arsenal, NJ (1991).

22. E. L. Lee, M. Van Thiel, L. G. Green and A. Mitchell, "Detonation Product EOS: The Region Above Chapman Jouget Pressure," in *Shock Waves in Condensed Matter–1983,* J. R. Asay, R. A. Graham and G. K. Straub, eds. (Elsevier Science Publishers, 1984), pp. 617–620.

23. P. J. Miller and R. H. Guirhuis, "Experimental Study and Model Calculations of Metal Combustion in Al/AP Underwater Explosives," *Materials Research Society, Symposium Proceedings,* **296** 199–304 (1993).

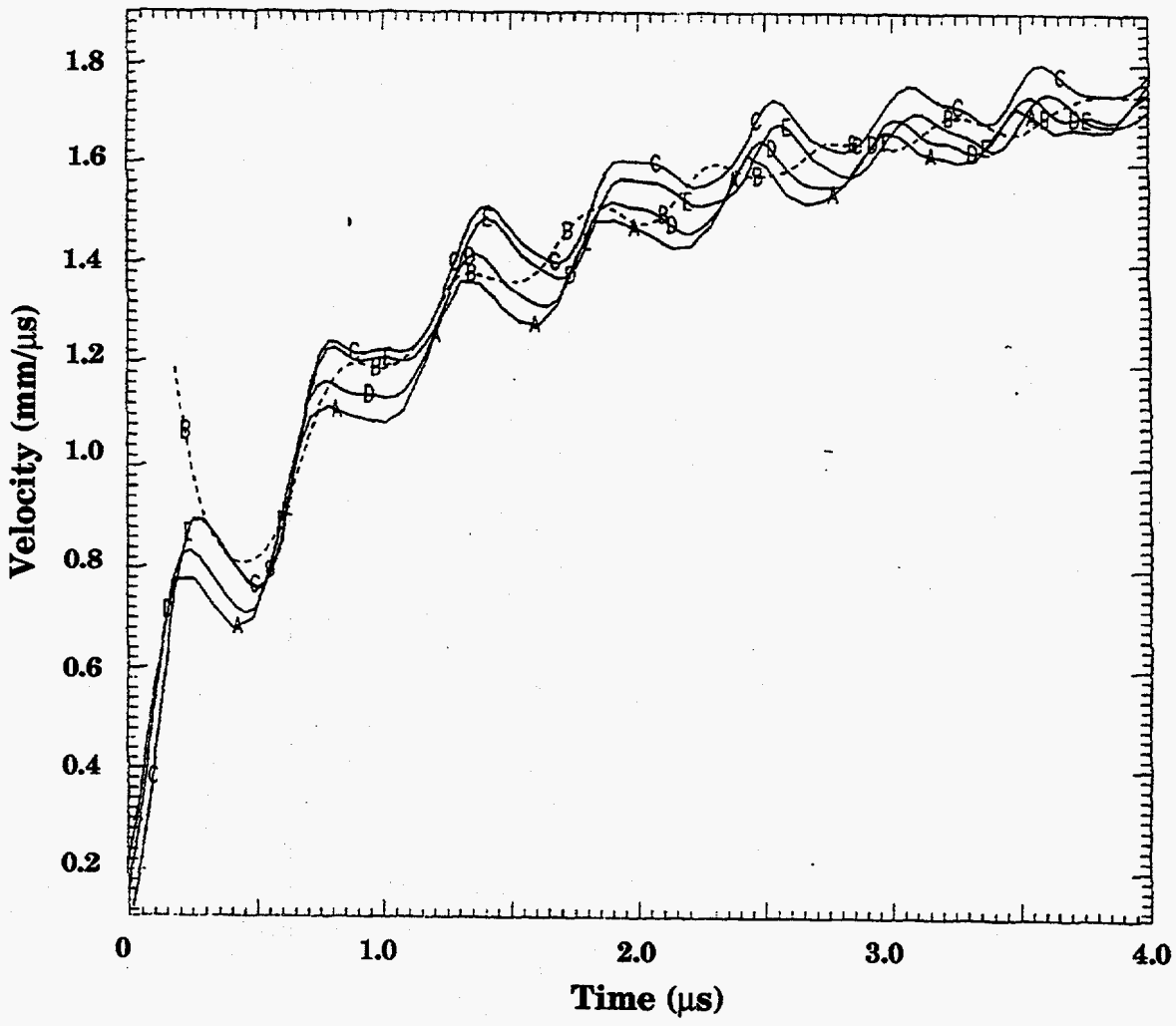

Fig. 3-1. DYNA2D runs for LX-17 in the cylinder test. Unconfined wall velocity is plotted against the scaled 25 mm-diameter time. A JWL with a 30-GPa detonation pressure fits the jump-off velocity but not the behavior at 4 μs. A 26-GPa JWL shows the reverse. The data are curve B, a smoothed average of the streak camera data in cylinder numbers 470, 471, 522, and 523. The DYNA curves with the JWL detonation pressures and the A coefficients are: curve A 26 GPa, A = 9.326; C Haselman's 30 GPa, A = 4.603; D 28 GPa, A = 6.205; E 30 GPa, A = 4.572.

Table 3-1. Comparison of historical JWLs used for LX-14 and LX-17. Although Mbar units are used for the JWLs, the energies are in kJ/cc.

	LX-14, 1.830 to 1.835 g/cc, 8.80 to 8.83 mm/μs			LX-17, 1.900 to 1.905 g/cc, 7.596 to 7.63 mm/μs		
	New from cylinder	Old cylinder f. Handbook	JWL no. 381	New from cylinder	Old cylinder f. Handbook	JWL no. LH
A (Mbars)	6.614142	8.261	7.5598	9.897607	4.46	4.603
B (Mbars)	0.054007	0.1724	0.2267	0.174413	0.01339	0.09544
C (Mbars)	0.018257	0.01296	0.009825	0.014271	0.01306	0.01265
R_1	4.118	4.55	4.44	5.15	3.85	4.00
R_2	0.95	1.32	1.5	1.713	1.03	1.70
ω	0.40	0.38	0.3	0.45	0.46	0.48
v_j	0.732	0.740	0.734	0.766	0.727	0.726
P_j (GPa)	38.0	37.0	38.1	26.0	30.0	30.0
E_o (J/cc)	10.8	10.2	10.1	7.0	6.9	6.9
E_d(v=2)	6.75	6.95	6.95	4.54	4.78	4.94
E_d(v=4)	8.09	8.15	7.92	5.31	5.43	5.56
E_d(v=7)	8.63	8.52	8.23	5.63	5.71	5.83

Table 3-2. Set of JWLs for 1.763 g/cc PETN that give the right answer to a Cylinder Test. These were run in the Baker cylinder model for a 25-mm-diameter, half-wall cylinder until the experimental velocities of 2.09 and 2.38 mm/μs, each ± 0.02 mm/μs, were obtained. All detonation velocities are 8.274 mm/μs. The detonation pressure is in GPa, the detonation energies E_o and E_d are in kJ/cc, the velocities at jump-off and the 5th dip for the plate are in mm/μs, and all other units are in Mbar. The text describes how these JWLs are narrowed to standard values. Both JWL no. 5 and 6 meet the standard conditions.

No.	1	2	3	4	5	6	7	8
P_j	34.5	34.5	32.0	32.0	31.0	32.0	28.5	28.5
E_o	12.0	10.8	10.8	10.8	10.3	10.8	10.8	9.6
A	5.5338	5.0536	23.8298	14.9186	10.2432	7.6647	31.6650	16.3837
B	0.8229	0.6312	1.6003	1.3337	0.3272	0.2834	0.5394	0.1758
C	0.0226	0.0282	0.0306	0.0310	0.0304	0.0296	0.0316	0.0307
R_1	5.0	4.7	8.0	7.0	5.5	5.0	7.3	6.0
R_2	2.35	2.30	2.8	2.7	1.75	1.75	2.00	1.25
ω	0.35	0.50	0.52	0.52	0.60	0.52	0.55	0.80
E_d(1.5)	5.29	5.23	5.18	5.10	4.92	4.93	4.85	4.63
E_d(2.2)	6.89	6.82	6.77	6.71	6.74	6.68	6.74	6.66
E_d(6.5)	8.64	8.59	8.58	8.54	8.65	8.65	8.75	8.74
jump-off	1.65	1.65	1.55	1.54	1.49	1.53	1.39	1.38
5th dip	3.12	3.09	3.05	3.01	2.91	2.94	2.83	2.75

Table 3-3. Comparison of measured calorimetric total energies of detonation with those derived from the cylinder JWLs. The final, adjusted total energies of detonation, as derived from the calorimeter, E_0, are in bold. The agreement between the calorimeter and the cylinder for these homogeneous explosives is better than expected. All heats and energies are in kJ/cc.

Explosive	Measured density (g/cc)	Measured confined heat of detonation (kJ/cc)	Our densities (g/cc)	Adjusted measured heat of detonation (kJ/cc)	Energy of Detonation (kJ/cc) from heat of detonation	Energy of Detonation (kJ/cc) from JWL fit
BTF	1.86	10.98	1.852	10.93	**11.2**	11.3
1,2-DP	1.265	7.09	1.26	7.06	**7.2**	6.9
FEFO	1.607	8.56	1.607	8.60	**8.3**	8.2
HMX	1.89	11.70	1.893	11.71	**11.0**	11.0
HMX	1.20	6.63	1.188	6.56	**6.2**	6.4
HNB	1.918	13.27	1.965	13.59	**13.7**	13.2
HNS	1.649	7.58	1.655	7.61	**7.5**	7.5
HNS	1.017	3.74	1.001	3.68	**3.7**	3.6
NM	1.13	5.80	1.13	5.80	**5.2**	5.0
PETN	1.732	10.81	1.763	11.01	**10.3**	10.8
PETN	1.496	9.41	1.503	9.46	**8.9**	8.5
RX-23-AA	1.424	7.98	1.424	7.98	**6.5**	6.5
RX-23-AB	1.356	6.24	1.356	6.24	**4.3**	4.1
RX-23-AC	1.136	4.66	1.136	4.66	**4.1**	4.5
TATB	1.87	7.96	1.83	7.92	**7.3**	7.3
TNT	1.533	7.01	1.632	7.46	**7.1**	7.1

Chapter 4. Cylinder Analysis

1. Cylinder Relative Volumes with Wall Thinning

What makes the Cylinder Test a "test" is that the relative volume may be determined directly from the cylinder expansion by calculating volume segments of the cylinder. In Chapter 2, we considered a wall of constant thickness and arrived at volumes of 2.2, 4.1, and 6.5 for perpendicular streak camera expansions of 6, 12.5, and 19 mm with a 25-mm-diameter cylinder.

However, one should include the thinning of the wall as the cylinder expands. Then, on the horizontal line just defined, we initially define the geometric relative volume, v_g, as

$$v_g \sim \{ [S_0 + (R - R_0)] / S_0 \}^2, \tag{1}$$

where S_0 and R_0 are the initial inner and outer radii and R is the outer radius at a later time. If we let W_0 be the initial wall thickness and W be the thickness at a later time, the decreased wall thickness at time t is given by

$$W \sim \{R_0 / R\} W_0. \tag{2}$$

The decreased wall thickness $W_0 - W$ is now added as gas space, and we obtain the new geometric volume

$$v_g \sim \{[S_0 + (R - R_0) + (W_0 - W)] / S_0\}^2. \tag{3}$$

The results are now dependent on the initial wall thickness, and we have a different set of values for the half- and full-wall cylinders, as listed below.

Distance $R - R_0$ (mm)	Relative Volumes, v_g		
	Constant wall, approx.	Thinning wall	
		Half-wall	Full-wall
6	2.2	2.26	2.36
12.5	4.1	4.14	4.34
19	6.5	6.53	6.84

(4)

One would then have to compare the corrections for wall motion from the hydrocodes. A correction for wall thinning has not yet seemed important enough to add, considering the accuracy of the JWL.

2. Comparing Streak and Fabry Data

The streak camera and the Fabry interferometer measure different things on the cylinder.[1,2] To see this, we consider the schematic in Fig. 4-1. The cylinder is vertical, with the central axis lying along A'B', the original wall along AB, and the detonation wave of velocity, D, moving upward. The cylinder wall is blown outward to the line BC, and all later surfaces will be parallel to BC (and farther out). At the time of Fig. 4-1, the wall has swung out from the vertical, as though on a hinge, from point B. The streak camera looks in at point C and so constantly sees new points from below on the cylinder. The Fabry looks in at point E along the line AE and so sees a point at A on the cylinder at t = zero.

In the simple "hinged wall" model, the wall has swung along the arc AE, which is very close to the straight line AE. Thus, the Fabry path AE is close to the path of the same point on the wall and is the one-dimensional path of interest. The streak camera, looking at point C, however, sees a new wall moving constantly upward into its field of view.

In this simple model, velocities and distances are assumed to be proportional to the geometry shown (strictly, the velocities change with time and hold only for a differentially small set of triangles). Because of the hinge, the distances AB = BE. The angle of the hinged wall to the original wall is ABF = Θ_s; the 7 or 8° angle of the Fabry line-of-sight to the horizontal is EAC = Θ_p. Because angle BAF = $90° - \Theta_s$, angle FAC = Θ_s. Because two sides of the triangle ABE are the same, angles BAE = BEA = $90° - \Theta_s/2$. The right angle BAC is composed of the sum of angles BAE and EAC so that angle BAC = 90° = $90° - \Theta_s/2 + \Theta_p$. Then

$$\Theta_s = 2\Theta_p. \tag{5}$$

From triangle AEF with angle FAE = $\Theta_s - \Theta_p$, we obtain, using Eq. (5),

$$u_d = u_f \cos(\Theta_s - \Theta_p) = u_f \cos \Theta_p. \tag{6}$$

From triangle ACF, using Eq. (5),

$$u_d = u_s \cos\Theta_s = u_s \cos 2\Theta_p. \tag{7}$$

Then the approximate Fabry path, from Eqs. (5) and (6), is

$$u_f / u_s = \cos 2\Theta_p / \cos \Theta_p = 0.978 \text{ for } \Theta_p = 7°, \\ = 0.971 \text{ for } \Theta_p = 8°. \tag{8}$$

We may obtain the actual value of u_s from triangle ABC and angle ABC:

$$u_s = D\tan\Theta_s = D\tan 2\Theta_p. \tag{9}$$

Also, the arc distance AE is found from

$$AE/\Theta_s = AE/2\Theta_p = 2\pi D/360^o, \tag{10}$$

so that

$$u_f/u_s \sim AE/u_s = 4\pi\Theta_p / 360^o\tan 2\Theta_p = 0.980 \text{ for } \Theta_p = 7^o, \\ = 0.974 \text{ for } \Theta_p = 8^o. \tag{11}$$

The Fabry path length is always shorter than that of the streak camera.

In practice, the outer radial displacements $R - R_0$ of 6, 12.5, and 19 mm will be used for both streak and Fabry analysis. For the streak camera, it is directly measured; for the Fabry, it is obtained by integration of the velocity. The time scales are different (it will take longer for the Fabry to reach the same displacement), and of course, the paths are different.

At LLNL, our experience leads us to set the Fabry angle, Θ_p, to 7° as the best value over the course of a cylinder shot. L. Green notes that the angle may be larger in the early stages of the shot and that it may be a degree larger for a more powerful explosive. The accuracy of this model can be demonstrated with RX-48-AA (92.4% ABNBF/7.6% Kel-F) in Fig. 4-2. At the same time, the Fabry velocity lies just below the streak velocity. The scatter in the streak data, created by the differentiation from the displacement, is obvious. The ratio of streak/Fabry is just below 1 and is constant after just a few microseconds. Such comparisons of Fabry and streak camera data allows us to ascertain the overall accuracy of the entire experiment.

A larger list of cylinder data is given in Table 4-1, where we list the Fabry/streak velocity ratios at given times. The streak camera $R - R_0$ data have been summed for the four cameras, then differentiated and smoothed five times. One set of unsmoothed data is shown for comparison. The two Fabry velocities are averaged. The ratios are presented from 3 μs (of scaled 25-mm-diameter time) to the end of the Fabry trace and also for the last 2 μs of the trace. We conclude that the Fabry/streak ratio is constant beyond 3 μs. For the HMX-level explosives, the average ratio is 0.968, and for the TATB-level explosives, it is about 0.975. This offers evidence that a Fabry angle of 8° may be better for the more powerful explosives.

The Fabry angle is expected to change with time. A simple velocity description might be

$$u = G[1 - \exp(-gt)] + Ht^{1/2}, \quad (12)$$

where u is either a streak or Fabry velocity and G, g, and H are constants. Eq. (12) is acceptable because the acceleration will approach zero at long times. More terms could be used to fit real data. The angle is

$$\Theta_p = \Theta_s/2 = (1/2)\tan^{-1}[(R - R_o)/Dt], \quad (13)$$

where

$$R - R_o = G[t + \exp(-gt)/g] + 2Ht^{3/2}/3. \quad (14)$$

At short times, the exponential decay dominates and the angle decreases. At long times, the exponential is gone and the argument in brackets in Eq. (13) becomes $[G + 2Ht^{1/3}/3]/D$. Because H is a small number, we expect the increase of the angle at long times to be gentle. The minimum angle is expected when the exponential dies and Eq. (12) returns to its slower mode of behavior.

3. Cylinder Codes with PETN

Two codes were run with 1.763 g/cc PETN in a half-wall copper cylinder as part of the process of establishing the pedigree of the standard JWL (Chapter 3, Eq. (9)). Both codes are explicit Lagrangian.

We first ran in DYNA2D,[3] with cylinder dimensions of 150-mm length, 12.7-mm inner radius, and 14.0-mm outer radius. The zoning was 300 elements long by 12 wide for a total of 7525 nodes and 7200 elements. This was 0.50 mm/zone axially, 1.06 mm/zone radially in the PETN, and 0.11 mm/zone in the copper. The wall and explosive were merged, and a stonewall was run across the bottom, where 300 elements were lit at time zero by program burn. The detonation then proceeded upward. The artificial viscosity parameters were increased slightly to 2.0 and 0.10 for a slight filtering effect.

The code was rezoned twice for speed. The detonation reached the top of the cylinder at about 18 μs. At 19 μs, a rezoning removed the bottom 2 cm and the top 1 cm. If rezoning was not done, zone-tangling resulted that slowed down the run considerably. At 23 μs, the run was rezoned, with the top and bottom 1 cm removed. The run stopped at 27 μs; total CPU time was about 6 1/2 minutes on a Cray YMP. The effect of not rezoning was to add extra steps to the calculation, as may seen from the "dt" parameter. The time step started at about 0.008 μs and decayed to 0.0008 μs at 19 μs. Rezoning boosted it to 0.004 μs, and it decayed to 0.0008 μs again at 23 μs. Rezoning put it back to 0.003 μs for the last run.

The observed slit height was at 9.5 cm out of the 15 cm total. For PETN, this should be reached at just over 11 μs. In DYNA2D, the run was usually

sent with one dump to 10 μs. A restart deck was run from 10 to 27 μs with a dump time of about 0.06 μs. In order not to overload the output, the rule used was

$$\text{Time between dumps } (\mu s) \sim 5 \times 10^{-7} \text{ (no. of zones)(run time in } \mu s). \quad (15)$$

A second means of running, which generates almost no output files, is to set the dump to ORION for every 3 μs (so there is something to monitor), but to collect the main data using DYNACYL. This DYNA2D modification was created by M. Murphy. It determines a set of velocities and pressures at selected points on or in the cylinder wall. Both the streak and the Fabry velocities are obtained.

Using 300-zone lighting, steady state for PETN is achieved in 6 cm, whereas 10 cm is required if only a single line of elements are lit. With 100 zones, it requires an 8-cm length. The addition of a type-1 slide line along the explosive-metal interface may seem more physical, but it greatly increases the zone tangling, and the results are not worth the effort. The simple material model for copper with the cut-off (spall) pressure of –0.012 Mbar is quite good.

Several types of velocity output must be considered in DYNA2D. The ORION output is either the pure radial velocity or the maximum velocity in an element. The DYNACYL program differentiates between streak and Fabry velocities.

The second code is HEMP.[4] The cylinder length was 210 mm with the same widths as in the first model, but unlike DYNA, the cylinder is horizontal. A type-1 slideline was placed between the explosive and the metal, and stonewalls were placed at the ends. A program burn along the left edge (bottom of the cylinder) was used. The detonation proceeded horizontally from left to right. The Steinberg-Guinan copper model (spall 1) was used with the cut-off (spall) pressure of –0.012 Mbar.[5] The artificial viscosity was set at 0.5 for mild smoothing. Steady state was achieved in about 75 mm of axial distance.[5] The code ran with no rezoning in just under 90 minutes on the Cray YMP.

The DYNA2D mesh has so few zones in the metal that there was no hope of adequately reproducing the oscillations of the shock wave in the metal. However, HEMP added zones to the metal just as the detonation reached the slit point at 16 cm. In the explosive, the zoning was 0.05 mm/zone axially on the cylinder and about 1 mm/zone radially. In the copper, the zoning was about 0.025 mm/zone axially and radially. (If extended to the entire 210-mm-long cylinder in the DYNA2D manner, it would require 50,000 zones in the explosive and 400,000 zones in the copper.). This was sufficient to reproduce the shock wave oscillations. The HEMP cylinder must be close to being zoned to convergence, as long as a JWL, which simulates an ideal explosive, is being used.

The results of the code runs on PETN are summarized in Fig. 4-3. All four streak camera results from shot no. 511 are plotted, and the HEMP result, first run by John Walton, runs through them. The less highly-zoned DYNA2D models fall in different places. The best agreement in DYNA was obtained by using the maximum velocity (element variables component number 27).[6] We note that the agreement with HEMP is not perfect at long times, so that more work is probably needed if PETN is to be used as a standard. In summary—to get an accurate EOS result from the cylinder, the problem must be zoned to convergence.

Fig. 4-4 shows the calculated Fabry/streak camera ratio, as a function of time, as calculated in the two codes run with a 7° Fabry angle. The three horizontal dashed lines represent, from top to bottom, the "hinge model" prediction for 7, 8, and 9° angles. We see that the ratios decrease in both models toward a steady state value, indicating that the angles start at 7° and increase slightly with time.

Finally, because this section uses the codes in an effort to confirm the standard PETN JWL, we include several 1-D plate runs, which are shown in Fig. 4-5. The data are from electric gun shot ppe88003 with 10-mm PETN and 0.25-mm tantalum. Further details of this shot are listed in the tables of Chapter 5. We note the excellent agreement of the jump-off and the first three wiggles with the codes, both the LLNL 1-D code and DYNA2D. Although zoned to convergence, the wiggles get out of phase at long times. The tantalum cutoff pressure of –0.044 Mbar was used, but the results are otherwise independent of the material model used.

4. References

1. E. Lee, D. Breithaupt, C. McMillan, N. Parker, J. Kury, C. Tarver, W. Quirk, and J. Walton, "The Motion of Thin Metal Walls and the Equation of State of Detonation Products," *Proceedings Eighth Symposium (International) on Detonation,* Albuquerque, NM, July 15–19, 1985, p. 613.

2. David Goosman, private communication, 1993.

3. J. O. Halquist, *User's Manual for DYNA2D,* Lawrence Livermore National Laboratory, Livermore, CA, UCID-18756, Rev. 3 (1988). The runs shown here were done under NLTSS.

4. E. L. Lee, H. C. Hornig and J. W. Kury, *Adiabatic Expansion of High Explosive Detonation Products,* Lawrence Livermore National Laboratory, Livermore, CA, UCRL-50422 (1968).

5. D. J. Steinberg, *Equation of State and Strength Properties of Selected Materials,* Lawrence Livermore National Laboratory, Livermore, CA, UCRL-MA-106439 (1991).

6. J. O. Hallquist and J. L. Levatin, *Orion : An Interactive Color Post-Processor for Two Dimensional Finite Element Codes,* Lawrence Livermore National Laboratory, Livermore, CA, UCID-19310, Rev. 2 (1985), p. 18.

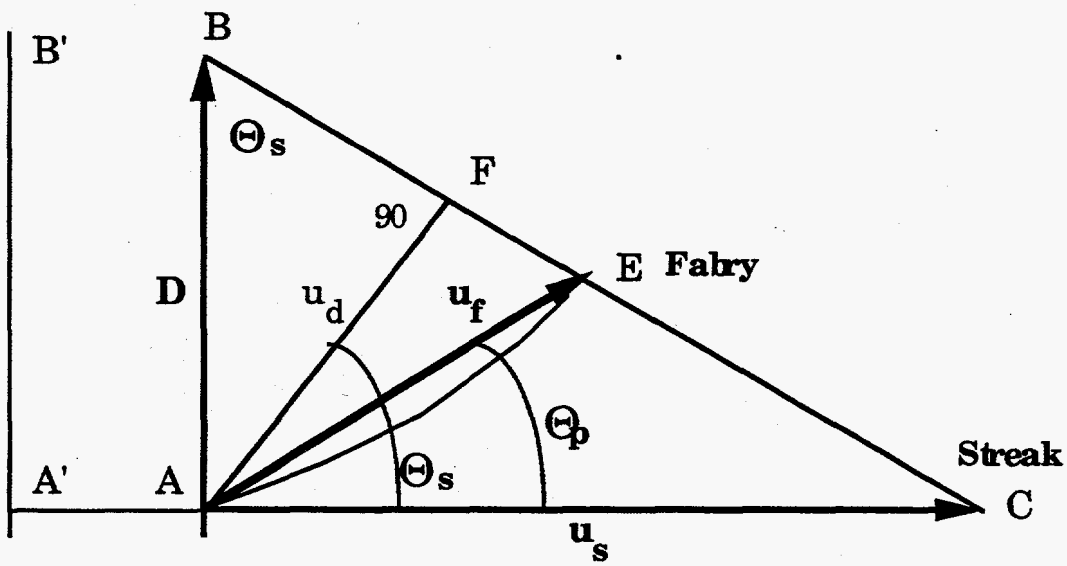

Fig. 4-1. Geometry of the Fabry/streak camera conversion using the simple "hinged wall" model. The cylinder axis lies along A'B' and the initial cylinder wall lay along AB. The detonation velocity, D, moves upward along AB. The Fabry beam looks along AE, and the particle velocity of the outer cylinder wall, u_f, lies approximately on this line. The velocity u_f moves actually along the curved dashed line AE. The radial streak camera velocity, u_s, of the outer wall moves along AC. Line AE is the closest to a one-dimensional path of motion.

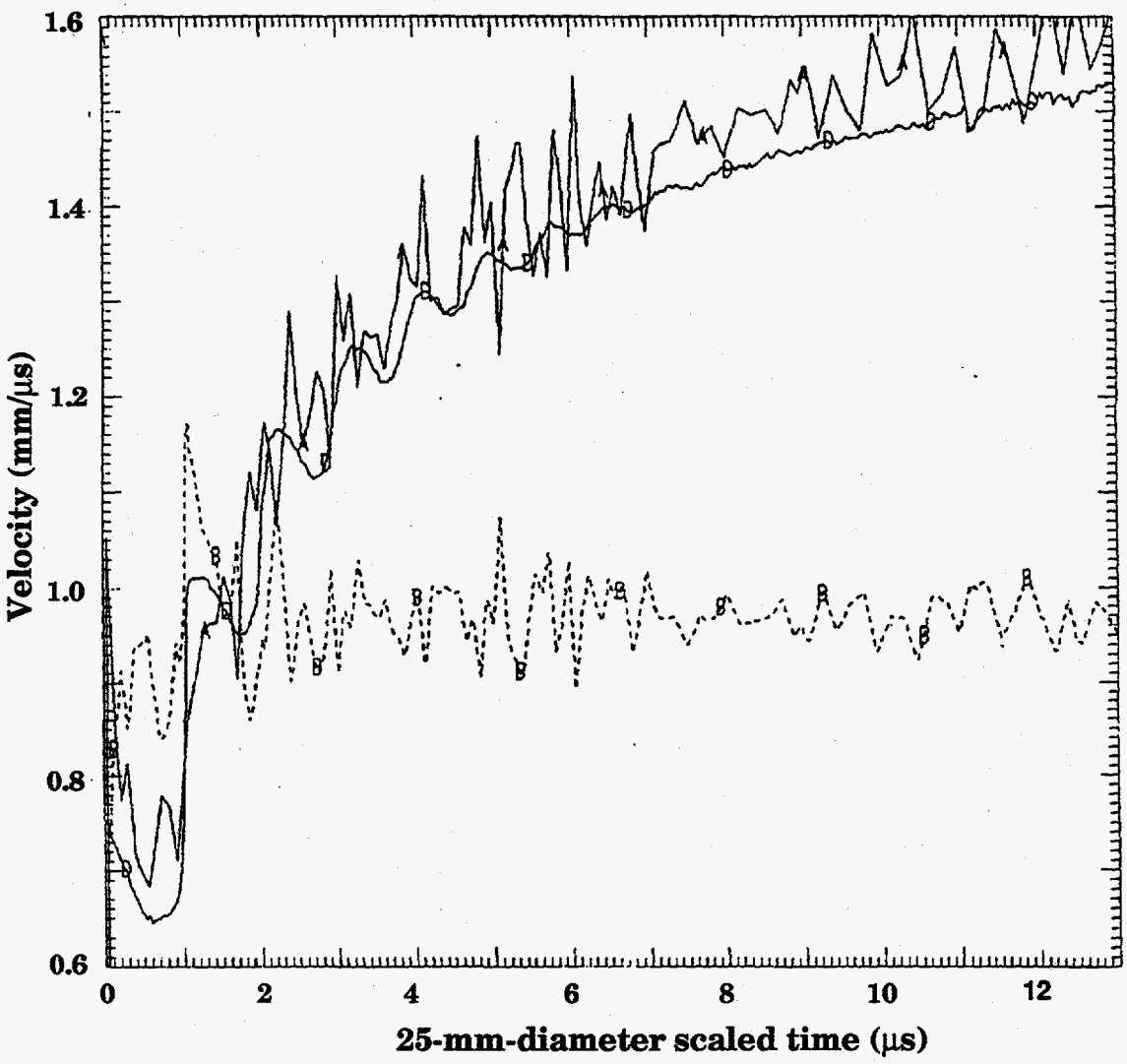

Fig. 4-2. Measured streak camera and Fabry cylinder velocities for shot no. 579 for RX-48-AA (92.4% ADNBF). The cylinder was 25 mm in diameter and full wall. The four streak cameras (A) are averaged as are the two Fabrys (D). The dashed curve (B) is the Fabry/streak ratio, and it is about 0.97 from 5 to 13 μs. The considerable scatter is derived from the differentiated streak camera data.

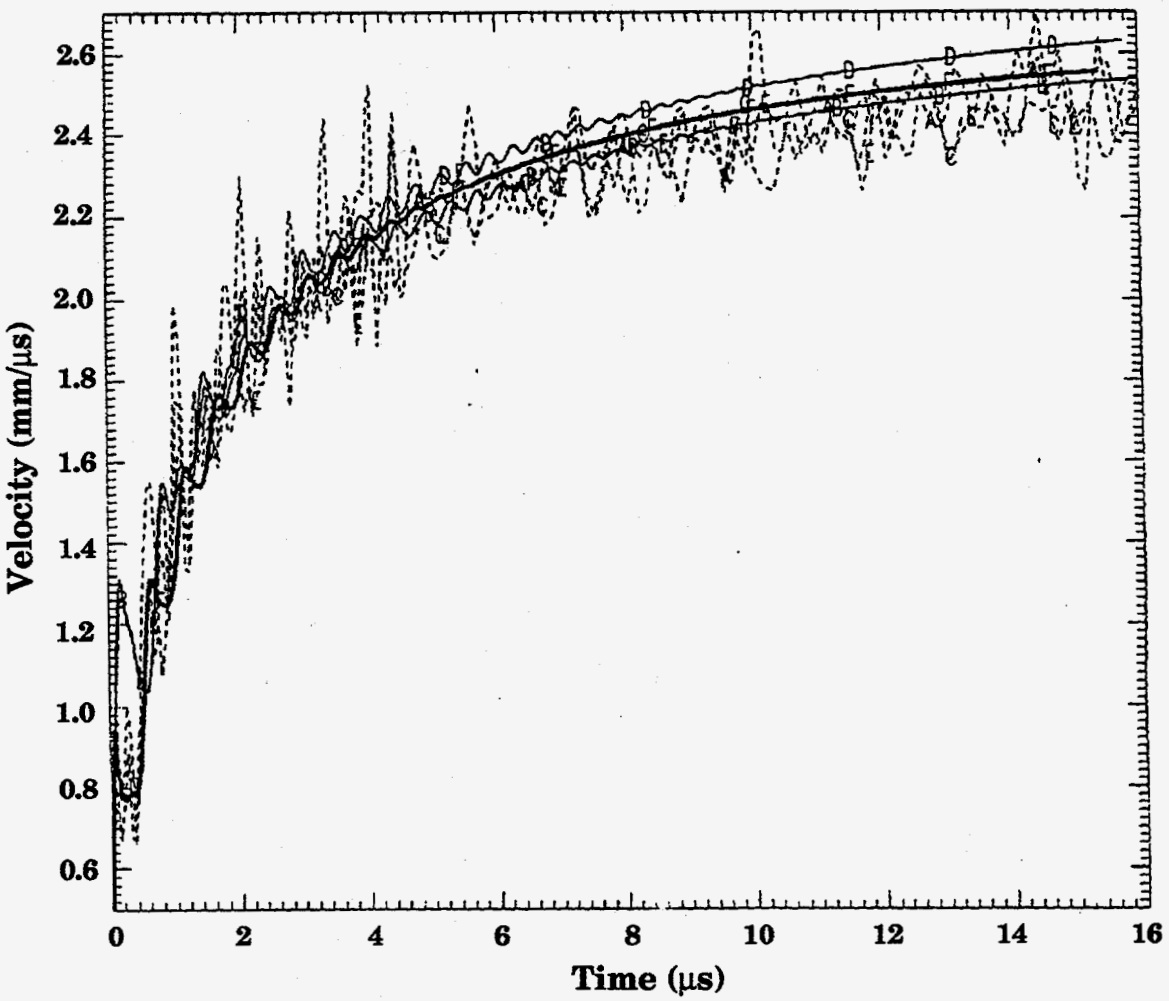

Fig. 4-3. Comparison of outer-wall cylinder streak camera velocities for PETN at 1.763 g/cc (dashed lines) as compared with several code runs that use the standard JWL. The best agreement is obtained from the radial velocity calculated in HEMP (heavy line). The light line below the HEMP result is the DYNA2D maximum velocity. The light line above the HEMP line is the DYNACYL result. The smaller zoned DYNA2D model best approximates the HEMP result and the data when the maximum velocity is used as output. The cylinder radius was 25 mm.

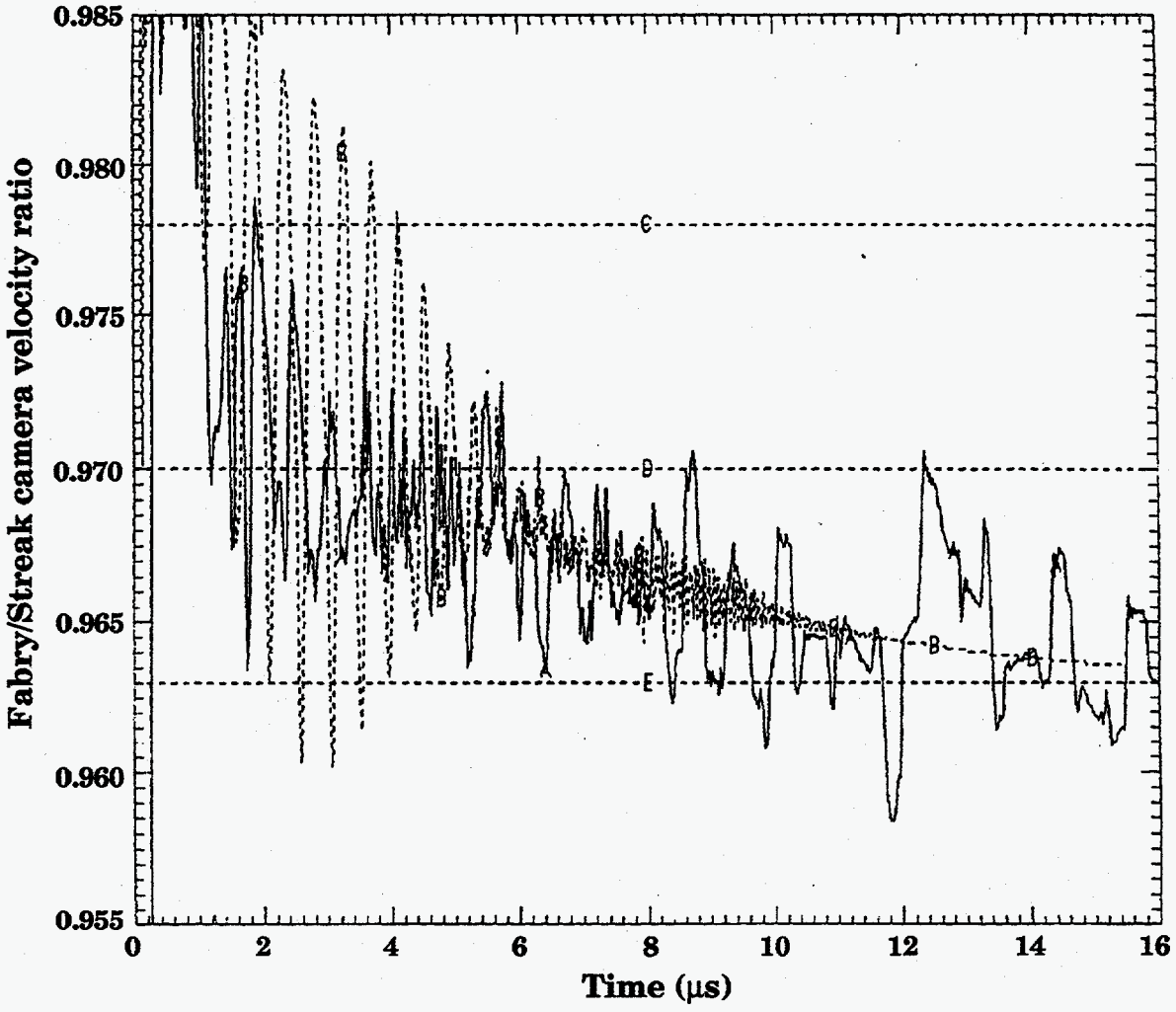

Fig. 4-4. The Fabry/streak camera velocity ratio as determined for 1.763 g/cc PETN in HEMP (dashed line) and in DYNACYL (solid line). The dashed horizontal lines indicate the predictions of the simple "hinged wall" model for 7, 8 and 9°, respectively. Although a 7° Fabry angle was used, an 8° angle appears to be slightly better.

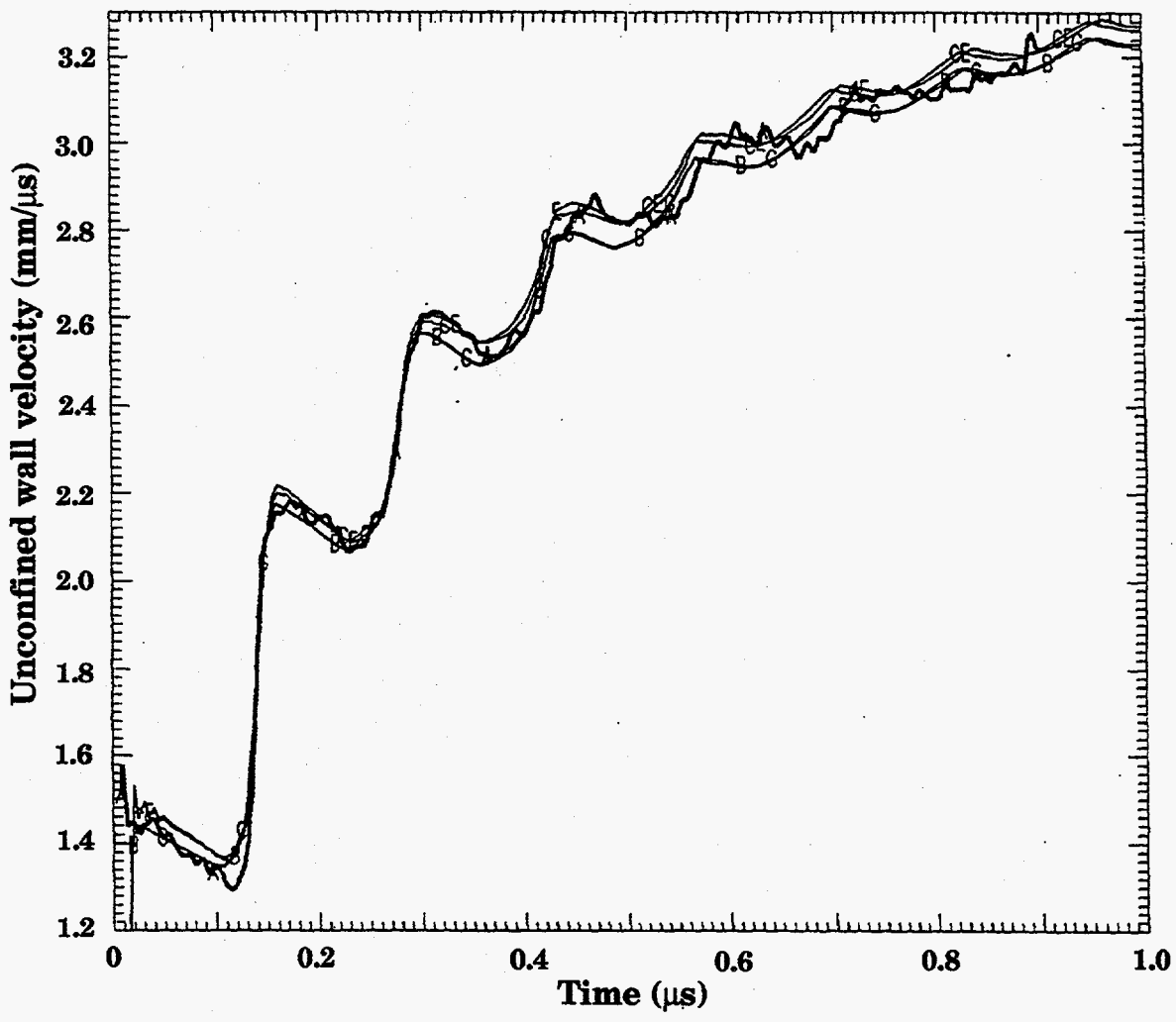

Fig. 4-5. Electric gun shot on 1.71 g/cc PETN (heavy line, shot ppe88003) showing the validity of the standard PETN JWL. The explosive length was 10 mm and the plate was 0.25-mm (10-mil) tantalum. The models are the 1-D code (B and G, low at long times) and DYNA2D (C and E, high at long times). We note that DYNA is slightly different from the 1-D and neither agrees with the wiggles, despite the zoning to convergence. Various material models are used, but they show no differences.

Table 4-1. Comparison of averaged streak camera and Fabry-Perot interferometer data at constant scaled times. "High" performance is HMX-level; "low" is TATB. No difference is seen for cylinder no. 579 as a function of smoothing.

Cyl. shot no.	Perfor-mance	No. of points	Smooth	Scaled time range (μs)	Fabry/streak velocity ratio at constant time		Last 2 μs Fabry/ streak ratio
					Average	Standard deviation	
547	high	335	5	3 to 9	0.962	0.008	0.961
549	high	344	5	3 to 10	0.962	0.009	0.958
555	high	277	5	3 to 9	0.982	0.008	0.984
560	high	270	5	3 to 12	0.965	0.012	0.959
580	high	710	5	4 to 12.5	0.969	0.011	0.970
554	low	308	5	3 to 10	0.978	0.012	0.984
573	low	287	5	3 to 11	0.981	0.007	0.978
574	low	484	5	3 to 10	0.981	0.007	0.980
575	low	251	5	3 to 11	0.980	0.006	0.982
579	low	1072	none	3 to 13	0.971	0.024	0.973
579	low	1072	5	3 to 13	0.970	0.010	0.970
579	low	1072	10	3 to 13	0.970	0.009	0.970
585	low	332	5	3 to 15	0.968	0.009	0.961

Chapter 5. Cylinder Data

1. Jump-Off Velocity and Detonation Pressure

Historically, the cylinder was the first LLNL test to refine the JWL . We have culled the LLNL records for the most often-fired explosives and listed their wall velocity results in Table 5-1. These include many of the more modern half-wall shots. All wall thickness are greater or equal to the reaction zone lengths. Most cylinder data were taken by streak camera, with only a few Fabry runs. The streak camera data were obtained by direct differentiation of the four channels of unsmoothed raw data, so that the error was ±0.15-0.3 mm/μs, with ±0.2 mm/μs the average. The Fabry data showed same-sample precisions of ±0.1 mm/μs for the PETN, ±0.03-0.05 for the LX-14, and ±0.02 mm/μs for the LX-17.

Table 5-2 lists wall velocity data taken over many years on homogeneous explosives, both liquid and solid. These should be directly comparable to TIGER results so that any analysis of JWLs to chemical composition would take place here. The data, however, are almost all old full-wall shots and are less reliable than those of Table 5-1.

The data presented here cover a long time. The cylinder shot numbers 100, 200, 300, 400, and 500 come from 1963, 1965, 1974, 1976, and 1984. Virtually all of it is taken by streak camera; Fabry interferometer data appear in the early 500s.

The data include measured unconfined wall velocities for the jump-off, at v = 2.2 ($R - R_0$ = 6 mm), v = 4.1 (12.5 mm), v = 6.5 (19 mm), and the last measured value. The streak-measured jump-off velocities, u_p, have never been considered accurate or important, and there is no equation to relate them to detonation pressures as we do in one dimension with plates. However, we may average the PETN data and relate it to the 31-GPa adiabat pressure, as determined by supracompression in Chapter 6. We have

$$P_p \sim 34.7 u_s^{\circ}. \qquad (1)$$

We use Eq. (1) to calculate detonation pressures from the cylinder jump-off. The best results are from Table 5-1, which we summarize here.

	Average jump-off velocity (mm/μs)	Calc det'n pressure (GPa)	Standard deviation pressure (GPa)	Cylinder JWL det'n pressure (GPa)
LX-14	1.06	37	3	38
PBX-9404	0.99	34	5	38
PETN	0.89	31	3	32
RX-26-AF	1.04	36	2	34
LX-17	0.92	32	4	26

(2)

The error in measuring the streak camera jump-off is ±0.1 mm/μs at best and creates the standard deviation in precision seen above. The first three are in agreement, given the wide spread of values. The discrepancy between values for LX-17 is most obvious. The 32-GPa value seen here is consistent with the spike pressure, as estimated from Ignition & Growth. It quickly decays, and the total JWL seen by the cylinder is consistent with a 26-GPa adiabat pressure.

2. List of Cylinder JWLs

We move to the data used to compile the preceeding comments. The velocities at volumes of 2.2, 4.1, and 6.5 in Tables 5-1 and 5-2 are the ones used in deriving the JWLs. Table 5-3 lists the cylinder-derived JWLs, using PETN as the standard material. The detonation pressures are those obtained from the cylinder fit; hence, LX-17 has the low 26-GPa value. The E_0 values are those from the cylinder fit with the calorimetric values as a bias where appropriate. Many significant digits are included, not because these EOSs are accurate but to avoid round-off errors. It is easy to have significant differences between a pressure calculated using A, B, and C as opposed to A, B, and E_0 unless many digits are included. Any recalculation of the data produces slightly different velocities, and the JWLs are hypersensitive to small changes.

We note a definite difference in full and half-wall PBX-9404 data. In comparing half-wall streak camera data, we find these results:

	Percent velocity-squared compared with PETN	
Relative volume	Half-wall Three runs	Full-wall Four runs
2.2	8.6	3.2
4.1	6.9	2.7
6.5	4.5	3.4

(3)

The full-wall runs are cylinder nos. 175 to 273 from years ago. The half-wall runs are nos. 512 and 528 of recent times. Both have an average density of 1.84 g/cc. There is no known composition difference, so that we may be seeing the changes in the cylinder measurements over twenty years.

3. Comparison of JWLs

We shall consider two measures of energy delivery. One is the "% of energy out"at v = 2.2, k_2. This is the percent of the total detonation energy to have come out into the cylinder wall at this volume. At steady state, a cylinder volume of explosive, $\pi R^2 h$, with R the inner radius and h the length, pushes the wall of mass, $m = \rho_m \pi[(R + W)^2 - R^2]h$, where ρ_m is the metal density and W is the wall thickness. Then, we have

$$k_2 = 100 m u_2^2 / 2E_o, \tag{4}$$

where u_2 is the velocity at v = 2.2. Enough ringing of the shock wave has taken place in the metal wall that u_2 is taken to be the rigid-body velocity. Then, the quantity k_2 is a measure of the steepness of the adiabat. For "fast" explosives, it should be as large as possible. Another measure of this quantity is the pressure-to-energy ratio,

$$P_j/E_o. \tag{5}$$

Fig. 5-1 shows a plot of k_2 as a function of P_j/E_o, and the proportionality is clearly there. LX-14 is a good example of a fast explosive. Two points are given for LX-17, one for P_j = 26 GPa, and the other for 32 GPa. The 26-GPa point lies on the central line, showing that the Cylinder Test delivers the lower detonation pressure.

We next consider the fraction of kinetic energy in the initial shock in the cylinder wall. Previously, we took data so late that the entire wall was in motion like a rigid body. The measured unconfined wall velocity, u_p, may then be considered representative of the entire wall. This is not so for the jump-off. In a plate DYNA2-D run, we find that the confined wall velocity is nearly constant over the first 2/3 of the plate thickness. The unconfined wall velocity (twice as great) appears in the last 1/3 of the plate. At the 2/3rds boundary inside the plate, the velocity jumps to the confined value, briefly lingers, and then hops up to the unconfined value. As an average across the wall, we take:

$$u(\text{average}) \sim 2u_p/3. \tag{6}$$

The % kinetic energy in the shock wave is then

$$k(\text{jump-off}) = 100 m u(\text{average})^2 / 2E_o. \tag{7}$$

The results for Tables 5-1 and 5-2 are

$$k(\text{jump-off}) = 6.3 \pm 2.7\% \tag{8}$$

and

$$k(\text{jump-off}) = 5.4 \pm 3.0\%. \tag{9}$$

The idea that speedy explosives expend more of their energy by v = 2.2 suggests that k(jump-off) should also vary according to the speed of the explosive. However, the data, mostly taken with the streak camera, show no such trend. The importance of the approximate 6% number is that it represents the initial shock wave with no further pushing—to be found in an explosion with no confinement.

We next want to consider the relative efficiency in converting detonation energy to wall kinetic energy. If u_2 is the wall velocity at v = 2.2, then the efficiency, e_2, is

$$e_2 = 100mu_2^2 / 2E_d(v = 2.2). \tag{10}$$

The velocity that should be used is the Fabry velocity. Most of our data are from the streak camera. Using Eq. (11) from Chapter 4 , we correct the streak velocities by 0.98 (assuming a 7° Fabry angle). For the diverse full-wall cylinder explosives of Table 5-2, we find

$$e_2 = 72.1 \pm 1.1\%. \tag{11}$$

The efficiency is the same regardless of the explosive speed and shows the high pushing efficiency of the Cylinder Test. The full-wall cylinders give a comparable efficiency of about 60.5%. The value is lower because the containment is less.

Eq. (11) is directly applicable to the second major assumption of the LLNL Cylinder EOS:

$$E_d / u^2 = \text{constant, for all explosives.} \tag{12}$$

It is not obvious that the total detonation energy would partition itself into the same fractions of kinetic and thermal energy for every explosive. Yet the efficiencies of Table 5-2 say that this is true within a few % within the cylinder, where the confinement causes the product to interact with the walls over a long time.

The variability of the derived JWL detonation volumes, v_j, is another puzzle. These values all cluster about 0.74, but a constant volume will not fit all JWLs. Consider a force, F, compressing a spring:

$$F = PA = k\Delta x, \tag{13}$$

where P is the pressure, A the area, k the spring constant, and Δx the displacement. In one dimension, $\Delta x = 1 - v$ (for a unit area and initial volume), so that

$$P_j = k(1 - v_j). \tag{14}$$

From Chapter 2, we recall that

$$P_j = \rho_o D^2(1 - v_j), \tag{15}$$

and

$$k = \rho_o D^2. \tag{16}$$

In physical terms, $\rho_o D^2$ is the spring constant for compression of the explosive.

In Fig. 5-2, we plot the detonation volume, v_j, as a function of the pressure/energy, P_j / E_o. We find that the low energy-pushing explosives compress to a smaller volume, because there is a less energetic product gas pushing back on the compression. Fast explosives, with large P_j/E_o ratios, have larger detonation volumes.

4. Describing Cylinder Relative Volumes

It may be possible to elicit more information from the Cylinder Test. This test is useful because the relative volume of the product gases, v, is close the geometric volume, v_g, obtained from the radius of the expanding cylinder. Because the wall moves outward, a difference exists, and a correction must be made.

We are interested in checking how close the hydrocodes predict the geometric volumes. For this reason, the cylinder model was run with DYNA2D using various conditions. A contour plot for relative volume was obtained at some given time, as shown in Fig. 5-3 for PETN. There are three ways to obtain geometric volumes. One can then integrate along a path to obtain the average relative volume, given by

$$v_a = \frac{1}{A} \sum_i A_i v_i, \tag{17}$$

where the ith volume and ith area are included. The volume corresponding to the 1-D problem is the Fabry path A'AE. We note in Fig. 5-3 that the path AE

moves into a region of gas with a smaller relative volume. This is why we require the hydrocode to make the volume adjustment.

The results are shown in Fig. 5-4 for the average volumes. The ratio of the average volume to the geometric volume for the Fabry path is:

$$\varepsilon = v_a / v_g = 1.01\,[\,1 - \exp(-1.8 v_g)] + 0.003 v_g. \qquad (18)$$

The same equation may describe the ratio for the streak camera path A'AC, but this path is not a 1-D problem path. Both the Fabry and streak volume ratios are shown in Fig. 5-4, and they are both fit by Eq. (18).

The relative volume next to the wall at point E, v_w, shows more scatter as a result of the different types of code settings, and the value is larger. We may describe the results by

$$v_w / v_g \sim 1.11\,[\,1 - \exp(-1.6 v_g)]\,. \qquad (19)$$

5. One-Dimensional Cylinder Analysis

We can use DYNA2D to consider the behavior of the parts of the copper wall during the 1.763-g/cc PETN cylinder shot, and the results are shown in Fig. 5-5. The spall pressure has been set to a large number to accentuate the oscillations. The unconfined outer face is out of phase with the inner face by the time necessary for the shock wave to cross the copper wall. Reverberating shock waves in the wall cause the oscillations of the inner and outer faces, whereas the center of the wall motion is relatively smooth. We note that the oscillations appear every half-cycle for the center of the wall and every full cycle for the outer face. The center-of-the-wall motion is smoother than that of the outer face.

We also note that the center-of-the-wall velocity is always larger than the average outer velocity. This difference is accounted for by the thinning of the wall with the inner wall advancing into the space previously occupied by the metal.

We now move to the 1-D cylinder wall problem, in which the wall is accelerated from its center of mass, which is taken to be the center of the wall shown in Fig. 5-5. Within the 1-D approach to this problem, we may write the force on the wall as

$$P_f A = ma, \qquad (20)$$

where P_f is the pressure on the wall along the Fabry path, A is the area of push, m is the mass of the wall, and a is the acceleration. The area is $2\pi(R - W/2)dh$, where R is the outer radius, W the wall thickness, and dh an arbitrary

distance along the cylinder. The mass being pushed is $\pi\rho_m[R^2 - (R - W)^2]dh$, where r_m is the density of the copper cylinder. These are combined to give

$$P_f = \rho_m \frac{[R^2 - (R - W)^2]}{2(R - W/2)} a, \tag{21}$$

where, from Eq. (2), Chapter 4, the thinning wall is given by

$$W = \{R_o / R\} W_o. \tag{22}$$

The initial outer radius is R_0, and the wall thickness is W_0. Finally, we need to obtain a relative volume. We modify the geometric volume, v_g, from Eq. (3) from Chapter 4 , to produce an average volume, v_a:

$$v_a = \varepsilon v_g = \varepsilon\{[S_o + (R - R_o) + (W_o - W)] / S_o\}^2, \tag{23}$$

Now, S_0 is the initial inner radius $(R_0 - W_0)$, so that

$$v_a = \varepsilon [(R - W) / (R_o - W_o)]^2. \tag{24}$$

All this can be followed in a simple model. The difficult part is getting a good fit for the acceleration. From Fig. 5-5, we note that the velocity peaks of the unconfined face are equivalent to the velocity of the center of mass. Also, the zero-time of the center of mass occurs slightly before this. By taking data beyond 3 to 4 scaled μs, i.e., beyond the ringing, we obtain accelerations that should be close to those of the center of mass—adding the extra time at the start will not matter in the differentiation from velocity to acceleration as we process the Fabry data.

The first data tried were raw streak-camera data for the outer copper face, with several hundred pairs of $R - R_0$ vs time points. The four sets of data points (two cameras on two sides) were averaged to give the overall curve. This curve was smoothed, then fit with a polynomial to the sixth power. The acceleration was obtained by double differentiation of the fitted function. The results for 1.763 g/cc PETN are shown in Fig. 5-6. The data for shot no. 511, a half-wall cylinder, maintain their fit out to v ~ 10. The older, full-wall no. 209 shows the common problem of trying to fit noisy streak camera data. The fit deviates at low volumes, and the pressure becomes unphysical. This noisiness does not affect the creation of a JWL because this is not really a fit of all the data. Also shown for comparison are the adiabats derived from the JWL and from CHEQ. Agreement is good, although both the data and CHEQ suggest that the adiabat could lie slightly below the JWL values.

Consideration of the more accurate Fabry data remains for the future. One approach is to average the two velocity vs time curves, and then fit the region from 4 μs onto a polynomial:

$$u_f - u_o = F + G(t - t_o) + H(t - t_o)^2 + I(t - t_o)^3 + J(t - t_o)^4, \qquad (25)$$

where t_o is about 4 μs, u_o is the velocity at this time, and F, G, H, I, and J are constants. The acceleration is obtained by differentiating Eq. (25). Perhaps a more accurate function can be found.

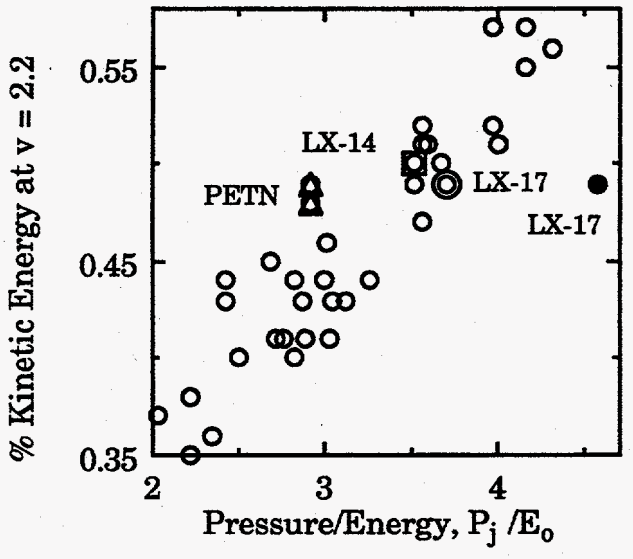

Fig. 5-1. Fraction of total detonation energy appearing as kinetic energy at v = 2.2 as a function of the ratio of P_j / E_o for full-wall cylinder shots. Special explosives are 1.763 g/cc PETN (triangles); LX-14 (squares); LX-17 with a 26 GPa detonation pressure (open circles); and LX-17 at 32 GPa (closed circles). The higher value for LX-17 does not fit the pattern, which may be taken as evidence that 26 GPa is the actual LX-17 adiabat pressure.

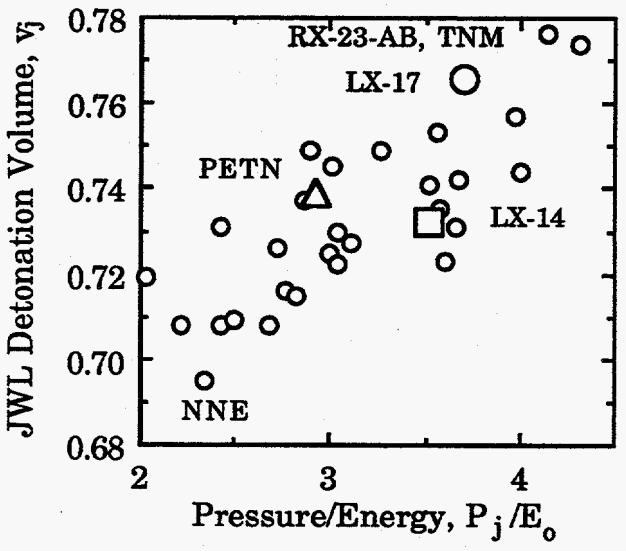

Fig. 5-2. JWL detonation volume, v_j, as a function of P_j / E_0 for full-wall cylinder shots. "Slower" explosives compress to smaller volumes. Special points are 1.763 g/cc PETN (triangles); LX-14 (squares); and LX-17 with a 26 GPa detonation pressure (circles). The explosive acronyms are explained in the Appendix.

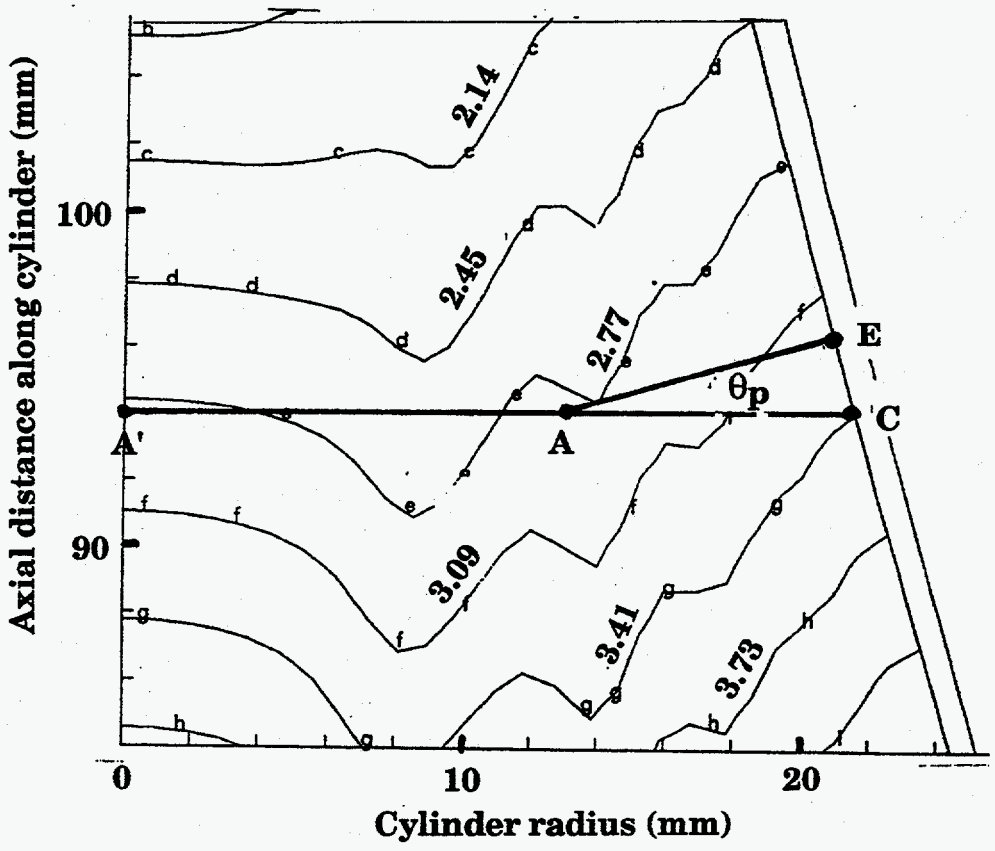

Fig. 5-3. Relative volume contours in a 1.763 g/cc PETN cylinder as calculated by DYNA2D. The letters are the same points used in the Fabry/streak camera model shown in Figure 3-1. The path for calculating the average streak volume is A'AC; for the Fabry, it is A'AE. As we move to the cylinder wall, the relative volume of the gas increases because of cylinder expansion.

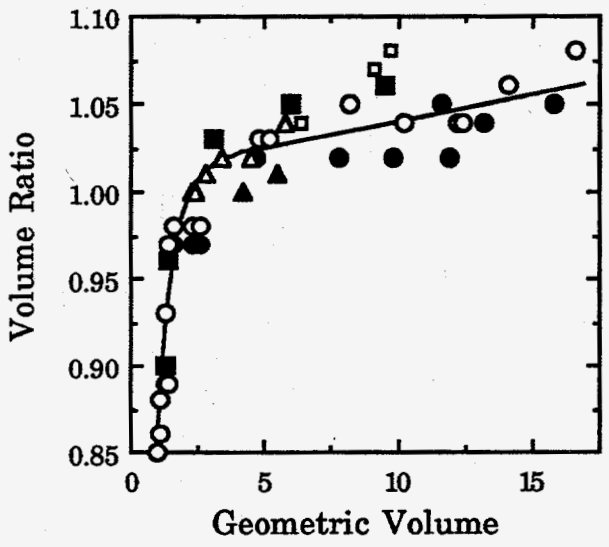

Fig. 5-4. Ratio of average relative volume to the geometric relative volume, ε, as a function of geometric volume, v_g (as calculated from the hydrocode). The streak and Fabry cases fit the same curve although the volumes are defined differently and the points are offset. The open symbols are for the streak camera data; the closed symbols are for the Fabry data. A mixture of programmed and beta burn, with and without a slide-line, was run. The cases run are PETN, full-wall (circles) and half-wall (triangles), and nitromethane full-wall (squares).

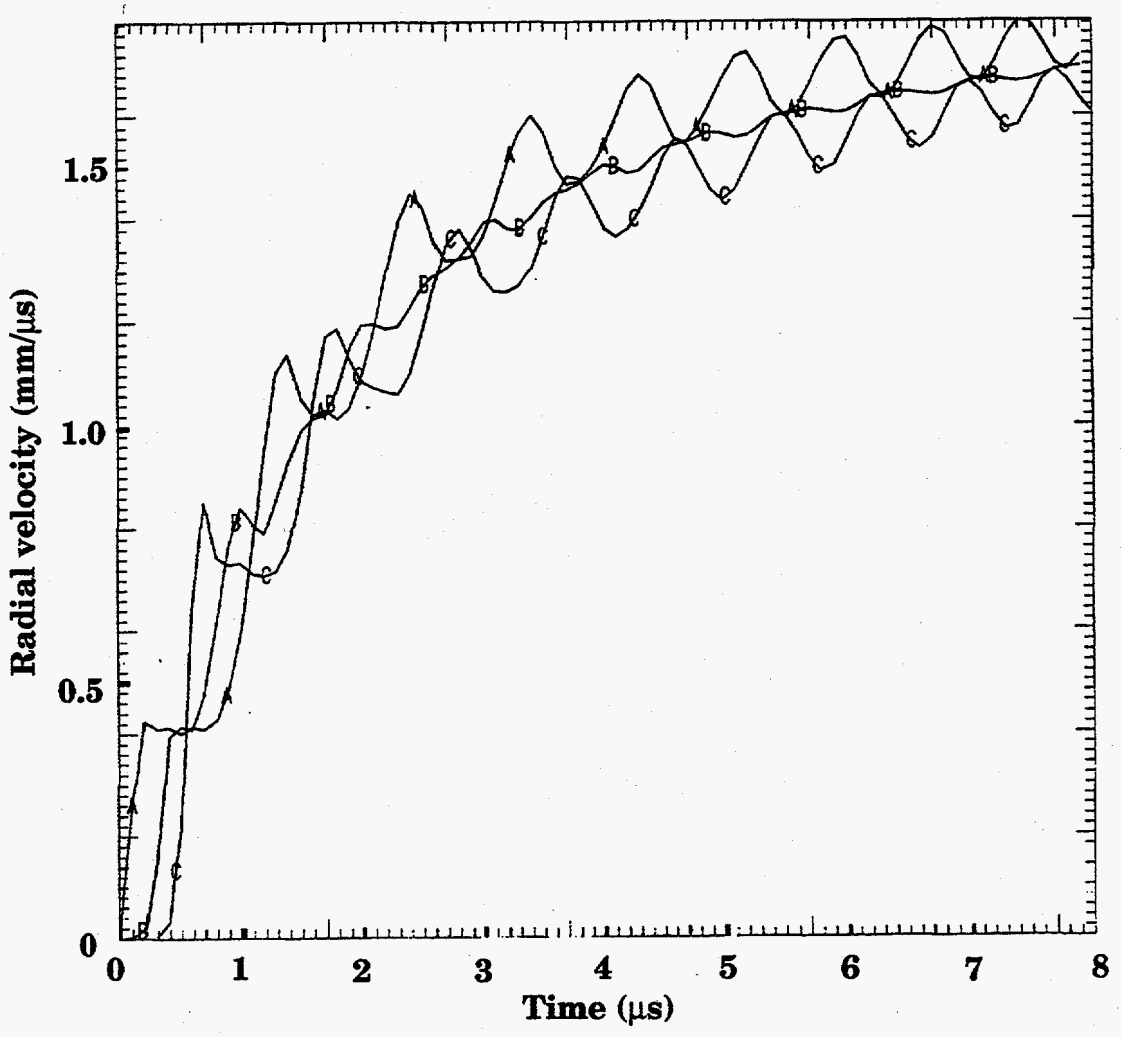

Fig. 5-5. Calculation of the velocity at three places in a copper wall of as cylinder driven by PETN of 1.763 g/cc. The curves are from top to bottom the inner (confined) wall (A), the center of motion of the wall (B), and the outer (unconfined)wall (C). All code burns and mergings give the same result. Reverberating shock waves in the wall cause the inner and outer faces to be out of phase throughout, whereas the center of mass motion is relatively smooth. Experimentally, only the velocity of the outer face is measured.

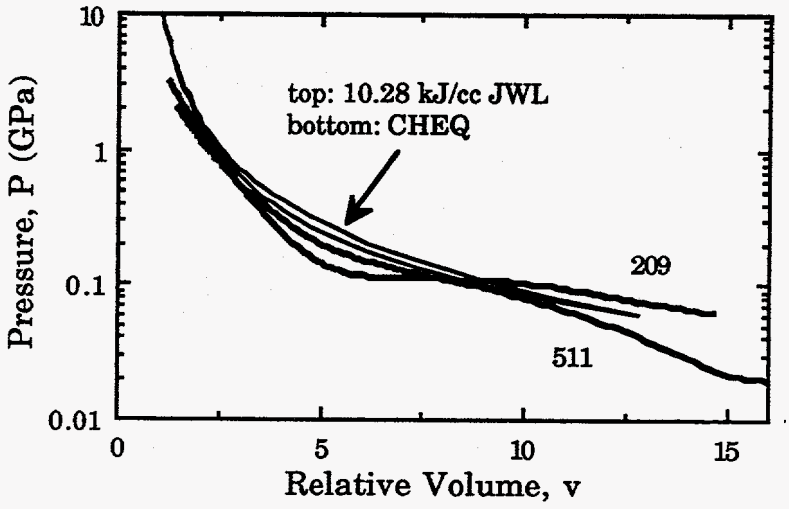

Fig. 5-6. Direct calculation of the adiabat pressure from streak camera data for PETN. The fit for shot no. 511 looks good to v ~ 10 but the older shot no. 209 is too noisy and the fit deviates at low volumes.

Table 5.1. Basic copper cylinder data, including velocities, for five often-measured explosives, as determined by streak camera (S) and Fabry (F). In a different column, F is full-wall, and H is half-wall.

Explosive	Shot No.			Inner radius (mm)	Wall thickness (mm)	Expl density (g/cc)	Det velocity (mm/μs)	Jump-velocity (mm/μs)	Wall velocity (mm/μs) at 25-4 mm diameter for R – R_0 equal to 6.0	12.5	19.0	% energy out Jump-off	At v=2.2
LX-14	353	S	F	12.709	2.606		8.86	1.15	1.59	1.73	1.79	11.5	50
	521	S	H	25.410	2.719	1.831	8.80	1.15	2.145	2.335	2.395	5.8	45
	520	S	H	25.408	2.727	1.831	8.80	1.40	2.135	2.325	2.395	8.6	45
	510	S	H	25.412	2.722	1.821	8.78	1.05	2.130	2.320	2.405	4.8	45
	469	S	H	12.712	1.359	1.821	8.77	1.10	2.095	2.325	2.380	5.3	43
	520	F	H	25.408	2.727	1.831	8.80	0.94	1.895			3.9	36
	521	F	H	25.410	2.719	1.831	8.80	0.97				4.1	
PBX-9404	237	S	F	12.714	2.595	1.845	8.77	1.00	1.610	1.735	1.810	8.8	52
	293	S	F	12.712	2.595	1.842	8.76	0.95	1.600	1.740	1.800	8.0	51
	235	S	F	12.715	2.593	1.844	8.76	0.91	1.600	1.765	1.825	7.3	51
	273	S	F	12.714	2.595	1.843	8.76	1.30	1.590	1.730	1.785	14.9	50
	512	S	H	25.418	2.718	1.849	8.78	0.80	2.180	2.350	2.430	2.8	47
	528	S	H	25.413	2.724	1.835	8.77	0.99	2.160	2.330	2.415	4.3	47
	175	S	H	25.414	2.602	1.841		1.00	2.195	2.390	2.455	4.2	46
PETN	209	S	F	12.714	2.595	1.765	8.28	0.90	1.58	1.73	1.77	7.0	49
	187	S	F	12.714	2.593	1.765		0.81	1.57	1.71	1.78	5.7	48
	511	F	H	12.718	1.361	1.761	8.27	0.86	2.10			3.2	43
	511	S	H	12.718	1.361	1.761	8.27	1.00	2.09	2.28	2.38	4.3	43
RX-26-AF	460	S	H	25.413	2.720	1.844	8.24	1.05	1.955	2.120	2.160	5.5	43
	495	S	H	25.414	2.719	1.845	8.25	1.11	1.945	2.100	2.165	6.2	43
	484	S	H	25.408	2.718	1.845	8.24	1.00	1.945	2.095	2.190	5.0	43
	455	S	H	12.709	1.362	1.846	8.24	1.10	1.940	2.085	2.155	6.1	43
	490	S	H	25.415	2.722	1.844	8.24	1.00	1.940	2.095	2.160	5.0	43
	444	S	H	25.413	2.718	1.840	8.23	1.00	1.940	2.095	2.170	5.0	43

Table 5-1, part 2

Explosive	Shot No.			Inner radius (mm)	Wall thickness (mm)	Expl density (g/cc)	Det velocity (mm/μs)	Jump-off velocity (mm/μs)	Wall velocity (mm/μs) at 25.4-mm diameter for $R-R_o$ equal to			% energy out	
									6.0	12.5	19.0	Jump-off	At v=2.2
LX-17	349	S	F	25.414	5.210	1.900	7.63	1.02	1.293	1.409	1.453	13.5	49
	434	S	F	25.420	5.184	1.875	7.55	0.74	1.29	1.41	1.46	7.0	49
	523	S	H	25.417	2.722	1.917	7.66	1.05	1.754	1.884	1.953	7.2	45
	470	S	H	25.417	2.718	1.904	7.63	0.80	1.750	1.856	1.933	4.1	45
	439	S	H	25.412	2.714	1.912	7.65	0.90	1.74	1.89	1.95	5.2	44
	522	S	H	25.414	2.723	1.908	7.64	1.05	1.741	1.880		7.2	44
	471	S	H	25.407	2.724	1.906	7.63	0.85	1.724	1.861	1.930	4.7	43
	523	F	H	25.417	2.722	1.917	7.66	1.02	1.70			6.8	42
	522	F	H	25.414	2.723	1.908	7.64	0.81	1.69			4.3	42

Table 5-2. Summary of experimental streak-camera, copper-cylinder wall velocity data for homogeneous explosives in full-wall copper cylinders.

Explosive	Cylinder shot no.	Initial density (g/cc)	Inner radius (mm)	Wall thick (mm)	Jump-off vel. (mm/μs)	Wall velocity (mm/μs) at 25.4 mm diameter for $R - R_o$ equal to 6 mm	12.5 mm	19 mm	% energy out Jump-off	At v=2.2	% Efficiency at v=2.2
1,2-DP	115	1.256	12.7	2.6	0.46	1.090	1.235	1.310	2.7	34.7	72.4
BTF	270	1.852	12.718	2.601	1.32	1.605	1.755	1.835	13.8	45.9	72.2
FEFO	513	1.607	12.720	2.586	0.63	1.340	1.490	1.560	4.3	43.8	71.7
FM-1	514	1.509	12.716	2.596	0.55	1.258	1.390	1.455	3.8	44.8	72.2
HMX	106, 107	1.894	12.714	2.596	1.24	1.650	1.820	1.883	12.5	49.7	71.9
HMX	198, 199	1.188	12.716	2.594	0.49	1.173	1.314	1.384	3.3	43.1	72.3
HNB	326	1.965	9.542	1.948		1.700	1.880	1.955		44.0	72.0
HNS	Pantex	1.681	12.7	2.6	0.66	1.255	1.385	1.458	5.3	42.9	72.3
HNS	Pantex	1.655	12.7	2.6	0.59	1.228	1.362	1.433	4.2	40.5	72.2
HNS	Pantex	1.610	12.7	2.6	0.61	1.210	1.335	1.393	4.8	42.8	72.2
HNS	Pantex	1.597	12.7	2.6	0.64	1.229	1.340	1.413	5.2	42.9	72.2
HNS	Pantex	1.504	12.7	2.6	0.57	1.170	1.297	1.368	4.3	40.6	72.4
HNS	Pantex	1.402	12.7	2.6	0.42	1.081	1.207	1.266	2.7	40.6	72.3
HNS	Pantex	1.200	12.7	2.6	0.36	0.959	1.073	1.145	2.5	40.3	72.2
HNS	Pantex	1.001	12.7	2.6	0.41	0.817	0.931	0.981	4.2	37.4	72.3
NM	391	1.13	25.415	5.199	0.35	1.045	1.180	1.230	2.2	44.4	72.1
NNE	324	1.034	25.4	5.1		0.836	0.935	0.990		36.3	70.8
PETN	187, 209	1.765	12.7	2.6	0.86	1.575	1.720	1.775	6.0	46.1	73.4
PETN	262	1.498	12.712	2.596	0.64	1.365	1.533	1.601	4.3	44.1	72.3
PETN	261	1.266	12.711	2.598	0.68	1.162	1.305	1.381	5.7	37.7	71.4
PF	194	1.833	12.7	2.5	0.79	1.395	1.525	1.585	7.3	51.0	70.5
RX-23-AA	402	1.424	25.419	5.198		1.356	1.499	1.541		56.9	76.4
RX-23-AA	244	1.424	12.7	2.5	0.61	1.315	1.452	1.496	5.0	52.3	70.1
RX-23-AB	378	1.356	25.4	5.1		1.088	1.179			57.0	72.0
RX-23-AB	246	1.356	12.7	2.5	0.48	1.075	1.182	1.210	4.9	55.4	70.0

Table 5-2, part 2

Explosive	Cylinder shot no.	Initial density (g/cc)	Inner radius (mm)	Wall thick (mm)	Jump-off vel. (mm/μs)	Wall velocity (mm/μs) at 25.4 mm diameter for $R - R_0$ equal to 6 mm	12.5 mm	19 mm	% energy out Jump-off	At v=2.2	% efficiency at v=2.2
RX-23-AC	245	1.136	25.4	5.1	0.49	1.077	1.175	1.219	4.7	50.9	71.3
TATB	322, 379	1.83	25.408	5.207	0.97	1.300	1.403	1.453	11.6	46.7	72.5
TNGU	413	1.885	12.711	2.598		1.600	1.750	1.825		49.0	72.3
TNM	474	1.650	12.715	2.592	0.48	1.000	1.095	1.130	5.7	55.7	72.1
TNT	140-1, 271	1.632	25.427	5.186	0.57	1.210	1.355	1.410	4.1	41.4	71.7

Table 5-3. JWL coefficients as determined from the Cylinder Test. GPa may be converted to Mbar and kJ/cc to Mbar·cc/cc by multiplying by 0.01. A, B, and C are listed to six significant digits so that round-off errors will not occur in their use. Explosives are listed in order of the PETN standard, often-run explosives, and homogeneous explosives.

Explosive	Initial density ρ_o (g/cc)	Detonation velocity D (mm/μs)	Energy of detonation E_o (kJ/cc)	Det pressure P_j (GPa)	A (GPa)	B (GPa)	C (GPa)	R_1	R_2	ω	γ_j
PETN	**1.763**	**8.274**	**10.8**	**31.5**	**1032.158**	**90.57014**	**3.72735**	**6.000**	**2.60**	**0.57**	**2.832**
PBX-9404	1.843	8.76	10.5	37.5	740.349	11.7009	0.725292	4.317	1.05	0.25	2.771
LX-14	1.830	8.80	10.8	38.0	661.414	5.40066	1.825670	4.118	0.95	0.40	2.729
RX-26-AF	1.844	8.24	9.2	33.7	564.811	4.47297	0.656169	3.998	0.887	0.20	2.715
LX-17	1.905	7.63	7.0	26.0	989.761	17.4413	1.42712	5.15	1.713	0.45	3.274
BTF	1.852	8.49	11.3	34.0	954.6163	22.66797	2.956620	5.027	1.60	0.50	2.926
1,2-DP	1.26	5.97	6.9	13.5	167.6882	3.630269	1.419315	4.118	1.00	0.33	2.326
FEFO	1.607	7.45	8.2	24.5	405.2865	4.158285	1.424809	4.148	0.84	0.40	2.641
FM-1	1.509	6.57	7.1	19.0	267.2952	7.795149	1.712195	4.281	1.23	0.48	2.428
HMX	1.894	9.10	11.0	40.5	858.0805	7.546531	0.781274	4.306	0.80	0.30	2.873
HMX	1.188	6.68	6.4	15.5	218.2000	4.959453	1.977170	4.379	1.10	0.55	2.420
HNB	1.965	9.34	13.2	43.0	1047.883	7.982396	1.396122	4.472	0.85	0.28	2.986
HNS	1.681	7.08	7.4	23.0	369.0609	2.028814	1.455287	4.041	0.75	0.40	2.664
HNS	1.655	7.03	7.5	21.5	423.7580	3.131467	1.704155	4.332	1.00	0.40	2.804
HNS	1.610	6.96	6.9	21.0	371.4426	3.482474	1.041547	4.172	0.90	0.33	2.714
HNS	1.597	6.96	7.1	21.5	328.5734	4.244564	1.529860	4.077	1.20	0.40	2.598
HNS	1.504	6.70	6.8	18.5	310.0104	3.426403	1.670635	4.235	1.10	0.42	2.649
HNS	1.402	6.34	5.8	16.0	226.5460	2.106304	0.783032	3.935	0.72	0.30	2.522
HNS	1.200	5.74	4.6	11.5	136.8456	9.270925	1.991536	4.300	2.50	0.59	2.438
HNS	1.001	5.10	3.6	7.3	138.8149	2.779832	0.694139	4.657	1.00	0.35	2.567
NM	1.13	6.28	5.0	12.0	297.7799	5.954922	1.108004	5.026	1.10	0.49	2.714
NNE	1.034	5.31	3.8	8.9	94.87257	1.140533	0.619964	3.706	0.75	0.30	2.276
PETN	1.503	7.48	8.5	24.0	351.0723	5.705547	1.216240	4.075	0.90	0.35	2.504
PETN	1.263	6.59	7.2	16.0	228.1744	5.104579	1.412013	4.240	1.05	0.35	2.428
PF	1.833	7.29	7.5	27.0	418.3832	5.083194	1.753291	4.110	0.95	0.65	2.608

Table 5-3, part 2

Explosive	Initial density ρ_o (g/cc)	Detonation velocity D (mm/μs)	Energy of detonation E_o (kJ/cc)	Det pressure P_j (GPa)	A (GPa)	B (GPa)	C (GPa)	R_1	R_2	ω	γ_j
RX-23-AA	1.424	8.64	6.5	25.8	737.8071	5.34171	0.167361	4.610	0.73	0.35	3.120
RX-23-AB	1.356	7.48	4.1	17.0	809.7106	6.543083	0.097540	5.243	1.00	0.30	3.463
RX-23-AC	1.136	7.88	4.5	18.0	379.9134	1.772972	0.938430	4.296	0.76	0.60	2.919
TATB	1.83	7.58	7.3	26.0	686.8140	7.811448	0.877917	4.598	1.20	0.30	3.044
TNGU	1.885	8.71	10.5	37.0	792.6978	7.784202	2.005135	4.410	1.00	0.49	2.865
TNM	1.65	6.45	3.6	15.5	642.2267	3.898275	0.258200	5.020	0.90	0.52	3.429
TNT	1.632	7.07	7.1	20.5	524.4089	4.900052	0.626131	4.579	0.85	0.23	2.979

Note: PF and TNGU have detonation velocities calculated from TIGER.

Chapter 6. One-Dimensional Plate Data

1. The Jump-Off Velocity of Metal Plates

The cylinder came first; oddly, the conceptually simpler, 1-D plate shots came later with the development of the "electric gun." The "gun" comes in 25-mm (1-in.) and 51-mm (2-in.) diameter sizes, and we shall describe the former. Electric current from a capacitor runs through copper leads to a 0.05-mm (2-mil) thick aluminum foil, which is vaporized. This drives a 0.13-mm (5-mil) thick mylar (density = 1.4 g/cc) flyer with a 25-mm diameter. The flyer passes through a Lucite "barrel," which is really a 5.6-mm-thick disc, with a 75-mm outer diameter and a 25-mm inner diameter. The sample of explosive sits inside a second Lucite barrel of the same dimensions. Glued to the explosive surface is the metal plate, whose unconfined face will be measured. The mylar flyer initiates the explosive. All samples reported here were made by Don Breithaupt.

The metal plate is glued onto the explosive using Eastman 910 epoxy, Shell 815, or a high-viscosity, high-grade silicone vacuum grease. These substances are put on and then wiped off to form a thin film. Chet Lee reports that the grease sticks better to LiF crystals than to metal foils. Because the glue interface is important in the modeling of thin plates, we reviewed the shot folders for glue thickness data. In some cases, the explosive and foil were measured by micrometer before and after gluing. The average of 45 samples was found to be:

$$\begin{aligned} \text{glue thickness} &= 0.022 \pm 0.019 \text{ mm} \\ &= 0.86 \pm 0.74 \text{ mil.} \end{aligned} \qquad (1)$$

There were six cases in which the procedure had been repeated five times for each sample. The average standard deviation, considering each set separately, was ±0.025 mm, showing that the standard deviation in Eq. (1) is the error of measurement. Epoxy was mentioned as the major glue. Only one case of the grease was documented, in which the layer was measured at 1.8 mil.

The flyer has been calibrated by silvering its front surface and then driving it into a plate of glass. The velocity is calibrated as a function of the capacitor bank voltage. For a 25-mm-diameter, 10-mil mylar flyer (at 20, 30, and 40 kV), the calibrated velocities are 4.0, 4.7, and 5.3 mm/μs, respectively. The 51-mm, 10-mil flyer at the same voltages produces 2.1, 3.6, and 4.3 mm/μs.

The velocity is measured with a Fabry-Perot interferometer. The beam is about 5 to 10 mm wide but is focused to a small point on the surface of the plate. A 12.5-mm focal lens is used to watch the motion over a definite region. Use of the narrow Fabry beam has led to concern as to whether the measure-ment is

sampling too small a region on the surface, especially for explosives with large grain sizes like LX-14. Chet Lee says that the small point of focused laser light is always larger than several hundred microns and that a width of 1 mm is a better number.

For straight-on metal plate shots, the jump-off velocity at the instant of impact is a critical parameter. The measured particle velocity on the free surface (outer face) of the metal, u_{fs}, often has this simple relation with the unmeasured jump-off velocity on the confined, inner face, u_m:[1]

$$u_m \simeq u_{fs}/2. \tag{2}$$

This relation occurs because the shock wave crossing the plate creates a rarefaction wave that moves backwards at the same velocity when it hits the unconfined wall. Thus, the forward wall velocity is the sum of the two equal velocities. Walsh and Christian calculated that the ratio of the backward to forward wave velocities should be 1 at the limit of zero shock and could rise slightly above 1 at high pressures.[1] Eq. (2) requires that the shock wave move through the metal without decay. Thus, a long initial pressure pulse is needed. Then, the rarefaction wave in the product gas decouples the explosive from the wall and allows the shock wave to continue.

A consideration of the pressures generated in a metal plate hit straight on by an explosive led to the "impedance matching" equation[2,3]

$$P_m = P_p + \rho_r U_r (u_p - u_m), \tag{3}$$

where P_m is the pressure at the confined, inner metal face at the instant of impact; P_p is the detonation pressure of the explosive; ρ_r is the density of the gaseous detonation products at the detonation point; ρ_0 is the initial density of the explosive, U_r is the shock velocity in the detonation products; and u_p and u_m are the jump-off particle velocities of the explosive and the metal. Eq. (3) holds only at the instant of initial impact, and it is an inspired assumption—not one that can be derived by first principles. In Eq. (3), we may consider the second term on the right as putting extra pressure into the metal as the result of the back-reflected rarefaction wave. Deal next made the Acoustic Approximation

$$\rho_r U_r \simeq (4/3\rho_o)(3/4D) = \rho_o D, \tag{4}$$

where ρ_o is the initial explosive density and D is the explosive's detonation velocity. By using the mass/momentum conservation relations,

$$P_p = \rho_o D u_p, \tag{5}$$

and

$$P_m = \rho_m U_m u_m, \tag{6}$$

where ρ_m is the initial density of the metal and U_s is the shock wave velocity on the inner face of the metal plate. This is related to the particle velocity by

$$U_m = C_o + S_1 u_m. \tag{7}$$

For Al, OHFC Cu, and Ta, the densities are 2.703, 8.93, and 16.69 g/cc. The constants C_o and S_1 are 5.24 and 1.40; 3.94 and 1.489; and 3.41 and 1.2 mm/μs, respectively, and are in dimensionless units.[4]

The jump-off velocities are those first measured as the initial step at time zero. This velocity declines rapidly with increasing metal-plate thickness until the plate becomes thicker than the reaction zone width of the explosive. At this point, the velocities decrease slowly as the metal thickness increases.[2] The velocities usually considered are those in the nearly constant range where the plate thickness has just exceeded the reaction zone width. If the plate thickness equals the reaction zone width for a near-ideal explosive, $P_a \sim P_p$, where P_a is the adiabat pressure of the explosive defined in Chapter 1. (We recall that the adiabat point is the point where the explosive, in large-size and at steady state, leaves the Rayleigh Line and starts down the Principal Adiabat.) Using the equations above, we obtain

$$P_a \sim P_p = (\rho_m U_m + \rho_o D)\, u_{fs}/4. \tag{8}$$

This equation is the usual means of experimentally obtaining the detonation pressure. Shvedov's detailed review of two solid explosive suggests that the adiabat pressures are good to perhaps ±10 to 15%.[5]

2. Experimental Plate Jump-Off Results

Table 6-1 lists the jump-off velocities for plate shots of aluminum, copper, and tantalum. The data were all taken with Fabry-Perot interferometry, and the precision in a given shot between fringes was about ±0.01 to 0.02 mm/μs, far better than the spread of results for a given explosive. The detonation velocities were adjusted from cylinder data using the 2/3 power-density relation listed in the previous chapter. This adjustment holds for both PETN and HNS samples.

The PETN has been divided into two parts. The samples of 1.71 to 1.73 g/cc are considered to be normal PETN, and their detonation pressures averaged to 32 ± 4 GPa. The PETN of 1.76 to 1.78 g/cc is marked with a double asterisk and is not used in calculating the official PETN detonation pressure.

These samples, according to C. Tarver and J. Kury, were so compressed that they became partly transparent. They believe that a shock wave then passed through this material with the detonation wave catching up later. Because the PETN was precompressed, the apparent detonation pressure would be too high. The pressure for these four samples was 38 ±2 GPa. This phenomenon would appear only in thin slabs of explosive and would not be a factor in the Cylinder Test.

Some of the LX-17 plate shots had 3-mm LX-10 booster pads to bring 20-mm-thick LX-17 to steady state.

If we ignore the highly scattered TNT data in Table 6-1 and average all data where the plate thickness is greater than the reaction zone, we find that the plate detonation pressures for LX-14, PBX-9404, and PETN are in agreement with the cylinder JWL and jump-off pressures. The exception is LX-17, where the 34 GPa found from plates is considerably higher than the 26 GPa value found previously from the cylinder JWL. It does agree, however, with the less certain cylinder jump-off pressure.

Fig. 6-1 shows the LX-14 data as a function of plate thickness. The 44-GPa LX-14 point is deep inside the 0.1-mm-thick reaction zone and surely represents the spike. The pressures near the 0.1-mm zone edge are spread around 36 GPa, in agreement with pressures measured by other means. The plate thickness data for LX-17 is not in agreement and will be considered in the next chapter.

Finally, both J. Kury and D. Steinberg have mentioned that the large grain size of LX-14 has made its results harder to interpret than that of the fine-grained LX-17 (see the Appendix for grain sizes). We would expect the biggest problem with the hundred-micron particles of LX-14. The standard deviations for the jump-off velocity, starting with the largest deviation, is given in the following table.

Explosive	Plate material	Plate thick-ness (mm)	Average jump-off velocity (mm/μs)	% Std. dev.
TNT	Cu	0.025 to 0.05	1.91	13
PETN	Ta	0.10	1.59	11
LX-14	Cu	2.5	2.07	6
LX-14	Cu	0.26 to 0.53	2.18	5
LX-14	Ta	0.25 to 0.77	1.61	5
PETN	Ta	0.25	1.41	4
LX-17	Ta	0.10 to 2.5	1.61	4
LX-17	Ta	0.25	1.63	3
PBX-9404	Ta	0.25 to 0.51	1.73	2

(9)

The detonation pressures taken from the plates are summarized in Eq. (5) of Chapter 7.

3. Establishing a Plate Test

With cylinder tests at $30,000 each, a plate shot at 1/10th the cost is an acceptable way to get a quick JWL. It is not a true "test" because we do not obtain a geometric relative volume. The JWL must be obtained by trial and error in the 1-D hydrocode, with the likelihood of a wide variation in the possible results.

We would like to have a plate geometry with as high a kinetic energy transfer efficiency as possible. For the cylinder, the greater the degree of confinement the more detonation energy is transferred to wall kinetic energy. Hence, a full-wall cylinder is more efficient than a half-wall, and tantalum is more efficient than copper. The opposite is true for the plate, because any forward resistance simply causes the gas to blow backward. We expect higher efficiency in thin plates of light metals.

Let h_f, h_o, and h_m be the thicknesses of the flyer, explosive, and metal plate. The densities and velocities of the flyer and metal are ρ_f, u_f, ρ_m, and u_m. At a long enough time, the unconfined face metal velocity may be taken as an average velocity for the entire plate. The total detonation energy of the explosive in kJ/cc is E_o. The percent of total energy appearing as kinetic energy of the plate, k, is

$$k = 100*(\rho_m h_m u_m^2 - \rho_f h_f u_f^2) / 2h_o E_o. \qquad (10)$$

We need to pick a special time for comparing measurements. Kinetic energies for all three plate materials are listed in Table 6-2. The points being compared are the velocities at the scaled times of 0.5 and 1.0 μs for a 10-mm-thick explosive. The scaled time for a sample of thickness h_o (in mm) is

$$t_o(\mu s) = (h_o/10)t_{10}, \qquad (11)$$

where t_{10} is the time for the 10-mm explosive. Also shown is the thickness ratio of explosive to plate, h_o/h_m, in dimensionless units. For a family of metals with a constant thickness ratio, we may look for the same fraction, f, at the scaled time, t_o. We see that, for a given metal, k increases as the ratio increases, peaks somewhere between 20 and 50, and then decreases. Too much or too little explosive is inefficient as gas shoots out the back and sides.

The kinetic energy fraction data in Table 6-2 have a lot of scatter. Also complicating the results are the 3-mm LX-10 drivers used in the 51-mm-diameter phm86000-series LX-17 shots. We compare six families with the same metal at the two scaled times with thickness ratios of 20 to 50. In general, we see that for efficiency LX-14 ≥ LX-17 >> PETN. For LX-14, the metal efficiencies are Cu ≥ Ta >> Al. On the basis of this limited data, mainly LX-14 data, the highest efficiency

is obtained with copper using a thickness ratio of 20 to 40. Tantalum showed the same efficiency at a ratio of 40 and would be close in performance. Selecting 40 leads us to the often-used combina-tion of 10-mm explosive and 10-mil metal (or 20-mm explosive and 20-mil metal).

We consider a "standard" plate shot to be fired before the blitz of dimension-changing begins. Chet Lee mentions that the laser light reflects better off shocked tantalum than off copper. Such a standard shot should be 20-mil tantalum with 20-mm explosive (or 10 and 10). The 20-mm is selected to allow for expected steady state in nonideal explosives such as LX-17. The Fabry would be run at least for 1.5 scaled μs, i.e., 3 μs for 20 mm. To avoid edge effects, we would run the 10-mm explosive with a 1-in. diameter and the 20 mm with a 2-in. diameter. Such a collection would allow easy comparison between plate shots of different explosives, much as we do now with cylinders.

John Kury has noted that we should be able to define geometric volumes for the plates. We integrate the Fabry velocity over the time of the shot to obtain the $R - R_0$ distance, Δh. The relative volume of the cylinder swept out by the explosive is then

$$v \sim (h_0 + \Delta h) / h_0. \qquad (12)$$

This would be true for the center of the plate, which is where we measure, until the side effects work their way in. Assuming shock velocities of 5.5 mm/μs in Cu or Ta, we calculate a 2.3-μs, 1-D time for a 25-mm-diameter gun shot and 4.6 μm for 51-mm shot. We now examine the longest running plate shots to see the results. The data are listed below:

	No.	Exp. length (mm)	Last time (μs)	Inte-gral (mm)	Max. vol. v	Rel. slope	Plate thick (mm)
PETN	ppe87003	5	0.9	3.3	1.7	0.09	0.10
LX-17	pta90005	5	1.5	3.5	1.7	0.11	0.25
PETN	ppe87005	5	1.5	3.6	1.7	0.07	0.25
LX-14	phm85013*	10	2.4	8.0	1.8	0.03	0.51
LX-14	phm90003	5	1.7	4.5	1.9	0.13	0.25

(13)

None of the plates was measured for long, and none reached the time for the side effects, even at 25 mm. The first problem we see is that the integral to $R - R_0$ is not large. We did not reach even $v = 2$, and this is partly due to the inefficiency of the linear geometry, changing as the first power in distance. The second problem is that the velocity saturates quickly—which occurs because most of the explosive blows away from the back and edges and the efficiency of putting energy into the forward direction is not high. The slope listed above is the increase

(compared to the total height) seen at the end per μs. All plates were made of Ta except for Cu in the asterisk case.

It appears then, that we could work to obtain a geometric volume if we used thin explosives of 4 or 5 mm combined with metal plates of 0.1 to 0.25 mm. A goal of about v = 3 seems to be the maximum, and the velocity curve would have leveled off at that point. We also recall that the early v ~ 1 results cannot be used without a hydrocode correction because we know that the explosive is coming from v < 1.

4. The Lucite PETN Experiment

PETN at densities of about 1.763 g/cc was studied in a careful detonation pressure experiment.[6] A 102-mm-diameter baratol plane wave lens was used to drive a PETN sample of either 25 or 50 mm in diameter. The explosive was placed against a stack of five carefully measured Lucite (polymethylmethacrylate) plastic discs. An electrical sensor on the far end picked up signals generated by the Lucite due to the shock electric effect.[7] The signals were placed on a high-speed oscilloscope, and the arrival time of the shock wave at each interface was measured.

The as-measured data for PETN samples of 25-mm (1-in.) and 13-mm (1/2-in.) lengths are listed in Table 6-3. The time for the explosive/disc 1 signal is time-zero by definition. The next times for the measured signals at discs 1/2, 2/3, 3/4, 4/5, and 5/standoff. These times are used to calculate an average shock velocity, U_m, applicable at the mid-point of each disc. Note how the velocities are higher in the center of disc 1. This led the researchers to initially use a quadratic fit of average velocity vs mid-point total distance in order to extrapolate back to time zero. The shock velocity was then converted into a particle velocity within the Lucite. Eq. (8) in the form

$$P_p = (\rho_m U_m + \rho_o D)\, u_m/2. \qquad (14)$$

was next used. A detonation pressure of 33.7 ± 0.4 GPa was obtained, where the plus/minus is precision.

Lee et al. considered a time-zero timing error in the Lucite experiment.[8] The photographic record of the time shows the electrical signal rising to its highest potential at the explosive/disc 1 interface, then decaying exponentially downward, reaching the baseline at the disc 2/3 interface. The time-zero signal has a measurable risetime and turnover, whereas the disc-to-disc signals are sharp blips on a nearly flat line. Lee et al. concluded that 8.8 ns should be added to all the times in Table 6-3. This decreased the resulting velocities, and they obtained a detonation pressure of 31.6 ± 0.2 GPa.

J. Kury then ran various JWLs using the old 1-D code KOVEC for sample no. 40966 (13-mm thickness).[9] He found that 1-D runs of the 25-mm samples produced shorter times for the last interfaces. The disc 5/standoff interface occurs

at 996 to 1002 μs for 1-D runs of the 13 mm samples, but 961- to 974-μs values were obtained for the 25-mm samples. These values are caused by the added push given the same target, which is reflected in the code but not in Eq. (14). Only a limited set of values from $31.5 < P_p < 32.5$ GPa and $8.5 < E_o < 10.5$ kJ/cc were run, and all interface times agreed to within 1%. The best fit was to a JWL at 31.7 GPa and 8.5 kJ/cc. Nevertheless, the standard values of 31.5 GPa and 10.8 kJ/cc were first selected from this work.

Kury has recently recalculated the experimental results. The actual data are not available because the experiment was done by J. E. Kurrle at Mason & Hangar-Silas Mason Co. in Burlington, Iowa. Kury, therefore, returned to the results of Table 6-3, where he notes that the velocity of the disc 1/2 interface is uniformly high. A linear fit works best across the final four points, and this curve should be extrapolated back to time zero. The new shock wave velocities are 6.74 ± 0.07 mm/μs for the 13-mm samples and 6.90
± 0.05 mm/μs for the 25-mm samples.

We next need D. Steinberg's EOS for Lucite.[4] This is

$$U_m = C_o + S_1 u_m + S_2 (u_m / U_m) u_m, \qquad (15)$$

where the constants are 2.18 mm/μs, 2.088, and –1.124, respectively. The resulting particle velocities are 2.82 and 2.93 mm/μs for the 13- and 25-mm samples.

We must next decide on the detonation velocity for PETN. Nine cylinder shots and pin-switch measurements give a result of 8.26 ± 0.05 mm/μs with an average density of 1.765 ± 0.004 g/cc.[6] This is in agreement with the J. Kury / L. Green suggested value of 8.274 mm/μs at 1.763 g/cc.[9]

Using Eq. (14), we obtain 31.4 ± 0.7 and 32.9 ± 0.6 GPa for the detonation pressures from the 13- and 25-mm samples, where the pluses and minuses are precision.

5. Supracompression as a Search for C-J

The most exciting approach in the quest for the C-J or at least the adiabat detonation point, is the supracompression experiment. A high-speed flyer is used to detonate an explosive above the adiabat pressure. In this case, the explosive is being driven by a piston that holds the reaction products at constant pressure for several microseconds before they decay. The flyer velocity is slowly reduced in succeeding shots, and the pressure plateau drops as well. At the adiabat point, the piston stops holding up the plateau, and the pressure declines immediately. The 1-D behavior holds until the side effects affect the experiment.

Unfortunately, our data were not taken with time-dependent gauges but with individual measurements of the explosive particle velocity, u_p, and shock

velocity, U_s. From the Rankine-Hugoniot momentum relation, we calculate the explosive pressure,

$$P_p = \rho_0 U_s u_p. \tag{16}$$

This pressure may be plotted as a function of U_s until the known detonation velocity, D, is reached. If D is obtained from a steady-state cylinder shot and represents the infinite size of the explosive, then $P_p \longrightarrow P_{cj}$ (or P_a).

A different formalism was used to express this problem at the time, and it was based on C-J Theory. From the corresponding mass conservation requirement, we have

$$v = 1 - u_p/U_s, \tag{17}$$

from which we get

$$\partial u_p/\partial v = -U_s. \tag{18}$$

We rearrange and multiply each side by ∂U_s to obtain

$$\partial U_s/\partial v = -U_s\,(\partial U_s/\partial u_p). \tag{19}$$

We now consider a single product Hugoniot, H1, as shown in Fig. 6-2, with a set of decreasing Rayleigh Lines U_0, U_1, and U_2. The intersection points drop from A to B to C, which is the C-J point. The detonation velocity cannot decrease any further if this is the only Hugoniot, so that at C-J

$$\partial U_s/\partial v = 0. \tag{20}$$

From Eq. (19), with U_s nonzero,

$$\partial U_s/\partial u_p = 0 \tag{21}$$

at the C-J point. The researchers looked for the condition of Eq. (21). It is crucial to note that **Eq. (21) is true only if the explosive has reacted to equilibrium and can be represented by a single product Hugoniot.**
Eq. (21) was first derived by E. Lee[10], but the short derivation above comes from Al Nichols.

Let us consider an explosive not at equilibrium also shown schematically in Fig. 6-2. Suppose the first shot on the Rayleigh Line U1 produces the Hugoniot H1 and the intersection point B. The next shot is at lower flyer velocity and pressure so that the explosive has not reacted as far. Here, the Rayleigh Line U2 produces Hugoniot H2. Instead of intersecting at C, we now intersect at D, which is not the

C-J point. The C-J point is never reached because each succeeding Hugoniot is less-reacted than the preceding one. The result is that, if we look at point D at which $U_s = D_{cj}$, $\partial U_s / \partial u_p$ is **not** equal to zero because we came down a path from B to D. We could even continue to $U_s < D_{cj}$ and possibly obtain detonation, until finally, the initiation pressure becomes too low for detonation to occur. None of the measured points would ever reach the adiabat point but would be sonic detonation points. These points are not characteristic of the bulk explosive but are determined by the size and time of each particular experiment.

6. The Supracompressed PETN Experiment

Of special interest for the standard PETN JWL were the measurements on 1.76 g/cc PETN hit with flyer plates from the H-Division two-stage gas gun, which is capable of driving explosives above the adiabat point.[8, 11] More accurately, a flyer plate was used to strike a buffer plate of either aluminum or 1.763 g/cc PETN, which then sent a shock wave into the PETN to detonate it. The optically measured time for the shock wave to pass through the explosive from the buffer plate to the edge gave the shock velocity, U_s. Pins were used to measure the flyer-plate velocity, which was converted into the explosive particle velocity, u_p.

The data are listed in Table 6-4 with the calculated results and are summarized in Fig. 6-3, where it is seen that it is approaching $\partial U_s / \partial u_p \longrightarrow 0$ at the vertical line, which is the cylinder detonation velocity. The listed error is given as belonging to the shock velocity, and it varies from 0.3 to 3.3%. Mitchell and Nellis list 0.5–1.0% accuracy for 200-ns transit times on this same gun.[11] It was these pressure-volume values that were tried out with the standard JWL in Chapter 3 and found to fit within 5% up to 80 GPa, even though one is an adiabat and the other a Hugoniot.

This leads us to attempt to find the adiabat point as an asymptote at slightly lower volumes, where we are searching for $U_s = D$, the detonation velocity for the infinite-size, steady-state cylinder. We have adjusted D slightly by the 2/3 power of the density, to move from the standard 1.763 g/cc PETN to the 1.760 g/cc average for this experiment. We expect D to be about 8.265 mm/μs.

Although $\partial U_s / \partial u_p$ seems to approach zero, it is difficult to pick the intersection point with the vertical detonation velocity line. Along the Rayleigh Line, we require that

$$\partial P_s / \partial v = -\rho_0 D^2. \qquad (22)$$

The value of this derivative is expected to be about -120 g·mm^2/cc·μs^2. Unfortunately, the jitter in the few points in Table 6-4 makes this derivative useless. The range of the following points all are reasonable solutions for the detonation point:

u_p (mm/μs)	P_p (GPa)	v_p
2.00	29.1	0.758
2.11	30.7	0.745
2.16	**31.4**	**0.739**
2.27	33.0	0.725

(23)

Eq. (16) plus the U_s-u_p relations for aluminum are used to get these results. The value of 31.5 GPa was chosen at the time for the detonation pressure, P_j, in the standard PETN JWL. The error of trying to pick the intersection point, with $0.72 < v < 0.76$, is considerably larger than the 1 to 2% error estimated by C. Tarver and M. van Thiel to be in the impedance matching of each point.

In summary, the Lucite experiment gave detonation pressures for 1.763 g/cc PETN of 31.5 to 33 GPa. The plate velocity-jump-off pressures are 34 ± 4 GPa, and the cylinder velocity-jump-off pressures (see Chapter 5) are 32 ± 8 GPa. The thermochemical codes (Chapter 8) add to the confusion by all coming in low at 30.6 GPa in BKWR, 28.7 GPa in BKWS, 27.5 GPa in JCZ3, and 29.3 GPa in CHEQ.

The best measured detonation point comes from supracompression and is the only one we can call a possible adiabat pressure. The 1.763 g/cc PETN adiabat pressure is

$$P_a \sim 31 \pm 2 \text{ GPa}, \tag{24}$$

which is 2 GPa higher than the thermochemical code results.

PETN brings up the philosophical difficulties of the adiabat point vs the C-J point. According to C. Tarver and L. Green, PETN has a reaction zone so small that they were never able to measure it. However, Hayes found some electrical conductivity in PETN that he attributed to carbon.[12] A. Nichols calculates 0.6 mol/mol of diamonds in PETN at the C-J point (Table 8-4) in CHEQ, so that carbon precipitation is already under way. A C-J point, therefore, may never exist in any carbon-containing explosive because the time-dependent phenomenon of carbon coagulation is always present.

The practical question is whether the Principal Adiabat takes off at 32 or at 29 GPa. The larger question is that if true equilibrium never exists in any carbon-containing explosive, then all explosives must possess a size effect that would become apparent if we were careful enough. Thus, the adiabat point is defined as referring to "large-size" samples (for which we have data) rather than infinite-size, which exists only in the equilibrium code.

It finally suggests that the quest for C-J should perhaps move to compounds with no carbon. For us, such samples are the three RX-23-A explosives. These show the same 2-GPa difference between the JWL detonation pressure and the

calculated C-J pressure. Overall, the homogeneous explosives in Table 5-4 show a difference of 2 ± 1 GPa between the JWL detonation pressure and the CHEQ C-J point. Therefore, no trend is evident.

7. Supracompression of HMX and TATB

Three samples were measured in supracompression: PBX-9404, RX-26-AF, and LX-17. The first is HMX-based and the last TATB-based; the second is a mixture of the two. This experiment was reported with more confidence than the PETN work just described. The data from Green, et al. are listed in Table 6-5 and are plotted in Fig. 6-4.[13] The horizontal lines are the steady-state detonation velocities found from cylinder shots. Also included is the PBX-9404 data of Kinecke and West.[14]

It is clear in Fig. 6-4 that none of the three explosives show any tendency to turn toward the horizontal. Neither did any of the explosives in Kinecke and West's work.[14] The PBX-9404 and LX-17 data have no room left to turn without running into the steady-state cylinder detonation lines—unless one assumes that the lowest measured points are incorrect. While more accurate data would be helpful, we must consider that nonequilibrium behavior may be present.

In the Green et al. paper, the belief that $\partial U_s/\partial u_p$ must go to zero caused them to assume that the true C-J pressures were lower than previously believed. JWLs were used to fit the supracompression data. The best example was PBX-9404, which L. Green has recently privately replotted. The data run from particle velocities of 5.5 to 2.3 mm/μs. On such a broad scale, the C-J region looks small indeed. Green mentions that the one point near C-J may have sufficient error to allow a bend in the curve. It has been moved up enough so that the cylinder detonation velocity fits underneath. The JWL curve is then fit over the entire extent of the data with a 34-GPa JWL passing through the data and a 37-GPa JWL not passing through. It is not mentioned how many other JWLs with 37-GPa detonation points were tried. The other published fits for LX-17 and RX-26-AF do not even look close.[13]

As a result of this supracompression experiment, we cannot decide whether we obtained an adiabat point with even the degree of equilibrium possessed by the PETN results. It appears that we did not. Further work will be needed, preferably with pressure gauges, to unravel this problem.

We shall extrapolate the data of Table 6-5 down to the steady-state detonation velocities as best we can. These are 8.76, 8.22 (extrapolated from 8.24 for 1.844 g/cc), and 7.63 mm/μs for PBX-9404, RX-26-AF, and LX-17. The PBX-9404 is close to the detonation point, as is the LX-17, except that its relative volume is too low. The RX-26-AF has a low volume as well, and the extrapolation is a long one. The detonation pressure results are shown below in GPa, with the standard deviations being precision.

	One-dimensional plate		
	Jump-off velocity	Green supra-compress	Our supra-compress
PBX-9404	39 ± 1	34	38 ± 2
PETN	34 ± 4	32	32 ± 1.5
RX-26-AF		32	34 ± 2
LX-17	34 ± 0	28	32 ± 2

(25)

We recall from Chapter 4 that the jump-off velocities for LX-17 included plate thicknesses from 0.10 to 2.5 mm. With the Green pressures now being considered too low because of the mode of extrapolation, we see that the plate jump-off velocity and supracompression results are in agreement.

8. References

1. J. M. Walsh and R. H. Christian, *Phys. Rev.* **97,** 1544 (1955).

2. R. E. Duff and E. Houston, *J. Chem. Phys.* **23,** 1268 (1955).

3. W. E. Deal, *J. Chem. Phys.* **27,** 796 (1957).

4. D. J. Steinberg, *Equation of State and Strength Properties of Selected Materials,* Lawrence Livermore National Laboratory, Livermore, CA, UCRL-MA-106439 (1991).

5. K. K. Shvedov, *Combustion, Explosives, Shock Waves* **23,** 464 (1987).

6. H. C. Hornig, E. L. Lee, M. Finger and J. E. Kurrle, "Equation of State of Detonation Products," *Proceedings Fifth Symposium (International) on Detonation,* Pasadena, CA, August 18–21, 1970, p. 503.

7. B. Hayes, *J. Appl. Phys.* **38,** 507 (1967).

8. E. L. Lee, M. van Thiel, L. G. Green, and A. Mitchell, "Detonation Product EOS: The Region above Chapman Jouget Pressure," presented at the Lawrence Livermore American Physical Society 1983 Topical Conference on Shock Waves in Condensed Matter, Santa Fe, NM, July 18–21, 1983.

9. L. Green, N. Holmes, and J. Kury, "Shock Measurements on Explosives in the Supra-Compressive Region," presented at the Int'l Symposium on Pyrotechnics and Explosives, Beijing, China, October 12–15, 1987; (UCRL-95461, 1987).

10. Memo from E. L. Lee to R. Weingart, December 20, 1984.

11. A. C. Mitchell and W. J. Nellis, *Rev. Sci. Instr.* **52,** 347 (1981).

12. B. Hayes, "On Electrical Conductivity in Detonation Products," *Proceedings Fourth Symposium (international) on Detonation,* White Oak, MD, October 12–15, 1965, p. 595.

13. L. Green, E. Lee, A. Mitchell, and C. Tarver, "The Supra-Compression of LX-07, LX-17, PBX-9404, and RX-26-AF and the Equations of State of the Detonation Products," *Proceedings Eighth Symposium (International) on Detonation,* Albuquerque, NM, July 15–19, 1985, pp. 587–595.

14. J. H. Kinecke, Jr. and C. E. West, Jr., "Shocked States of Four Overdriven Explosives," *Proceedings Fifth Symposium (International) on Detonation,* Pasadena, CA, August 18–21, 1970, pp. 533–542.

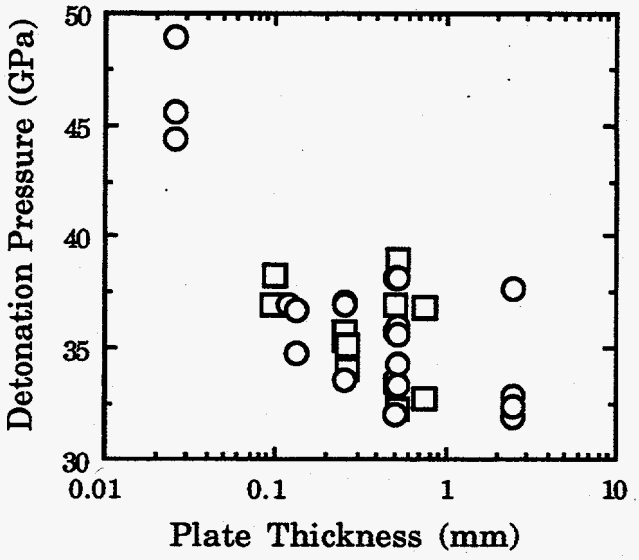

Fig. 6-1. Detonation pressure, as calculated from impedance matching, for metal plates pushed by LX-14, which has a reaction zone of about 0.1 mm. Hence, the 44-GPa LX-14 point is the expected spike, and the 36 GPa cluster of lower points is close to the expected C-J point. The data show LX-14 on Ta (open squares) and LX-14 on Cu (open circles).

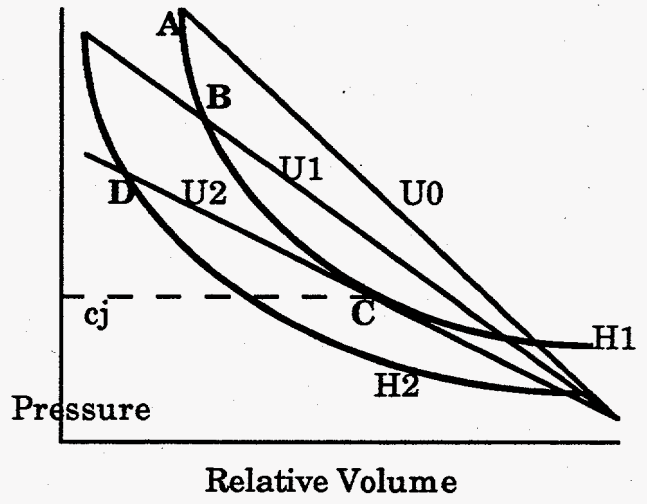

Fig. 6-2. Schematic of detonation in the pressure-volume plane according to C-J Theory. If H1 is the only product Hugoniot, then supracompression Rayleigh Lines U0, U1, and U2 create intersection points A, B, and C. C is the C-J point, and the two curves are tangent. However, suppose U1 creates the nonequilibrium Hugoniot H1 with the intersection point B. Then the next, lower pressure Rayleigh Line U2 creates the less-reacted Hugoniot H2 with the intersection point D. We never reach a C-J point with the tangency condition.

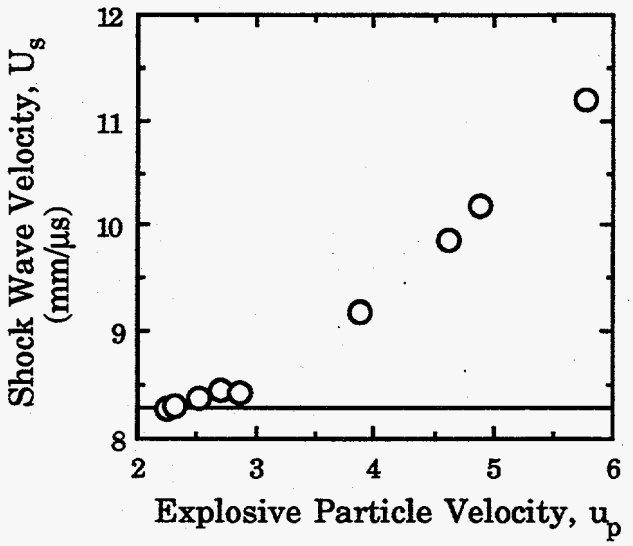

Fig. 6-3. Supracompression shock velocity vs. particle velocity data for 1.760 g/cc PETN. The horizontal line is the steady state cylinder detonation velocity toward which the data are headed. The shape suggests that $\partial U_S/\partial u_p$ is indeed heading toward zero as expected for an ideal explosive.

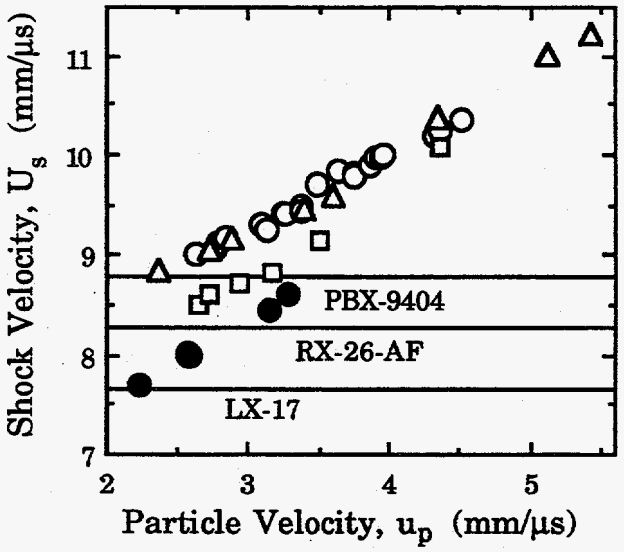

Fig. 6-4. Supracompression plot for three explosives. The horizontal lines are the steady state cylinder detonation velocities to which the points are extrapolated. None of the three shows any bending toward the horizontal, a sign of nonideal behavior. The explosives, from top to bottom, are: PBX-9404 (open circles) and (open triangles; RX-26-AF (open squares), and LX-17 (filled circles).

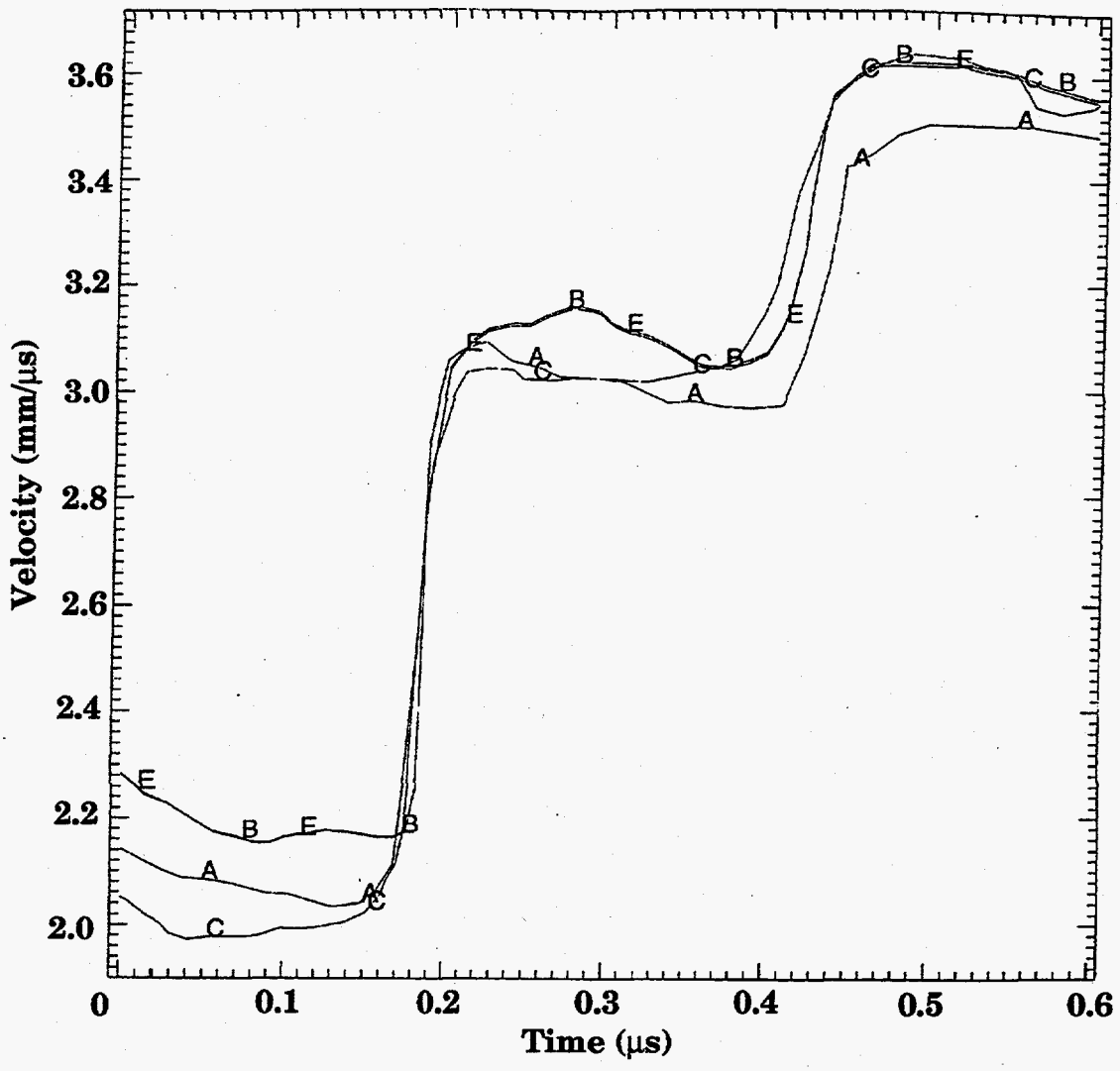

Curve	Label	X-min	X-max	Y-min	Y-max	File
A	*1x14 in phm85039 f. old dv9634b, 9634	–0.0404	0.972	2.03	3.77	uphm85039
B	1x–14 9577 mm/ms vs ms	–0.0186	1.43	2.15	4.28	uphm85017
C	1x–14 9578 mm/ms vs ms	–0.0196	1.17	1.97	4.16	uphm85018
E	*9577a1x–14 0514e08	–0.0186	1.43	2.15	4.28	uphm85041

Fig. 6-5. Overlay of four, identical 1-D electric gun shots with 20-mm LX-14 on 0.51-mm copper plates. The flyer velocity was 4.3 mm/μs, and Fabry interferometry was used. The variability in jump-off suggests that the detonation point is actually an undefined band. The samples are phm85017, 18, 39, and 41.

Table 6-1. Jump-off velocities and calculated detonation pressures from 1-D plate shots. All flyers were 0.25 mm Mylar. The * indicates a fine-grained explosive; ** means the sample was probably overdriven. The samples are arranged in the order of increasing plate thickness.

Explosive	Shot no.	Plate	Jump-off velocity (mm/μs)	**Calc det pressure (GPa)**	Thickness explosive (mm)	Plate thickness (mm)	Explosive density (g/cc)	Flyer velocity (mm/us)	Det velocity D (mm/μs)
LX-14	9632	Cu	2.80	**48.9**	25.58	0.0254	1.83	4.3	8.79
	9643	Cu	2.65	**45.6**	25.58	0.0254	1.83	4.3	8.79
	phm85047	Cu	2.59	**44.4**	25.58	0.0254	1.83	4.3	8.79
	phm85001	Ta	1.66	**36.9**	5.47	0.096	1.79	4.3	8.66
	phm90004	Ta	1.70	**38.3**	5.00	0.10	1.84	4.1	8.83
	phm85011	Cu	2.24	**37.0**	20.18	0.12	1.83	4.3	8.79
	phm85014	Cu	2.22	**36.7**	19.97	0.13	1.84	4.1	8.82
	phm85011	Cu	2.13	**34.8**	20.30	0.13	1.82	4.3	8.77
	phm90003	Ta	1.59	**35.4**	5.00	0.25	1.84	4.1	8.83
	phm90001	Ta	1.61	**35.8**	10.92	0.25	1.82	4.1	8.77
	phm85040	Cu	2.24	**37.1**	40.00	0.25	1.84	4.3	8.82
	phm85035	Cu*	2.24	**36.9**	40.15	0.257	1.83	4.3	8.79
	phm85036	Cu*	2.07	**33.6**	40.15	0.257	1.83	4.3	8.79
	phm85003	Ta	1.61	**35.1**	13.22	0.264	1.69	4.3	8.35
	phm85004	Ta	1.57	**34.1**	13.22	0.264	1.69	4.3	8.35
	phm85017	Cu	2.29	**38.1**	20.15	0.505	1.83	4.3	8.80
	phm85018	Cu	2.07	**33.6**	20.15	0.505	1.83	4.3	8.79
	phm90002	Ta	1.64	**36.9**	10.00	0.51	1.86	4.1	8.89
	phm85039	Cu	2.18	**35.8**	20.00	0.51	1.84	4.3	8.82
	phm85041	Cu	2.30	**38.2**	20.00	0.51	1.84	4.3	8.82
	phm85020	Al	3.58	**33.2**	20.23	0.515	1.83	4.3	8.79
	phm85021	Al	3.47	**32.0**	20.23	0.515	1.83	4.3	8.79
	phm85013	Cu	2.30	**38.2**	10.00	0.523	1.83	4.3	8.79

Table 6-1, part 2

Explosive	Shot no.	Plate	Jump-off velocity (mm/μs)	**Calc det pressure (GPa)**	Thickness explosive (mm)	Plate thickness (mm)	Explosive density (g/cc)	Flyer velocity (mm/us)	Det velocity D (mm/μs)
LX-14	phm85005	Ta	1.76	**39.0**	26.51	0.525	1.69	4.3	8.35
	phm85006	Ta	1.50	**32.3**	26.51	0.525	1.69	4.3	8.35
	phm85033	Cu*	2.19	**36.0**	19.95	0.526	1.83	4.3	8.79
	phm85034	Cu*	2.17	**35.6**	19.95	0.526	1.83	4.3	8.79
	phm85015	Cu	2.05	**33.3**	20.00	0.530	1.84	4.3	8.82
	phm85016	Cu	2.10	**34.3**	10.01	0.532	1.84	4.3	8.82
	phm85016	Cu	2.10	**34.3**	10.01	0.532	1.84	4.3	8.82
	phm85007	Ta	1.51	**32.8**	38.91	0.769	1.77	4.3	8.60
	phm85008	Ta	1.66	**36.8**	38.91	0.769	1.77	4.3	8.60
	phm85024	Cu	2.03	**32.9**	101.6	2.502	1.84	lens	8.82
	phm85025	Cu	2.27	**37.7**	101.6	2.520	1.84	lens	8.82
	phm85046	Cu	1.98	**31.9**	91.07	2.53	1.84	lens	8.82
	phm85045	Cu	2.00	**32.4**	92.02	2.53	1.84	lens	8.82
PBX-9404	phm86002	Ta	1.76	**39.9**	15.00	0.25	1.84	4.3	8.73
	phm86005	Ta	1.76	**39.9**	30.00	0.25	1.84	4.3	8.73
	phm86003	Ta	1.73	**39.1**	15.00	0.51	1.84	4.3	8.73
	phm86006	Ta	1.67	**37.5**	30.00	0.51	1.84	4.3	8.73
PETN	ppe87001	Ta	1.64	**35.8**	5.00	0.10	1.71	5.7	8.11
	ppe87002	Ta	1.34	**28.2**	5.00	0.10	1.72	5.7	8.13
	ppe87003	Ta	1.74	**38.4**	5.00	0.10	1.71	5.7	8.12
	ppe86001**	Ta	1.66	**36.7**	20.00	0.10	1.78	4.1	8.34
	ppe86002**	Ta	1.70	**37.6**	20.00	0.10	1.76	4.1	8.26
	ppe86008	Ta	1.64	**35.9**	20.00	0.10	1.73	4.1	8.17
	ppe87004	Ta	1.42	**30.2**	5.00	0.25	1.71	5.7	8.11
	ppe87005	Ta	1.44	**30.7**	5.00	0.25	1.71	5.7	8.12

Table 6-1, part 3

Explosive	Shot no.	Plate	Jump-off velocity (mm/μs)	**Calc det pressure (GPa)**	Thickness explosive (mm)	Plate thickness (mm)	Explosive density (g/cc)	Flyer velocity (mm/us)	Det velocity D (mm/μs)
PETN	ppe88003	Ta	1.46	**31.2**	10.00	0.25	1.71	4.1	8.11
	ppe86004**	Ta	1.81	**40.5**	20.00	0.25	1.76	4.1	8.26
	ppe86006**	Ta	1.62	**35.5**	20.00	0.25	1.77	4.1	8.29
	ppe86007	Ta	1.32	**27.8**	20.00	0.25	1.73	4.1	8.17
LX-17	1983 report	Al	3.87	**36.4**	17.00	0.243	1.83	1.9	8.79
	1983 report	Cu	1.95	**31.4**	14.00	0.433	1.84	1.1	8.82
	1983 report	Cu	2.25	**37.3**	17.00	0.249	1.84	2.0	8.82
	1983 report	Cu	2.38	**40.0**	17.00	0.103	1.84	1.9	8.82
	pta90004	Ta	1.56	**33.9**	5.00	0.10	1.90	4.3	7.62
	pta86003	Ta	1.70	**37.6**	20.00	0.10	1.90	4.3	7.62
	pta86008	Ta	1.77	**39.4**	20.00	0.10	1.90	4.3	7.62
	pta90005	Ta	1.57	**34.2**	5.00	0.25	1.90	4.3	7.62
	pta90001	Ta	1.61	**35.1**	10.00	0.25	1.90	4.3	7.62
	pta90002	Ta	1.63	**35.7**	15.00	0.25	1.90	4.3	7.62
	pta86005	Ta	1.67	**36.8**	20.00	0.25	1.90	4.3	7.62
	pta86010	Ta	1.66	**36.5**	20.00	0.25	1.90	4.3	7.62
	pta90003	Ta	1.54	**33.4**	15.00	0.51	1.90	4.3	7.62
	pta86007	Ta	1.59	**34.7**	20.00	0.51	1.90	4.3	7.62
	pta86012	Ta	1.57	**34.2**	20.00	0.51	1.90	4.3	7.62
	pta86006	Ta	1.65	**36.3**	40.00	0.51	1.90	4.3	7.62
	pta86011	Ta	1.62	**35.5**	40.00	0.51	1.90	4.3	7.62
	pta86004	Ta	1.51	**32.7**	20.00	0.76	1.90	4.3	7.62
	pta86009	Ta	1.55	**33.7**	20.00	0.76	1.90	4.3	7.62
	pta85005	Ta	1.62	**35.5**	99.10	1.52	1.90	lens	7.62
	pta85003	Ta	1.56	**33.9**	98.30	2.54	1.90	lens	7.62

Table 6-1, part 4

Explo-sive	Shot no.	Plate	Jump-off velocity (mm/μs)	**Calc det pressure (GPa)**	Thick-ness explosive (mm)	Plate thick-ness (mm)	Explosive density (g/cc)	Flyer velocity (mm/us)	Det velocity D (mm/μs)
	pta85004	Ta	1.55	**33.7**	99.10	2.54	1.90	lens	7.62
	pta85001	Cu	2.09	**33.2**	100.00	2.54	1.90	lens	7.62
	pta85002	Cu	2.11	**33.6**	100.00	2.54	1.90	lens	7.62
TNT	ptn86011	Cu	2.04	**30.7**	17.80	0.03	1.62	4.3	7.05
	ptn86012	Cu	2.05	**30.9**	17.80	0.03	1.62	4.3	7.05
	ptn86004	Cu	1.42	**19.9**	38.60	0.03	1.62	4.3	7.05
	ptn86013	Cu	2.06	**31.0**	38.60	0.03	1.62	4.3	7.05
	ptn86007	Cu	1.94	**28.9**	38.60	0.05	1.62	4.3	7.05
	ptn86008	Cu	1.97	**29.4**	38.60	0.05	1.62	4.3	7.05
	ptn86006	Cu	1.85	**27.3**	38.60	0.13	1.62	4.3	7.05
	ptn87001	Ta	1.01	**12.0**	101.60	1.52	1.63	lens	7.06
	ptn87002	Ta	1.04	**20.5**	101.60	1.52	1.63	lens	7.06

Note: the LX-14 9632 and 9643 numbers are from E. Lee, et. al., 8th Det. Symposium, p. 621. They are incresead by 7% to match our jump-off and the published value for the third 1 mil shot, phm85047. This data must be taken as rough.
Note: the pta90000 series is LX-17-0; the others are LX-17-1.

Table 6-2. Fraction of kinetic energy put into various plates at the scaled times of 0.5 and 1.0 μs for a 10 mm-thick explosive. Sorting is by metal, then the ratio of explosive-to-plate thickness.

Explosive	Shot no.	Plate	Scaled time re 1 μs at 10 mm	Velocity (mm/μs) At scaled 0.5 μs	Velocity (mm/μs) At scaled 1 μs	% energy out At scaled 0.5 μs	% energy out At scaled 1 μs	Ratio thick HE /Plate	He thick mm	Plate thick (nm)
LX-14	phm85020	Al	2.0	5.71	5.98	9.4	11	39	20	508
	phm85021	Al	2.0	5.66	5.95	9.2	10	39	20	508
	phm85013	Cu	1.0	3.04	3.42	18	24	20	10	508
	phm85016	Cu	1.0	2.99	3.34	18	23	20	10	508
	phm85033	Cu	1.9	3.82	4.32	15	20	37	19	508
	phm85034	Cu	1.9	3.81	4.30	15	20	37	19	508
	phm85015	Cu	2.0	3.97	4.36	17	20	39	20	508
	phm85039	Cu	2.0	3.82	4.31	15	19	39	20	508
	phm85041	Cu	2.0	4.12	4.43	17	20	39	20	508
	phm85017	Cu	2.0	4.13	4.43	17	20	39	20	508
	phm85018	Cu	2.0	4.09	4.42	17	20	39	20	508
	phm85014	Cu	1.9	5.83	6.14	7.9	8.9	187	19	102
	phm90003	Ta	0.5	2.11	2.62	13	23	20	5	254
	phm90002	Ta	1.0	2.12	2.56	16	24	20	10	508
	phm90001	Ta	1.0	3.12		16		39	10	254
	phm90004	Ta	0.5	3.69	4.08	17	22	49	5	102
	phm85001	Ta	0.5	3.66	4.11	13	18	49	5	102
	phm85007	Ta	3.8	3.34		17		50	38	762
	phm85008	Ta	3.8	3.38		18		50	38	762
	phm85003	Ta	1.3	3.38		16		51	13	254
	phm85004	Ta	1.3	3.41		17		51	13	254
PETN	ppe87004	Ta	0.5	1.89	2.36	3.7	12	20	5	254
	ppe87005	Ta	0.5	1.92	2.36	4.2	12	20	5	254
	ppe88003	Ta	1.0	2.83		14		39	10	254

Table 6-2, part 2

Explosive	Shot no.	Plate	Scaled time re 1 μs at 10 mm	Velocity (mm/μs) At scaled 0.5 μs	Velocity (mm/μs) At scaled 1 μs	% energy out At scaled 0.5 μs	% energy out At scaled 1 μs	Ratio thick HE /Plate	He thick mm	Plate thick (nm)
PETN	ppe87001	Ta	0.5	3.50	3.90	9.1	14	49	5	102
	ppe87002	Ta	0.5	3.43	3.85	8.3	13	49	5	102
	ppe87003	Ta	0.5	3.43	3.86	8.3	14	49	5	102
LX-17	pta90005	Ta	0.5	1.90	2.26	13	22	20	5	254
	pta86004	Ta	2.0	2.25		21		26	20	762
	pta86009	Ta	2.0	2.28		22		26	20	762
	pta90003	Ta	1.5	2.21		17		30	15	508
	pta90001	Ta	1.0	2.67	3.00	17	23	39	10	254
	pta86007	Ta	2.0	2.65		19		39	20	508
	pta86012	Ta	2.0	2.63		19		39	20	508
	pta90004	Ta	0.5	2.89	3.15	11	15	49	5	102
	pta90002	Ta	1.5	3.02		16		59	15	254

Note: the 51 mm diameter pta86000 series had 3 mm of LX-10 before the LX-17. The 25 mm pta90000 series did not use a driver.

Table 6-3. Summary of as-measured Lucite PETN data for densities of about 1.763 g/cc. The times from top to bottom are for the interfaces between discs 1/2, 2/3, 3/4, 4/5, and 5/standoff. The explosive/disc 1 interface is time zero by definition.

25 mm (1 in.) length- Original data					13 mm (1/2 in.) length- Original data				
	Distance (μm)	Mid point (μm)	Time (ns)	Vel. (mm/ms)		Distance (μm)	Mid point (μm)	Time (ns)	Vel. (mm/ms)
Exp 40934	1265	633	181	6.99	Exp 40936	1303	652	183	7.12
(D1A)	2563	1914	371	6.83	(D1HA)	2548	1926	376	6.45
25 mm dia.	3830	3197	562	6.63	25 mm dia.	3843	3196	577	6.44
x25.40 mm	5095	4463	755	6.55	x12.85 mm	5108	4476	779	6.26
1.763 g/cc	6360	5728	951	6.45	1.763 g/cc	6373	5741	984	6.17
Exp 40933	1285	643	184	6.98	Exp 40932	1295	648	184	7.04
(D1B)	2570	1928	375	6.73	(D1HB)	2558	1927	378	6.51
25 mm dia.	3846	3208	570	6.54	25 mm dia.	3830	3194	575	6.46
x25.75 mm	5131	4489	767	6.52	x12.73 mm	5103	4467	777	6.30
1.758 g/cc	6393	5762	965	6.37	1.763 g/cc	6373	5738	985	6.11
Exp 40931	1285	643	187	6.87	Exp 40966	1285	643	182	7.06
(D2A)	2548	1917	375	6.72	(D2HA)	2560	1923	377	6.54
51 mm dia.	3823	3186	567	6.64	51 mm dia.	3838	3199	574	6.49
x25.32 mm	5105	4464	762	6.57	x12.62 mm	5108	4473	778	6.23
1.762 g/cc	6373	5739	959	6.44	1.763 g/cc	6388	5748	986	6.15
Exp 40912	1293	647	183	7.07	Exp 40949	1280	640	181	7.07
(D2B)	2578	1936	373	6.76	(D2HB)	2553	1917	373	6.63
51 mm dia.	3843	3211	564	6.62	51 mm dia.	3840	3197	572	6.47
x25.37 mm	5121	4482	759	6.55	x12.51 mm	5123	4482	774	6.35
1.763 g/cc	6388	5755	955	6.46	1.764 g/cc	6411	5767	980	6.25

Table 6-4. Supracompressed PETN experimental data. The line in italics is the expected C-J point with a detonation velocity, D, of 8.265 mm/μs. Although $\Delta U_s/\Delta u_p$ is approaching zero, how to extrapolate to the C-J point is not easy.

PETN target									
	(mm/μs)			Calc.	Calc.				
Density	Meas. Velocity		Error	pressure	volume		Flyer plate		Buffer
(g/cc)	U_s	u_p	U_s	(GPa)	v	$\Delta P/\Delta v$		(mm/μs)	plate
1.760	*8.265*								
1.761	8.298	2.320	0.074	33.9	0.720		Al	3.960	Al
1.761	8.384	2.518	0.032	37.2	0.700	-158	Al	4.280	Al
1.758	8.452	2.692	0.060	40.0	0.681	-155	Al	4.555	Al
1.763	8.429	2.856	0.048	42.4	0.661	-120	Al	4.810	PETN
1.757	9.194	3.886	0.300	62.8	0.577	-243	Al	6.492	PETN
1.757	9.859	4.629	0.049	80.2	0.530	-372	Al	7.729	PETN
1.766	10.200	4.883	0.120	88.0	0.521	-844	Ta	5.998	PETN
1.759	11.206	5.768	0.034	114	0.485	-715	Ta	7.116	PETN

Table 6-5. Summary of supracompressed data for three less-ideal explosives. "L" is the LLNL data; "K" is Kinecke and West. The Kinecke and West velocity in the next to last column is the buffer's unconfined face velocity. The LLNL velocity in the same column is the flyer velocity.

Explosive	Density g/cc	all mm/μs Velocity U_s	u_p	Listed error U_s	u_p	Pressure (GPa)	Volume v		Flyer plate	Vel. mm/μs	Buffer plate
PBX-9404	1.844	8.85	2.353	0.04	0.01	38.4	0.734	L	Al	4.164	9404
	1.839	9.01	2.63	0.11		43.6	0.708	K	Mo	3.34	Mo
	1.841	9.07	2.723	0.06	0.02	45.5	0.700	L	Al	4.779	Al
	1.839	9.07	2.77	0.12		46.2	0.695	K	Mo	3.50	Mo
	1.839	9.12	2.79	0.10		46.8	0.694	K	Mo	3.55	Mo
	1.839	9.17	2.84	0.08		47.9	0.690	K	Mo	3.61	Mo
	1.841	9.17	2.874	0.08	0.02	48.5	0.687	L	Al	5.032	Al
	1.839	9.31	3.08	0.14		52.7	0.669	K	Mo	3.91	Mo
	1.839	9.24	3.12	0.18		53.0	0.662	K	Mo	3.97	Mo
	1.839	9.41	3.24	0.08		56.1	0.656	K	Mo	4.12	Mo
	1.839	9.42	3.25	0.14		56.3	0.655	K	Mo	4.13	Mo
	1.839	9.43	3.37	0.21		58.4	0.643	K	Mo	4.29	Mo
	1.839	9.49	3.37	0.13		58.8	0.645	K	Mo	4.29	Mo
	1.844	9.47	3.399	0.05	0.02	59.4	0.641	L	Al	5.901	9404
	1.839	9.70	3.49	0.13		62.3	0.640	K	Mo	4.45	Mo
	1.844	9.59	3.591	0.10	0.04	63.5	0.626	L	Al	6.218	9404
	1.839	9.83	3.63	0.15		65.6	0.631	K	Mo	4.64	Mo
	1.839	9.78	3.76	0.11		67.6	0.616	K	Mo	4.80	Mo
	1.839	9.81	3.75	0.12		67.7	0.618	K	Mo	4.79	Mo
	1.839	9.89	3.86	0.07		70.2	0.610	K	Mo	4.92	Mo
	1.839	9.96	3.91	0.09		71.6	0.607	K	Mo	4.99	Mo
	1.839	9.98	3.94	0.11		72.3	0.605	K	Mo	5.03	Mo
	1.839	10.01	3.97	0.13		73.1	0.603	K	Mo	5.07	Mo
	1.839	10.19	4.32	0.12		81.0	0.576	K	Mo	5.53	Mo
	1.839	10.23	4.36	0.24		82.0	0.574	K	Mo	5.59	Mo
	1.841	10.37	4.343	0.07	0.02	82.9	0.581	L	Al	7.533	Al
	1.839	10.36	4.52	0.11		86.1	0.564	K	Mo	5.78	Mo
	1.841	11.03	5.130	0.06	0.03	104.2	0.535	L	Ta	6.402	9404
	1.843	11.23	5.424	0.07	0.04	112.3	0.517	L	Ta	6.760	9404
RX-26 AF	1.835	8.50	2.64	0.04	0.01	41.2	0.689	L	Al	4.547	Al
	1.837	8.62	2.73	0.08	0.03	43.2	0.683	L	Al	4.710	Al
	1.832	8.72	2.93	0.02	0.01	46.8	0.664	L	Al	5.028	Al
	1.836	8.82	3.17	0.04	0.15	51.3	0.641	L	Al	5.416	RX26
	1.837	9.14	3.50	0.08	0.04	58.8	0.617	L	Al	5.988	Al
	1.837	10.09	4.36	0.07	0.03	80.8	0.568	L	Al	7.493	Al

Table 6-5, part 2

Explosive	Density g/cc	all mm/μs Velocity U_s	all mm/μs Velocity u_p	Listed error U_s	Listed error u_p	Pressure (GPa)	Volume v		Flyer plate	Flyer mm/μs	Buffer plate
LX-17	1.906	7.70	2.222	0.04	0.02	32.6	0.711	L	Al	3.813	Al
	1.903	7.70	2.223	0.04	0.02	32.6	0.711	L	Al	3.813	LX17
	1.901	8.02	2.563	0.04	0.01	39.1	0.680	L	Al	4.400	LX17
	1.898	7.98	2.569	0.04	0.01	38.9	0.678	L	Al	4.400	LX17
	1.905	8.00	2.587	0.02	0.01	39.4	0.677	L	Al	4.436	LX17
	1.903	8.44	3.134	0.04	0.02	50.3	0.629	L	Al	5.355	LX17
	1.902	8.60	3.284	0.03	0.01	53.7	0.618	L	Al	5.612	Al

Chapter 7. TATB Nonideality

1. Detonation Front Curvature

LX-17, which is based on TATB, is the LLNL version of a nonideal explosive. It is not very nonideal, nothing like a composite explosive. However, it was the first LLNL production explosive to substantially deviate from classical behavior. We noted in the preceding chapter how the cylinder JWL detonation pressure, P_j, is significantly lower than the impedance-match plate push pressure, P_d, which is caused by nonideality. This result caused confusion when the first LX-17 JWLs were made. Moreover, LX-17 has a size effect. The critical or failure diameter of LX-17 is listed as less than 9.4 mm for 20-μm powder and between 6.4 and 9.5 mm for 60-μm material.[1] Campbell and Engelke found no detonation at diameters below 8 mm in bare rate sticks of PBX-9502 (95% TATB, 5% Kel-F).[2]

LLNL velocities for LX-17 increased slightly from 7.59 to 7.63 mm/μs from the 25- to the 51-mm cylinder. The PBX-9502 sticks of 50-mm diameter showed a detonation velocity of 7.665 mm/μs, while a 108-mm stick gave 7.729 mm/μs.[3] There is no reason to suppose that 108 mm is infinite-diameter, but our largest 51-mm-diameter LX-17 shots certainly are not. We would estimate an infinite-size detonation velocity of about 7.69 mm/μs for our LX-17 at 1.905 g/cc.

However, the curvature of its detonation front graphically gives the explosive a nonideal character not possessed by the other explosives so far considered in this report. The curvature of the detonation front is measured end-on in a cylinder test. A metal fixture over the end has a slit running across a diameter. Streak camera film is pulled past the slits as the detonation front arrives. The fastest part of the front along the axis of the cylinder arrives first at the film, and the explosive-metal interfaces arrive later. The lag of the detonation front may then be calculated from the streak-camera speed and the detonation velocity, which is the same over the entire front at steady state.

Five cylinder experiments have been run at LLNL, and the results are shown in Fig. 7-1 and Table 7-1. The first three—LX-04, LX-10, and LX-17—did not have the end-slit on the diameter. Instead, the longest slit was displaced 1.0 to 2.5 mm from the diameter. The explosive-wall interface was difficult to see and the total picture of the cylinder top was distorted—which is why the radii listed in Table 7-1 are less than 50.8 mm. For LX-04 and LX-10, other, more-off-center, slits were selected to obtain the best interface data, and an unknown amount of distortion affected these results. Recently, the slit was moved onto the diameter. The two subsequent RX-52 runs are excellent, with good interfaces and a complete diameter is observed. Both are TATB-based explosives. RX-52-AD contains 65 wt% TATB, 31.9% FEFO and 3.1 oil, and has

a 1.81 g/cc density. RX-52-AE contains 65.0% TATB and 35% RX-44 lacquer. From Fig. 7-1, we note that the TATB/FEFO explosives show the same amount of curvature as the LX-17.

Also plotted in Fig. 7-1 is LANL data on PBX-9502 (95 wt% TATB, 5% Kel-F, 1.89 g/cc) kindly given us by John Bdzil.[4] Three different diameters of rate sticks are included, and we see the increased curvature of the detonation front as the diameter decreases. The data were taken on rate sticks, not cylinders, so there is no lateral confinement with copper. We see that there is more curvature with less confinement.

Of importance is the limiting angle of the detonation front with the cylinder wall. Lambourn and Swift define the angle Θ_c as the angle of incidence, that is, the angle between the detonation front and the normal to the wall.[5] This angle is hard to measure, and the LX-17 data in Fig. 7-1 are not good enough. The RX-52 data are better, and we analyze five points near the edge to obtain:

RX-52-AD	12°, 13°
RX-52-AE	12°, 14°.

(1)

These data are in agreement with the British observation that an angle of about 12° is seen for all explosives against any material.[6] The LANL data in Fig. 7-1 at 50-, 18-, and 12-mm diameters produce limiting angles of 27, 22, and 23°. The reason for the discrepancy, a factor of 2, is not known at this time.

An outgrowth of the experimentally measured curved detonation front is the "corner-turning" mapping model of Lambourn and Swift (the WBL—for Whitham, Bdzil, Lambourn)[5] and J. B. Bdzil (the DSD—for Detonation Shock Dynamics).[7–9] In the code, a perpendicular basis vector is assigned to each element of the detonation surface. Let the angle between the basis vector and the direction of detonation along the cylinder axis be ϕ. The detonation velocity, D, lies along the axis. The detonation velocity normal to the detonation front is $D\cos\phi$. The code is written so that the normal of the detonation velocity determines the position of the next element. Because the maximum curvature is next to the walls, corner-turning is allowed. The hydrocode can now run around corners using input from experiment, but without making any adjustments to the inherent EOS of the explosive. Fine zoning is needed if extreme curvature is to be shown accurately.

This approach requires that the detonation front curvature be measured and available as input. Some means must be found to modify the detonation velocity for different sizes of cylinders. The measured steady-state detonation velocity, D_s, in a cylinder is usually related to the infinite volume velocity, D_∞, by

$$D_s = D_\infty (1 - A / R), \qquad (2)$$

where A is a constant and R is the radius. The corner-turning models assign a velocity to each part of the curved front, D_κ, according to

$$D_\kappa = D_s (1 - \alpha\kappa), \qquad (3)$$

where κ is the curvature at each point of the detonation front and α is a constant. The velocity, D_κ, is perpendicular to the front at each point, and this provides a vector that causes motion away from the cylinder axis and around corners.

The corner-turning models all require actual data in order to derive Eqs. (2) and (3), which are input to the code. Detonation velocity is the only hard data that comes out of most detonation measurements so that explicitly including it as input seems reasonable and desirable. The program burn, which also uses explicit velocities, is the only initiation sequence used in a production code at LLNL. Neither the beta burn nor Ignition & Growth require a detonation velocity—nor can it be seen in their outputs, short of measuring the difference between two graphs at different times. The presence of an explicit detonation velocity appears to be a necessary component in selling a production code.

Harold Zimmerman has compared the curvature phenomenon with the 1-D supracompression data in the previous chapter. For the size effect in cylinders, $D_s < D_\infty$. He notes that Hull looked at colliding shock waves.[10] Instead of finding a straight Mach stem between them, he found a concave shock front that agrees with Eq. (3), but here κ is negative and $D_s > D_\infty$. Thus, for the same explosive, Eq. (3) holds with U_s passing continuously through the C-J (actually, the adiabat point). In order to have $\partial U_s / \partial u_p$ equal zero, u_p would have to go through an infinite jump. Thus, $\partial U_s / \partial u_p$ is unequal to zero along this path. However, A. Nichols believes that the size effect in the cylinder is a different effect than initiation and that the colliding shock waves create states on a different Hugoniot.

2. Summary of Measured Pressures and Theory

The detonation pressures measured in this report often represent different things. To go further requires consideration of the basic theories. The old C-J Theory starts with detonation at the C-J point and an adiabat expanding to larger volumes. The JWL is made to fit this theory, although there is no reason why the JWL detonation point has to be the C-J point. In any case, the use of the JWL with program burn in hydrocodes predisposes its users to the C-J model.

The newer ZND Theory (for Zeldovich, von Neumann, and Doring) starts with the solid explosive being compressed to the von Neumann spike. As the explosive burns, it drops down the Rayleigh Line to the C-J point and then moves down the adiabat. Time is introduced directly to slow the burning and spread out the reaction zone. The only ZND input to hydrocodes is Ignition & Growth (I&G or "Reactive Flow"). It has been used mainly on LX-17, usually to model initiation experiments. Craig Tarver has been the keeper of the model and the theory behind it for the last decade.

We first consider the C-J Theory. Fig. 7-2 schematically shows the P-v plane. The Rayleigh Line is A'I, with the initial explosive at v = 1 at point I. In the conventional C-J detonation theory for an ideal explosive, the explosive is compressed up the Rayleigh Line to the C-J point at B. The gaseous products then expand down the adiabat BDF. At point D, where $v_B \sim 0.91$ for LX-17, the energy of compression has been used to compress the next section of explosive, and the energy of detonation, E_d, changes sign. The energy of detonation used to compress the next section of explosive is the area in the triangle, BDH. At larger volumes, the energy of detonation available externally (which totals E_o) is the area inside FDHI, where F and I extend on to the right.

Next, we turn to the ZND Theory. In Fig. 7-2, the LX-17 is driven up the Rayleigh Line to the von Neumann spike at point A'. Here, the energy of compression from the preceding slice of explosive compresses the slightly-burned but mostly solid LX-17 to about 43 GPa and 1800 K. The explosive continues to burn and falls down the Rayleigh Line to the I&G C-J point, A, at 26 to 27 GPa and perhaps 2500 K. At this point, the burn fraction, F, is 1. The products then expand down the adiabat ACE. The energy of compression in triangle ACG has been passed to the next zone of explosive by point C, which is at about $v_A \sim 0.93$ for LX-17. The energy of detonation available externally, E_o, lies in ECGI.

In ZND Theory, no energy of detonation is obtained as the explosive moves down the Rayleigh Line from the spike to the C-J point. The energy of compression is simply released to be passed to the next section of explosive. The C-J point in ZND Theory and I&G lies at a lower pressure than it does in pure C-J theory. The volume at which $E_d = 0$ is larger in I&G, i.e., $v_A > v_B$. The external energy of detonation, E_o, is the same in both. Thus, the adiabats must cross one another.

We now try to summarize the two approaches using the data of the preceding two chapters. For a near-ideal explosive hitting a metal of thickness equal to the explosive's reaction zone, we may list these pressures:

$$(P_k >) \; P_a \sim P_p \sim P_j > P_{cj} \qquad (4)$$

The spike pressure, P_k, is the highest, but the spike will not be seen in the jump-off of the metal plate. The pressure found from impedance-matching the plate shot, P_p, and the cylinder JWL, P_j, are essentially equal. In C-J Theory, one would equate these with the C-J pressure, P_{cj}. However, thermochemical codes give lower pressures so that the nonequilibrium adiabat pressure, P_a, is the inherent explosive property. We recall that the adiabat pressure is the point at which an infinite-size, steady-state (but not equilibrated) explosive leaves the Rayleigh Line and moves onto the Principal Adiabat. In I&G, the C-J point, a true thermodynamic equilibrium point, is probably never reached.

We next summarize the various detonation pressures obtained for five explosives in this report. We have these results, where the plus/minus values are precision:

	1-D Plate, P_p		Cylinder			
	Jump-off velocity	Supra-compress	Jump-off vel., P_p	3-point JWL Fit, P_j	Haselman compres-. sion, P_p	TIGER BKWR P_{cj}
LX-14	35 ± 2		37 ± 3	38 ± 2	36	35
PBX-9404	39 ± 2	38 ± 2	34 ± 5	38 ± 2	37 to 39	36
PETN	32 ± 4	31 ± 2	31* ± 3	32 ± 2		31
RX-26-AF		34 ± 2	36 ± 2	34 ± 2	32.5	32
LX-17	34	32 ± 2	32 ± 4	26 ± 1	30	27

(5)

The detonation pressures for the plate are those taken at the end of the reaction zone and represent the closest approach to C-J. The asterisk reminds us that PETN is set to 31 GPa for the cylinder jump-off, and the others are calculated from it.

For the first three explosives in Eq. (5), based on nearly ideal HMX and PETN, we see that the detonation and JWL pressures are in agreement. These would be called C-J pressures in C-J Theory, but the thermochemical codes always say that true equilibrium is 1 to 3 GPa lower. Our agreement breaks down for LX-17, where the jump-off and supracompression pressures are much higher than the JWL and calculated C-J pressures. We also recall that 26 GPa was consistent with a detonation pressure in the cylinder as obtained by comparing the percent of kinetic energy put into wall motion. We also note that the 34 and 26 GPa values found for LX-17 fit Tarver's values assigned to the spike and adiabat pressures, respectively, in the I&G model.

We now consider the data on the spike obtained from plates. The classic effect of plate thickness for LX-14 was seen in the previous chapter. The detonation pressures are determined by the impedance-match equation. There, thin plates showed a 44-GPa spike pressure, whereas at the 0.1-mm zone boundary, the pressure was about 36 GPa, in agreement with the other data.

The corresponding data for LX-17 are shown in Fig. 7-3 for copper and tantalum plates. The spike pressure is about 38 to 39 GPa and the near-C-J pressure at the zone boundary of 2 mm is 34 GPa. These numbers are higher than those obtained by I&G and by the efficiency and JWL fit in the cylinder. It appears that the impedance-matching pressure equation does not work for LX-17.

Hugoniot measurements on unreacted LX-17 have been made to 16 GPa, over halfway to the detonation point.[11] Tarver estimates from I&G that only a few percent have reacted at the spike. Hence, the initial shock delivered to a metal plate is by mostly solid LX-17 moving at 7.63 mm. The shock wave delivered to a metal wall is a thin-pulse spike.

We return to the impedance-match equation derived in the previous chapter. It is

$$P_m = P_p + \rho_o U_o (u_p - u_m), \tag{6}$$

where P_m is the pressure in the metal, P_p the pressure in the explosive, u_p the instantaneous particle velocity in the explosive, and u_m the particle velocity on the confined face of the metal. The LX-17 has not turned into gaseous products, so the Acoustic Approximation is literally true. All of Eq. (6) seems fine; the problem apparently arises with the relation

$$u_m = G u_{fs}, \tag{7}$$

where u_{fs} is the free surface particle velocity and G = 1/ 2 for a wide pressure pulse. We suggest that, for a projectile of solid LX-17, the pressure pulse is so thin the rarefaction wave degrades the velocity of the shock wave in the metal. Then, a smaller number is doubled at the unconfined face, and G > 1/ 2. The result would be to lower the detonation pressure calculated by the impedance-match equation.

3. The Ignition and Growth Model

We shall now briefly describe the I&G model created by Cochran and Chan.[12] It uses three sets of equations: a solid explosive EOS, a reaction products EOS, and a set of burn rate commands. A. Nichols notes that the JWLs are the EOSs, and the rate equations are hydrocode pulse-shaping commands—no different from program or beta-burn. However, the kinetic behavior is so deeply imbedded in the model that the entire package soon becomes considered an EOS.

We recall that the EOS usually used is the JWL, in which the pressure adiabat is

$$P_s(v) = Aexp(-R_1v) + Bexp(-R_2v) + Cv^{-(1+\omega)}. \quad (8)$$

In the I&G model, the EOS is called the Gruneison form of the JWL, and it is

$$P_s(v) = R_1exp(-R_5v) + R_2exp(-R_6v) + R_3T/v, \quad (9)$$

where the terminology used in the new DYNA2D manual will be used throughout.[13] Eq. (8) is not the same as Eq. (9). The third term in this EOS is simply replaced by a different kind of function. Because of this, any fitting routine will likely produce a different set of R_i in place of A and B.

All other codes have only the product EOS, but I&G has two: the explosive (reactant) EOS,

$$P_{se}(v) = R_{1e}exp(-R_{5e}v) + R_{2e}exp(-R_{6e}v) + R_{3e}T/v, \quad (10)$$

and the product EOS,

$$P_{sp}(v) = R_{1p}exp(-R_{5p}v) + R_{2p}exp(-R_{6p}v) + R_{3p}T/v. \quad (11)$$

The EOSs are identical in structure. However, the explosive EOS is a Hugoniot, and the product EOS is an adiabat used as a Hugoniot above the adiabat point. The intent is to blend them while the explosive burns between the spike and adiabat points.

The constant R_3 may be written

$$R_3 = \omega c_v, \quad (12)$$

where c_v is a constant with the appearance of a heat capacity at constant volume.

The fraction of explosive reacted in each element is F, which starts at perhaps 0.03 to 0.06 and ends fully burned at 1. The burning rate is

$$\partial F/\partial t = \partial F/\partial t|_1 + \partial F/\partial t|_2 + \partial F/\partial t|_3. \quad (13)$$

where the burning process moves through terms 1, 2, and 3 in order.

The initiation term is

$$\partial F/\partial t|_1 = F_q (1-F)^{F_r} \left[\frac{1}{v_e} - 1 - C_{crit} \right]^{\eta}, \quad (14)$$

where v_e is the relative volume of the solid explosive and F_q, F_r, C_{crit}, and η are constants. This term is needed to start an explosive burn with a low-level trigger such that initiation may fail or take some time to get started. It probably is not needed in detonation caused by a detonator, but it can be used to turn on the detonation faster than can be done with a program burn.

The G_1 growth term in DYNA2D is the only such term when two terms (the other being initiation) are used. When three terms are used, it is the fast-growth kinetics term. This term is

$$\partial F/\partial t\,|_2 = G_1\,(1-F)^{s_1}\,F^{a_1}\,P_s^m, \tag{15}$$

where G_1, s_1, and a_1 are constants. One might expect the rate to go only as a function of $(1-F)$. C. Tarver says that the $(1-F)F$ form is included to bring the rate in the code gently to zero as $F \longrightarrow 1$.

It is the G_1 growth term, with its pressure dependence, that creates the curved detonation front in a cylinder. The rarefaction wave at the cylinder wall lowers the pressure in the adjacent explosive. This turns down the reaction rate during initiation so that the explosive at the walls burns more slowly. For a slow initiation, the calculated curvature is very large and obvious. As it approaches steady state, the detonation front tries to straighten out. At steady state, the curvature is much more gentle.

The G_2 growth term represents slow kinetics when three terms are used. It is not included for the two-term model. It is

$$\partial F/\partial t\,|_3 = G_2\,(1-F)^{s_2}\,F^{a_2}\,P_s^n, \tag{16}$$

where G_2, s_2, and a_2 are constants. Because this term is always dropped in the two-term model, confusion with the G_1 coefficients can easily result.

Originally, the second growth term was added as a fast-growth term to describe thin-pulse initiation. Therefore, the G_1 term is slow for the two-term description of LX-17, but the G_2 term is slow for the three-term model. This is locked in by the limits set on F for the various terms. Looking across a table of I&G constants does not allow easy comparison.

By the time the second growth term is done, $F = 1$ and the adiabat point is reached for an infinite diameter explosive. For a smaller charge, the adiabat point is never reached, and the adiabat starts from a sonic point. The adiabat point is not equated with the C-J point because we cannot be sure that this point really is at thermodynamic equilibrium.

Table 7-2 lists the I&G constants found for all explosives run with I&G at LLNL.[14–26] For convenience, we list some of the compositions in wt % and with names. Comp B is RDX 63, TNT 36, and wax 1. H-6 is RDX 45, TNT 30,

Al 20, wax 5, and $CaCl_2$ 0.5. LX-10 is HMX 90 and Viton A 5. Propellant B is AP 88 and HMX 12. RX-03-BB is the experimental ancestor of LX-17. RX-25-BF is HMX 38.4, AP 35.5, ZrH_2 22.1, and estane 4.0. RX-35-BH has the same components, but with values of 19.3, 47.1, 29.8, and 3.8. RX-26-AF is TATB 46.6, HMX 49.3, and estane 4.1. RX-HD, an ANFO explosive, is 78.65, water 9.45, calcium nitrate 5.52, fuel 6.38, and plastic microballoons 0.08.

For the PETN/Al and TNT/Al explosives, we list wt%, names with 5-μm aluminum, and names with 18-μm aluminum. For PETN/Al, they are 95/5 RX-40-AI, RX-40-AF; 90/10 RX-40-AJ, RX-40-AG; 80/20 RX-40-AK, and RX-40-AH. For TNT/AL, we have 95/5 RX-40-CI, RX-40-CF and 90/10 RX-40-CJ and RX-40-CG.

Most I&G runs are for initiation, but a few are for the overdriven or supracompressed explosive; LX-17 has a set for both. In the ignition model, where the detonation pressure starts below 26 GPa, the three terms, in order, describe (1) hot-spot creation, (2) hot-spot spreading, and (3) hot-spot coalescing. The supracompression model, for detonation pressures greater than 26 GPa, has the three terms refer to (1) ignition, (2) the main explosive reaction to product gases, and (3) precipitation of carbon. For the third term, Tarver has set the exponent equal to 1, so we have

$$\partial F/\partial t\,|_3 = G_2(1-F)FP_s, \tag{17}$$

which looks more like traditional kinetics with a pressure to the first power.

One possibility is that carbon condensation occurs after the sonic point. If it does, I&G cannot properly describe it. Tarver, however, notes the work of Kolomiichuk and Mal'kov on ultradispersed diamond as seen by x-ray diffraction in the final debris of PETN, TNT, and other explosives.[27] These authors varied the diameter of their charges by a factor of 10 and the mass by a factor of 40 but saw no appreciable change in the size of the diamond distributions. Because only the reaction zone width is invariant to sample size, the authors concluded that all diamond condensation occurs in the reaction zone, i.e., before the adiabat point.

We return to the listing of the I&G constants. These constants are used according to these rules:

$$\partial F/\partial F\,|_1 \longrightarrow 0 \text{ when } F \geq F_{max,ig}, \tag{18}$$

$$\partial F/\partial F\,|_2 \longrightarrow 0 \text{ when } F \geq F_{max,gr}, \tag{19}$$

$$\partial F/\partial F\,|_3 \longrightarrow 0 \text{ when } F \leq F_{min,gr}. \tag{20}$$

$F_{max,ig}$ and $F_{min,gr}$ set the upper limits of the terms. In the 1985 version, both terms 1 and 2 can run to F = 0.5, but Tarver says that the first term rarely

turns on more than about 0.03. In the 1989 version, the first term is limited to 0.0232 while the second term runs on to 0.85. The third term takes over from the second and may or may not run all the way to 1.00.

The I&G model can also model slow-reacting aluminized explosives. The fast-growth term now becomes the total descriptor for the base explosive, and the slow-growth term describes the reaction of its products with the aluminum. In DYNA2D, two EOSs are now used, although C. Tarver has used up to five in the past. A. Nichols has recently introduced a three-EOS model into CALE. It has two temperature-dependent product JWLs—one for the main explosive and the other for the aluminized products. The first EOS is used with the fast-growth term and the second EOS with the slow-growth term. The fast-explosive EOS was created from CHEQ and represents the C, H, N, and O gaseous products of the explosive itself. The slow aluminized EOS was created from TIGER BKWR, which is, at present, the only code that includes gaseous aluminum compounds. This EOS has the solid product Al_2O_3, plus what is left from the reaction with the second EOS gases. A three-term EOS can also be considered for the carbon coagulation problem. The second EOS would be identical to the C, H, N, O gas EOS above, and the third EOS contains solid carbon plus gas.

The idea of simplifying I&G to freshen it up has recently become popular. M. Murphy et al. have taken out the fast-growth term and returned to the original two-term formulation, which is useful for certain problems.[19] They also realized that a major drawback was the lack of physical reality in the constants, which they tried to relate to measurable quantities. They related the exponent n in the slow growth term to the slope of the run distance-to-detonation (Pop) plots. This slope, $\Delta \ln x / \Delta \ln P$, is about 3.5 mm/GPa for LX-17 and about 1.5 mm/GPa for PBX-9404 and Comp B. They suggested that these numbers be related to the exponents 3 and 2, respectively, in the I&G model.

Murphy et al. estimated the amplitude of the slow-growth term, G_2 (in μs^{-1}) for Weapons Grade Comp B as

$$G_2 \sim 1800/D_f \text{ for } 4.4 < D_f < 7.2 \text{ mm}, \qquad (21)$$

where D_f is the failure diameter. For Comp B, one expects the slow growth term to represent carbon coagulation, so this effect presumably is the key to nonideality in this case.

Harold Zimmerman has suggested some additions for the next-stage I&G model. The current model assumes that the reactant and the products are at the same temperature. This, in turn, requires small zoning in order to imagine a real volume where this might be so. In fact, it is doubtful that temperature equilibrium exists even in a small volume. Zimmerman wants to go to larger zones, in which reactant and products will be tracked separately in each element for volume, pressure, and artificial viscosity, Q. This approach

leads to separate temperatures. His hope is that all the parameters can be kept track of "subzonally," thereby allowing the use of larger zones. Again, the reactant and products will be described by the temperature-dependent JWLs, and the C-term will be temperature-dependent.

4. Inner Workings of I&G

The only detailed discussion of the I&G model has been given by Cochran and Chan.[12] They describe two versions of the model with significant differences when only part of the explosive is burned. The first and more physical model is used in DYNA2D. Here, there is pressure equilibration between the reactant and products. The equations are

$$P(v, T, F) = P_e(v_e, T) = P_r(v_r, T), \tag{22}$$

$$E = (1-F)E_{se}(v_e, T) + FE_{sr}(v_r, T) - \text{constant}, \tag{23}$$

$$v = (1-F)v_e + Fv_p. \tag{24}$$

Many of the code iterations involve a variable β, which is called a real volume fraction occupied by the specific material.[12] The volume relations are:

$$v_e = \beta v/(1-F). \tag{25}$$

$$v_p = (1-\beta)v/F. \tag{26}$$

$$v = v_e v_p/[v_p\beta + v_e(1-\beta)]. \tag{27}$$

This method required considerable reiteration to get the pressures and was considered too slow. A second and less physical method was devised and used in KOVEC and HEMP. The pressures and energies were split into mechanical (function of volume only) and thermal parts (volume and temperature). This is the form of the temperature-dependent JWLs listed above, where the R_1 and R_2 terms are mechanical and the R_3 term is thermal. The mechanical pressure, P_m, and the energy, E_m, are related by

$$\partial E_m / \partial v = -P_m. \tag{28}$$

The pressure then becomes

$$P(v, T, F) = (1-F)P_e(v, T) + FP_r(v, T). \tag{29}$$

We are now using the concept of partial pressures with no need to keep track of separate volumes; also,

$$E = (1 - F)E_s(v, T) + FE_{s(}v, T) - \text{ constant.} \quad (30)$$

In both models, there is no apparent requirement of temperature equilibrium between the two parts. A total thermal energy, E_t, is calculated and an overall temperature computed using

$$T = (E_t + Q) / c_v, \quad (31)$$

where Q is the artificial viscosity. D. Sharp has noted that one of the functions of Q is to add entropy to a model that doesn't otherwise have it. Eq. (31) shows how the entropy of the shock translates into additional temperature.

5. Results from the I&G Model

Fig. 7-4 shows the curvature of the steady-state detonation front in LX-17 using the two-term I&G model in DYNA2D. The cylinder was 12 cm long and 50 mm in diameter with 13,920 zones—12,000 of them in the explosive. The explosive was 50 elements wide (0.16 mm/zone) compared to 12 in the standard cylinder model. A merged explosive-wall configuration was used. A programmed burn was used to start the burn before it switched to I&G. This is a coarse-zoned run, but it took about 5 times as long as a programmed burn of the same zoning. Cycle times were 25 to 30 μs as compared with 5 to 6 with a programmed burn, and zone-tangling was pronounced.

The curvature in Fig. 7-4 agrees with the data in Fig. 7-1, although it does not appear to do so because Fig. 7-1 magnifies the lag in the detonation front, whereas Fig. 7-4 has the same magnification throughout. We see that the curvature is really not very great for LX-17. The calculated maximum pressure in the center of the cylinder is 30 GPa, which drops to 24 GPa at the wall.

We may compare the 0.16- × 0.16-mm/explosive zone sizing in the I&G model with the 0.05- × 1-mm/zone size used by John Walton in HEMP to describe the standard PETN JWL in Chapter 3. The I&G zoning is a factor of four greater in number of zones. Moreover, the HEMP zoning used to get the oscillations right in the metal far exceeds anything used in the I&G model.

LX-17 was modeled in HEMP using the 1985 three-term model by Aldis, Quirk, and Breithaupt.[28] They report good agreement for LX-17 in copper cylinders but some deviation in the single tantalum shot. L. Haselman's view of the HEMP runs was that the energy was low even with I&G. Tarver states that the constant R_{3p} term is the reason for this. An average heat capacity of the detonation products is used to cover 2000 K, and any changes in the

experimental details can affect this term by 5%. The constant R_{3p} was developed from copper cylinders and should be changed for tantalum. We note that the 1985 JWL was based on the cylinder JWL, which was also low in energy. Finally, we have noted above that the I&G models are different in HEMP and DYNA, so that Tarver and Aldis could have gotten different results with the same EOS.

6. Estimating the Reactant and Product JWLs

We next consider the estimating of temperature-dependent JWLs. For the unreacted explosive, Tarver often uses the rule of thumb

$$R_{5e} \sim 10R_{6e}. \tag{32}$$

At v = 1 and zero pressure, another constraint appears as

$$R_{1e}\exp(-R_{5e}) + R_{2e}\exp(-R_6)e + R_{3e}T_o \simeq 0, \tag{33}$$

where T_o is 298 K. The constant $c_v = R_{3e} / \omega$ is not a real heat capacity taken from the thermodynamic literature but is a constant of the fit.

The derivation of the product EOS is more critical. The simplest way to connect this with the temperature-dependent JWL is to define the temperature function

$$T(v) = M / v^n, \tag{34}$$

which we substitute into the temperature-dependent JWL. At the detonation point of the JWL, we have

$$dP_j / dv_j = -\rho_o D^2 = -R_{1p}R_{5p}\exp(-R_{5p}v_j) - R_{2p}R_{6p}\exp(-R_{6p}v_j) - (n + 1)R_{3p}M / v_j^{n+2}, \tag{35}$$

$$P_j = R_{1p}\exp(-R_{5p}v_j) + R_{2p}\exp(-R_{6p}v_j) + R_{3p}M / v_j^{n+1}, \tag{36}$$

$$E_s(j) = (R_{1p}/R_{5p})\exp(-R_{5p}v_j) + (R_{2p}/R_{6p})\exp(-R_{6p}v_j) + R_{3p}M / nv_j^n. \tag{37}$$

These are the same equations as those of the regular JWL, where

$$C \longleftrightarrow R_{3p}M, \tag{38}$$

and

$$\omega \longleftrightarrow n. \tag{39}$$

This equality is the result of the temperature fit and not the result of mathematical equality. As an example, for 1.763 g/cc PETN we obtain for the detonation point and volumes of 1.87, 2.2, 4.1, and 6.5 the calculated temperatures of 3338, 1798, 1630, 1181, and 968 K, respectively. This can be fit to

$$T = 2684 / v^{0.573}, \tag{40}$$

so that M = 2684 and n = 0.573. The latter is accidentally close to the 0.57 for ω in the regular JWL. Leaving n as 0.57, we have

$$R_{3p} = C / M = 0.0372735 / 2684 = 1.389\ e{-}5. \tag{41}$$

This allows the quick creation of the temperature-dependent JWL, here with identical A and B terms. If n had been different, A and B would have changed somewhat. It is important to remember that the temperature calibration is unknown and uncertain both in TIGER and in the hydrocode where the JWL will be used. Hence, the use of the new JWL will be empirically judged by the hydrocode results for that problem.

7. Changes for a Future Production Model

The present I&G model depends on the symmetry of its JWLs and cannot easily be changed. Also, there will always be a need for a full-scale scientific version of I&G. However, there is a real and immediate need for a faster, less complicated production version of I&G. The following ideas might be considered.

- Use of the partial pressure mixing rule for computational speed.
- Explicit use of the detonation velocity, with linking to the corner-turning models. The detonation velocity, as a function of distance from the initiator, would be used as an advanced kind of programmed burn.
- Use of a nontemperature-dependent product EOS, with the regular JWL being the most obvious.
- Use of a U_s-u_p EOS for the unreacted explosive.

We may further consider the unreacted EOS. One drawback of the JWL form, as M. Murphy et al. have noted,[23] is that real data don't come in this format. They come as the constants C_o and S_1 in the equation

$$U_s = C_o + S_1 u_p. \tag{42}$$

From mass conservation comes,

$$u_p = U_s (1 - v), \tag{43}$$

and from mass and momentum conservation

$$P = \rho_o U_s u_p. \tag{44}$$

We substitute Eq. (42) into Eq. (43), eliminate u_p, and solve for U_s to get

$$U_s = \frac{C_o}{S_1(v - 1) + 1}. \tag{45}$$

We substitute Eqs. (42), (43), and (45) into Eq. (44) to obtain the U_s-u_p EOS

$$P_e = \rho_o C_o^2 \frac{1 - v}{[S_1(v - 1) + 1]^2}. \tag{46}$$

This is the Hugoniot of the unreacted explosive.

Eq. (46) runs upward in pressure until it intersects the Rayleigh Line, defined by

$$P = \rho_o D^2 (1 - v). \tag{47}$$

We eliminate pressure between Eqs. (45) and (47) to obtain the spike volume

$$v_k = \frac{1}{S_1}\left(\frac{C_o}{D} - 1\right) + 1. \tag{48}$$

The spike pressure is then calculated from Eq. (47).

$$P_k = \rho_o D^2 (1 - v_k). \tag{49}$$

The two EOSs may be compared for LX-17. We calculate below the Spike pressure and the v = 1 pressure using both the temperature-dependent JWL but also the older regular JWL. A temperature of 1800 K at the Spike point was obtained from C. Tarver and used in the calculation. For LX-17, C_o = 2.74 mm/μs and S_1 = 2.6 mm/μs.[29] We get these results:

	Volume	Pressure (GPa)
Regular JWL	0.676	35.5
	1.00	2.3
T-dependent JWL	0.695	33.5
	1.00	0.7
U_s-u_p	0.701	33.2
	1.00	0.0

(50)

We see that neither JWL is near zero pressure for v = 1. However, the form of the U_s-u_p EOS forces it to be zero for the initial state of the explosive. It is, in effect, a specialized EOS that runs from v = 1 to compressed states.

Mike Murphy has suggested that the U_s-u_p EOS be used in the codes so that more convenient input can be used.[23] This EOS usually appears with the substitution

$$\mu = \frac{1}{v} - 1 = \frac{\rho}{\rho_o} - 1. \tag{51}$$

Then, Eq. (51) becomes

$$P_e = \frac{\rho_o \mu (1+\mu) C_o^2}{[1-(S_1-1)\mu]^2}. \tag{52}$$

Another form is derived from the Gruneison EOS form of

$$P_e = \gamma_o E_e / v + f(v), \tag{53}$$

where γ_o is a constant (the Gruneison gamma, equal to $v\partial P/\partial E$) and E_e is the total energy. Eq. (52) is substituted into Eq. (53), which is solved for f(v). This is put back into Eq. (53) to obtain

$$P_e = \frac{\rho_o \mu (1+\mu) C_o^2}{[1-(S_1-1)\mu]^2}\left(1 - \frac{\gamma_o}{v}\mu\right) + \frac{\gamma_o}{v}E_e. \qquad (54)$$

This is the energy form, and it is comparable to the pressure-energy form of the JWL in Chapter 2, Eq. (15). It is not comparable to the temperature-dependent JWL, in which $c_v T$ is a thermal energy, not a total energy. A disadvantage of Eq. (54) is that another constant needs to be known.

Eqs. (51) and (52) constitute the simplest unreacted explosive EOS given that only C_o and S_1 are available. A major problem is that the U_s-u_p data may not be very good. Sometimes the fit is so bad that C_o is just a constant and does not equal the speed of sound. At the moment, finding decent two-constant data appears more difficult than adding a third constant, S_2. Also, measured unreacted data and even a measured detonation velocity may not be available. In this case, one can calculate the C-J pressure and volume and the detonation velocity from TIGER. Then, add 2 GPa to the C-J pressure to approximate the adiabat pressure and calculate the detonation volume on the Rayleigh Line. Then, as a rough summary suggested by C. Tarver, use the relation

$$P_k / P_j \sim 1.25. \qquad (55)$$

The volume ratio, v_k / v_j will be about 0.94.

8. References

1. B. M. Dobratz and P. C. Crawford, *LLNL Explosives Handbook,* Lawrence Livermore National Laboratory, Livermore, CA, UCRL-52997 (1985), pp. 8–32.

2. A. W. Campbell and R. Engelke, "The Diameter Effect in High-Density Heterogeneous Explosives," *Proceedings Sixth Symposium (international) on Detonation,* Coronado, CA, August 24–27, 1976, p. 642.

3. A. W. Campbell, *Propellants, Explosives, Pyrotechnics* **9,** 183 (1984).

4. J. B. Bdzil, Los Alamos National Laboratory, Los Alamos, NM, 87545, private communication, 1993.

5. B. D. Lambourn and D. C. Swift, "Application of Whitham's Shock Dynamics Theory to the Propagation of Divergent Detonation Waves," *Proceedings Ninth Symposium (International) on Detonation,* Portland, OR, August 28–September 1, 1989, pp. 784–797.

6. D. C. Swift, AWE, Aldermaston, England, private communication, 1993.

7. J. B. Bdzil, *J. Fluid Mech.* **108,** 195 (1981).

8. D. S. Stewart and J. B. Bdzil, "Examples of Detonation Shock Dynamics for Detonation Wave Spread Applications," *Proceedings Ninth Symposium (International) on Detonation,* Portland, OR, August 28–September 1, 1989, pp. 773–783.

9. J. Bdzil and W. Fickett, *DSD Technology: A Detonation Reactive Huygens Code,* Los Alamos National Laboratory, Los Alamos, NM, LA-12235-MS (1992).

10. L. M. Hull, "Mach Reflection of Spherical Detonation Waves," Tenth International Detonation Symposium, Boston, MA, July 12–16, 1993, Paper Summaries, p. 87.

11. R. K. Jackson, L. G. Green, R. H. Bartlett, W. W. Hofer, P. E. Kramer, R. S. Lee, E. J. Nidick, Jr., L. L. Shaw, and R. C. Weingart, "Initiation and Detonation Characteristics of TATB," *Proceedings Sixth Symposium (International) on Detonation,* Coronado, CA, August 24–27, 1976, p. 755.

12. S. G. Cochran and J. Chan, *Shock Initiation and Detonation Models in One and Two Dimensions,* Lawrence Livermore National Laboratory, Livermore, CA, UCID-18024 (1979).

13. R. G. Whirley and B. E. Engelmann, *DYNA2D A Nonlinear Explicit, Two-Dimensional Finite Element Code for Solid Mechanics—User Manual,* J. O. Hallquist, originator (April, 1992), pp. 121–125.

14. E. L. Lee and C. M. Tarver, *Phys. Fluids* **23,** 2362 (1980).

15. C. M. Tarver and J. O. Hallquist, "Modeling Two-Dimensional Shock Initiation and Detonation Wave Phenomena in PBX 9404 and LX-17," *Proceedings Seventh Symposium (International) on Detonation,* Annapolis, MD, June 16–19, 1981, pp. 488–497.

16. C. M. Tarver, L. M. Erickson, and N. L. Parker, "Shock Initiation, Detonation Wave Propagation and Metal Acceleration Measurements and Calculations for RX-26-AF," *Shock Waves in Condensed Matter,* American Physical Society, Santa Fe, NM, July 18–21, 1983, pp. 609–612.

17. C. M. Tarver, J. O. Hallquist, and L. M. Erickson, "Modeling Short Pulse Duration of Solid Explosives," *Proceedings Eighth Symposium (International) on Detonation,* Albuquerque, NM, July 15–19, 1985, pp. 951–961.

18. P. A. Urtiew, L. M. Erickson, D. F. Aldis, and C. M. Tarver, "Shock Initiation of LX-17 as a Function of its Initial Temperature," *Proceedings Ninth Symposium (International) on Detonation,* Portland, OR, August 28–September 1, 1989, pp. 112–122.

19. M. J. Murphy, R. L. Simpson, R. D. Breithaupt, and C. M. Tarver, "Reactive Flow Measurements and Calculations for ZrH_2-Based Composite Explosives," *Proceedings Ninth Symposium (International) on Detonation,* Portland, OR, August 28–September 1, 1989, pp. 525–534.

20. L. G. Green, C. M. Tarver, and D. J. Erskine, "Reaction Zone Structure in Supracompressed Detonating Explosives," *Proceedings Ninth Symposium (International) on Detonation,* Portland, OR, August 28–September 1, 1989, pp. 670–682.

21. C. M. Tarver and L. G. Green, "Using Small Scale Tests to Estimate the Failure Diameter of a Propellant," *Proceedings Ninth Symposium (International) on Detonation,* Portland, OR, August 28–September 1, 1989, pp. 701–710.

22. W. C. Tao, C. M. Tarver, D. L. Ornellas, C. Lee, T. Cook, and J. Kury, "Understanding Composite Explosive Energetics: IV. Reactive Flow Modeling of Aluminum Reaction Kinetics in PETN and TNT using Normalized Product Equation of State," *Tenth International Detonation Symposium,* Boston, MA, July 12–16, 1993, Paper Summaries, pp. 52–54.

23. M. J. Murphy, E. L. Lee, A. M. Weston, and A. E. Williams, "Modeling Shock Initiation in Composition B," *Tenth International Detonation Symposium,* Boston, MA, July 12–16, 1993, Paper Summaries, p. 181.

24. P. A. Urtiew, T. M. Cook, J. L. Maienschein, and C. M. Tarver, "Shock Sensitivity of IHE at Elevated Temperatures," *Tenth International Detonation Symposium,* Boston, MA, July 12–16, 1993, Paper Summaries, Ppp. 528–530.

25. C. M. Tarver, P. A. Urtiew, S. K. Chidester, and L. G. Green, *Propellants, Explosives & Pyrotechnics* **18,** 117 (1993).

26. Craig Tarver, LLNL, unpublished data kindly provided for this report, 1994.

27. V. N. Kolomiichuk and I. Yu. Mal'kov, *Combustion, Explosions & Shock Waves* **29,** 113 (1993).

28. D. F. Aldis, W. Quirk and R. D. Breithaupt, *The Effect of Detonation Curvature on Cylindrical Wall Motion,* Lawrence Livermore National Laboratory, Livermore, CA, UCRL-ID-107480 (1991).

29. B. M. Dobratz and P. C. Crawford, *LLNL Explosives Handbook,* Lawrence Livermore National Laboratory, Livermore, CA, UCRL-52997, Change 2, January 31, 1985, p. 7–33.

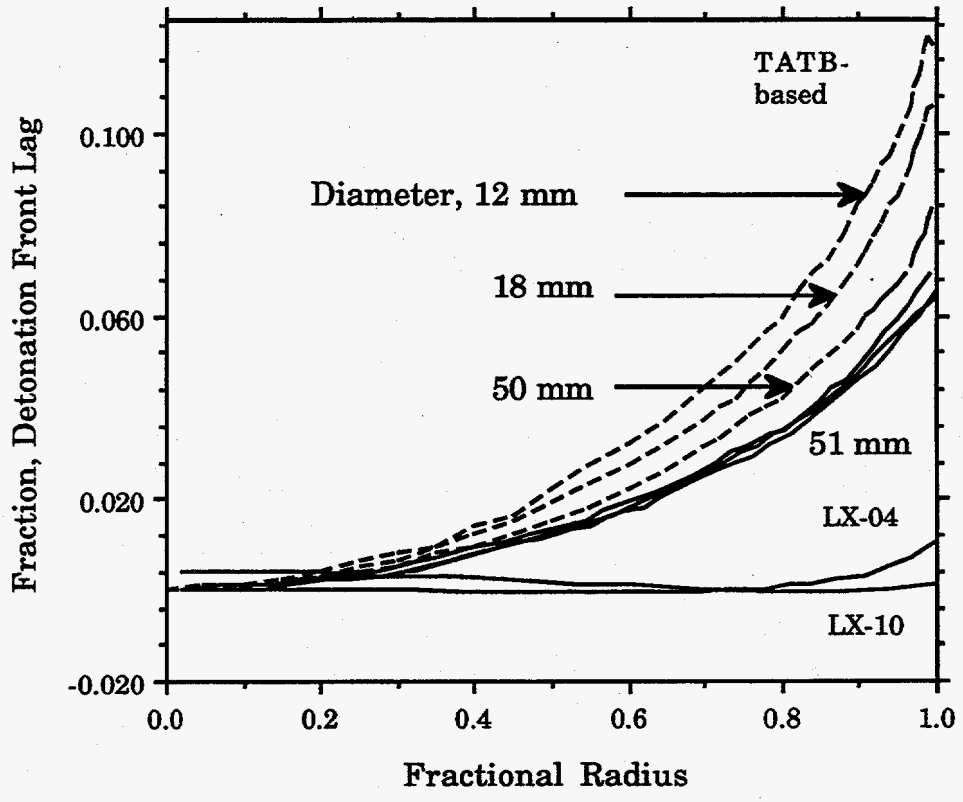

Fig. 7-1. Detonation front curvature as measured end-on in cylinder shots. The X-axis is the fractional radius—equal to 0 at the cylinder center and 1 at the edge. The Y-axis is the lag of the detonation front relative to the radius. The Y-axis is expanded and greatly magnifies the curvature effect. The HMX explosives show no curvature except near the wall, but the TATB explosives are all curved across their radii. A set of three unconfined LANL TATB shots shows increasing curvature with decreasing actual cylinder diameter.

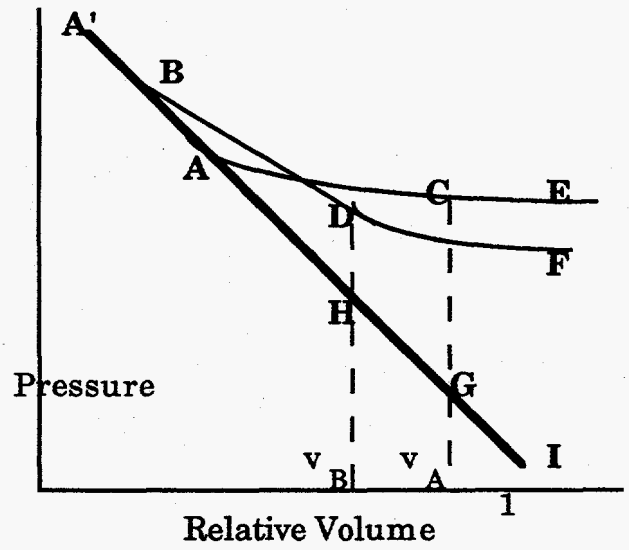

Fig. 7-2. Schematic of the pressure-relative plane for the EOS models. The Rayleigh Line is A'I, with the initial v = 1 solid explosive point at I. For an ideal explosive in C-J theory, the C-J point is B, the energy of compression is the area of the triangle BDH, and the energy of detonation, E_0, is the area FDHI. For the nonideal explosive in the I&G model and ZND theory, the spike point is A' and the C-J point A. The energy of compression is ACG, and the energy of detonation, E_0, is ECGI. The pure-CJ adiabat, BDF, crosses the I&G adiabat, ACE. The two energies, E_0, are the same. Points E and F are supposed to be far out at 1 atmosphere.

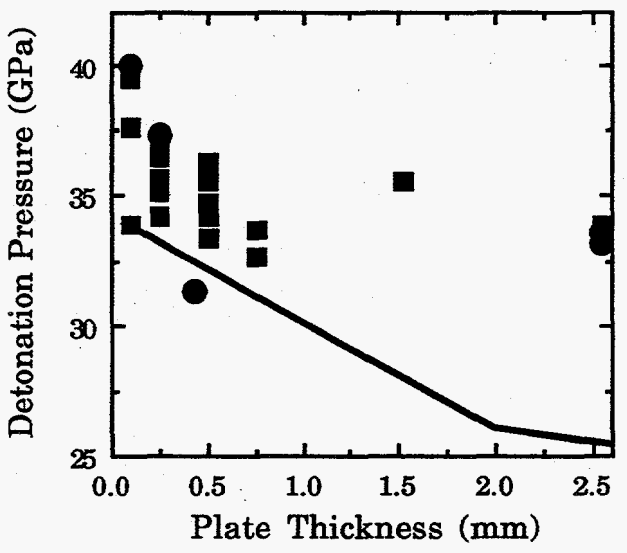

Fig. 7-3. Detonation pressure, as calculated from impedance matching, for metal plates pushed by LX-17, which has a reaction zone of about 2 mm. The line is Tarver's I&G view of LX-17, which is generally supported by the Cylinder Test. The discrepancy in the data is considered from the point of view of the failure of the impedance-matching equation. The data are LX-17 on Ta (solid squares) and Cu (solid circles).

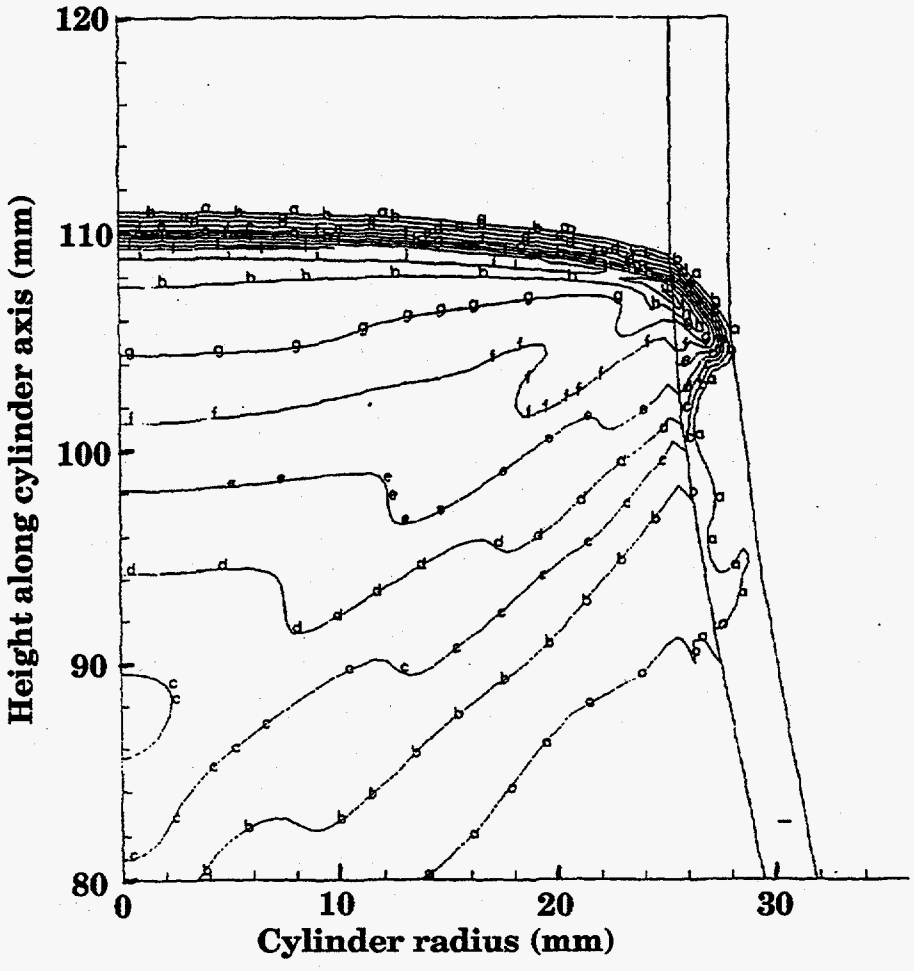

Pressure (GPa)			
a = 0.0500	d = 0.132	g = 0.214	j = 0.295
b = 0.0773	e = 0.159	h = 0.241	k = 0.323
c = 0.105	f = 0.186	i = 0.268	l = 0.350

Fig. 7-4. Detonation front for LX-17 as calculated in DYNA2D using the two-term parameters of Table 3. The curvature corresponds to that shown in Fig. 7-1, although the unmagnified scale shown here shows that the curvature is not great. The maximum pressure is 30 GPa in the center of the cylinder and 24 GPa at the wall.

Table 7-1. Detonation front data for three TATB-based explosives and two HMX-based explosives. The RX-52 data are by far the best. All cylinders are 51 mm in diameter. The length listed below is that of the measurement slit, unfortunately off-center from the diameter in three cases. The headings are: A ratio of radius (edge = 1); B detonation front lag (mm); and C ratio detonation lag to radius.

Cyl #584, RX-52-AD 50.8 mm diameter			Cyl#585, RX-52-AE 50.8 mm diameter			Cyl #556, LX-17 46.7 mm diameter			Cyl #557, LX-04 46.2 mm diameter		
A	B	C	A	B	C	A	B	C	A	B	C
-1.00	1.72	0.068	-0.99	1.71	0.067	-1.00	1.78	0.070	-1.00	0.30	0.012
-0.97	1.57	0.062	-0.97	1.55	0.061	-0.98	1.69	0.067	-0.98	0.24	0.010
-0.95	1.43	0.056	-0.94	1.37	0.054	-0.96	1.60	0.063	-0.95	0.19	0.007
-0.91	1.28	0.051	-0.91	1.23	0.048	-0.93	1.46	0.057	-0.89	0.13	0.005
-0.87	1.14	0.045	-0.89	1.13	0.044	-0.90	1.33	0.052	-0.82	0.06	0.003
-0.82	0.99	0.039	-0.85	0.98	0.038	-0.86	1.17	0.046	-0.76	0.04	0.001
-0.77	0.85	0.034	-0.80	0.86	0.034	-0.81	1.03	0.040	-0.24	-0.01	0.000
-0.70	0.70	0.028	-0.76	0.74	0.029	-0.76	0.88	0.035	-0.02	-0.01	0.000
-0.64	0.58	0.023	-0.68	0.59	0.023	-0.70	0.74	0.029	0.25	-0.01	0.000
-0.56	0.46	0.018	-0.59	0.43	0.017	-0.62	0.57	0.022	0.78	0.01	0.000
-0.44	0.32	0.012	-0.51	0.29	0.012	-0.55	0.43	0.017	0.84	0.03	0.001
-0.31	0.18	0.007	-0.37	0.16	0.006	-0.45	0.30	0.012	0.87	0.05	0.002
-0.18	0.09	0.004	-0.24	0.06	0.002	-0.34	0.17	0.007	0.91	0.09	0.003
-0.05	0.04	0.002	-0.08	0.00	0.000	-0.22	0.07	0.003	0.94	0.12	0.005
0.09	0.01	0.000	0.11	0.02	0.001	-0.02	0.00	0.000	0.97	0.18	0.007
0.20	0.06	0.002	0.22	0.07	0.003	0.13	0.01	0.000	0.99	0.23	0.009
0.34	0.14	0.005	0.33	0.16	0.006	0.31	0.10	0.004	1.00	0.26	0.010
0.46	0.25	0.010	0.47	0.29	0.012	0.46	0.25	0.010	Cylinder #558, LX-10 76.8 mm diameter		
0.58	0.39	0.016	0.57	0.43	0.017	0.58	0.41	0.016			
0.67	0.56	0.022	0.65	0.56	0.022	0.64	0.53	0.021	A	B	C
0.74	0.70	0.028	0.72	0.71	0.028	0.71	0.66	0.026	-1.00	0.03	0.001
0.81	0.88	0.034	0.79	0.85	0.034	0.77	0.79	0.031	-0.77	0.01	0.000
0.86	1.02	0.040	0.83	0.96	0.038	0.82	0.95	0.037	-0.51	0.08	0.002
0.88	1.08	0.043	0.86	1.11	0.044	0.86	1.07	0.042	-0.22	0.13	0.005
0.92	1.24	0.049	0.91	1.28	0.050	0.90	1.19	0.047	0.09	0.14	0.005
0.96	1.41	0.056	0.93	1.42	0.056	0.93	1.34	0.053	0.33	0.10	0.005
0.98	1.52	0.060	0.96	1.58	0.062	0.97	1.50	0.059	0.55	0.04	0.003
1.00	1.66	0.065	0.98	1.66	0.065	0.99	1.58	0.062	0.74	-0.01	0.002
			0.99	1.74	0.069	1.00	1.65	0.065	1.00	0.06	0.000

Table 7-2. List of all LLNL-derived I&G parameters used in DYN2D. A blank space means zero. A list of compositions is given in the text. For the PETN- and TNT-aluminized explosives, two values of G_2 are given. The first is for 5-μm aluminum and the second for 18-μm aluminum. All units are in Mbars except for detonation velocity, which is in mm/μs.

					COMP B	H-6	LX-10
	DYNA2D manual	Tarver's terms	COMP B (LANL) initiation	COMP B (Military) initiation	Three-term initiation	Three-term initiation	Three-term initiation
Unreacted explosive JWL	density (g/cc)	ρ_o	1.712	1.630	1.712	1.76	1.865
	R_{1e} (Mbars)	A	778.1	1479	778.1	152.7	9522
	R_{2e} (Mbars)	B	-0.05031	-0.05261	-0.05031	-0.05175	-0.05944
	R_{3e} (Mbar/K)		2.22E-05	2.27E-05	2.22E-05	2.88E-05	2.47E-05
	R_{5e}	R_1	11.3	12	11.3	9.5	14.1
	R_{6e}	R_2	1.13	1.2	1.13	0.95	1.41
	ω_e	ω	0.8938	0.912	0.8938	0.976	0.8867
	c_{ve}	C_v	2.487E-05	2.487E-05	2.487E-05	2.951E-05	2.781E-05
	T_o (K)	T_o	298	298	298	298	298
	P_k (Mbars)		0.334	0.268	0.334		
Reacted products JWL	D (mm/μs)	D	7.98	7.70	7.98	7.47	
	R_{1p} (Mbars)	A	5.242	5.5748	5.242	7.5807	8.807
	R_{2p} (Mbars)	B	0.07678	0.0783	0.07678	0.08513	0.1836
	R_{3p} (Mbar/K)		3.4E-06	3.4E-06	3.4E-06	2.0E-06	3.8E-06
	R_{5p}	R_1	4.2	4.5	4.2	4.9	4.62
	R_{6p}	R_2	1.1	1.2	1.1	1.0	1.32
	ω_p	ω	0.34	0.34	0.34	0.20	0.38
	c_{vp}	C_v	1.0E-05	1.0E-05	1.0E-05	1.0E-05	1.0E-05
	Q_r (Mb·cc/cc)	E_o	0.085	0.081	0.085	0.103	0.104
	P_a (Mbars)		0.295	0.250	0.295	0.240	
Initiation term	F_q (μs^{-1})	I	44	44	4.0E+06	4.0E+08	7.43E+11
	F_r	b	0.222	0.222	0.667	0.667	0.667
	C_{crit}	a	0.01	0.01			
	η	x	4	4	7	7	20
Fast growth term	G_1 ($\mu s^{-1}Mb^{-z}$)	G_1	414	514	85	6	120
	s_1	c	0.222	0.222	0.222	0.667	0.667
	a_1	d	0.667	0.667	0.667	0.667	0.333
	m	y	2	2	2	1	2
Slow growth term	G_2 ($\mu s^{-1}Mb^{-z}$)	G_2			660	5500	400
	s_2	e			0.333	0.333	0.333
	a_2	g			1	1	1
	n	z			3	3	2
Limits	$F_{max,\ ig}$	F_{igmax}	0.3	0.3	0.022	0.02	0.3
	$F_{max,gr}$	F_{G1max}	1	1	0.6	0.5	0.5
	$F_{min,gr}$	F_{G2min}	1	1			0.5
Ref.			23	23	26	26	25

Table 7-2, part 2

	LX-17	LX-17	LX-17	LX-17	LX-17	LX-17	PBX-9404
	Two-term initiation	Three-term initiation	Three-term supracomp	cold 219 K initiation	heat 361 K initiation	heat 523 K initiation	Two-term initiation
ρ_o	1.905	1.905	1.905	1.905	1.905	1.7	1.842
R_{1e}	778.1	778.1	778.1	778.1	778.1	244.8	9522
R_{2e}	-0.05031	-0.05031	-0.05031	-0.05031	-0.05031	-0.0454	-0.05944
R_{3e}	2.22E-05	2.22E-05	2.22E-05	2.22E-05	2.22E-05	2.22E-05	2.47E-05
R_{5e}	11.3	11.3	11.3	11.3	11.3	11.3	14.1
R_{6e}	1.13	1.13	1.13	1.3	1.3	1.13	1.41
ω_e	0.8939	0.8938	0.8938	0.8938	0.8938	0.894	0.8867
c_{ve}	2.487E-05	2.487E-05	2.487E-05	2.487E-05	2.487E-05	2.487E-05	2.781E-05
T_o	298	298	298	298	298	523	298
P_k	0.337	0.337	0.337				0.398
D	7.596	7.596	7.596	7.596	7.596		8.8
R_{1p}	6.5467	5.31396	43.42773	5.31396	5.31396	6.5467	8.524
R_{2p}	0.071236	0.0270309	1.94564	0.0270309	0.0270309	0.0712	0.1802
R_{3p}	3.5E-06	3.5E-06	6.0E-06	4.6E-06	4.6E-06	3.5E-06	3.8E-06
R_{5p}	4.45	4.1	8.5	4.1	4.1	4.45	4.6
R_{6p}	1.2	1.1	3.28	1.1	1.1	1.2	1.3
ω_p	0.35	0.46	0.6	0.46	0.46	0.35	0.38
c_{vp}	1.0E-05	1.0E-05	1.0E-05	1.0E-05	1.0E-05	1.0E-05	1.0E-05
Q_r	0.069	0.069	0.07	0.069	0.069	0.062	0.102
P_a	0.275	0.290	0.250	0.290	0.290		0.370
F_q	50	4.0E+06	4.0E+06	2.8E+06	6.0E+06	1.0E+04	44
F_r	0.222	0.667	0.667	0.667	0.667	0.667	0.222
C_{crt}		0.22	0.22	0.22	0.22	0.22	
η	4	7	7	7	7	7	4
G_1	500	0.6	48	0.42	1.2	75	850
s_1	0.222	0.667	0.111	0.667	0.667	0.667	0.222
a_1	0.667	0.111	0.111	0.111	0.111	0.111	0.667
m	3	1	1	1	1	2	2
G_2		400	500	160	400	400	
s_2		0.333	1	0.333	0.333	0.333	
a_2		1	1	1	1	1	
n		3	3	3	3	3	
F_{xig}	1	0.5	0.0232	0.5	0.5	0.4	1
F_{xgr}		0.5	0.85	0.5	0.5	0.5	
F_{ngr}						0.5	
Ref.	15	17	20	18	18	24	15

Table 7-2, part 3

	PBX-9404	PBX-9404	PETN	PETN	PETN	PETN	PETN/Al5
	Two-term initiation	Three-term initiation	Two-term initiation	Two-term initiation	Two-term initiation	Two-term initiation	Three-term initiation
ρ_o	1.842	1.843	1.00	1.60	1.72	1.75	1.775
R_{1e}	9522	9522	13.12	21.88	346.6	37.46	12510
R_{2e}	-0.05944	-0.05944	-0.0784	-0.58	-3.3	-1.313	-0.06053
R_{3e}	2.47E-05	2.47E-05	3.40E-07	9.31E-06	2.18E-05	2.65E-05	2.47E-05
R_{5e}	14.1	14.1	11.0	7.8	10.0	7.2	14.4
R_{6e}	1.41	1.41	5.5	3.9	5.0	3.6	1.44
ω_e	0.8867	0.8867	0.02027	0.3468	0.7556	1.173	0.9875
c_{ve}	2.781E-05	2.781E-05	1.676E-05	2.685E-05	2.887E-05	2.263E-05	2.504E-05
T_o	298	298	298	298	298	298	298
P_k	0.398	0.398				0.452	
D	8.8	8.80				8.21	8.10
R_{1p}	8.524	8.524	2.372	6.253	6.17	6.17	5.942
R_{2p}	0.1802	0.1802	0.1061	0.2329	0.16926	0.16926	0.441
R_{3p}	3.8E-06	3.8E-06	2.4E-06	2.8E-06	2.5E-06	2.5E-06	5.2E-06
R_{5p}	4.6	4.6	5.6	5.25	4.4	4.4	4.9
R_{6p}	1.3	1.3	1.8	1.6	1.2	1.2	2.3
ω_p	0.38	0.38	0.24	0.28	0.25	0.25	0.52
c_{vp}	1.0E-05	1.0E-05	1.0E-05	1.0E-05	1.0E-05	1.0E-05	1.0E-05
Q_r	0.102	0.102	0.05706	0.0913	0.09815	0.101	0.120
P_a	0.370	0.370				0.335	0.320
F_q	44	7.43E+11	20	20	20	20	20
F_r	0.222	0.667	0.222	0.222	0.222	0.222	0.222
C_{crt}	0.01						
η	4	20	4	4	4	4	4
G_1	850	3.1	400	400	400	400	1000
s_1	0.222	0.667	0.222	0.222	0.222	0.222	1
a_1	0.667	0.111	0.667	0.667	0.667	0.667	0.667
m	2	1	1.4	1.4	1.4	1.4	1
G_2		400					66, 18.4
s_2		0.333					1
a_2		1					1
n		2					1
F_{xig}	0.3	0.3	1	1	1	1	0.03
F_{xgr}	1	0.5					0.86
F_{ngr}	1						0.86
Ref.	23	17	14	14	14	14	22

Table 7-2, part 4

	PETN/Al10	PETN/Al20	Prop B	RX-03-BB	RX-25-BF	RX-25-BH	RX-26-AF
	Three-term initiation	Three-term initiation	Three-term initiation	Two-term initiation	Three-term initiation	Three-term initiation	Three-term initiation
ρ_o	1.800	1.893	1.848	1.90	2.149	2.30	1.836
R_{1e}	12510	12510	40.66	108.2	286.9	286.9	2011
R_{2e}	-0.06053	-0.06053	-1.339	-2.406	-0.1453	-0.1453	-0.05204
R_{3e}	2.47E-05	2.47E-05	2.09E-05	3.41E-05	2.23E-05	2.23E-05	2.27E-05
R_{5e}	14.4	14.4	7.2	8.2	10.0	10.0	12.4
R_{6e}	1.44	1.44	3.6	4.1	2.0	2.0	1.24
ω_e	0.9875	0.9875	0.8351	1.251	0.8161	0.8161	0.9451
c_{ve}	2.504E-05	2.504E-05	2.504E-05	2.724E-05	2.730E-05	2.730E-05	2.406E-05
T_o	298	298	298	298	298	298	298
P_k				0.355			
D	8.00	7.88		7.596	7.506	6.01	8.239
R_{1p}	5.022	8.126	7.737	6.5467	53.24	20.62243	8.018
R_{2p}	0.269	0.654	0.1155	0.071236	0.514	0.286777	0.5264
R_{3p}	5.0E-06	4.2E-06	2.4E-06	3.5E-06	6.0E-06	6.0E-06	3.4E-06
R_{5p}	4.5	5.55	4.8	4.45	8.0	7.0	5.0
R_{6p}	2	2.23	1.2	1.2	1.75	1.0	2.1
ω_p	0.50	0.42	0.24	0.35	0.60	0.60	0.34
c_{vp}	1.0E-05	1.0E-05	1.0E-05	1.0E-05	1.0E-05	1.0E-05	1.0E-05
Q_r	0.120	0.123	0.12	0.069	0.10	0.08	0.085
P_a	0.325	0.320		0.275	0.280	0.210	0.325
F_q	20	20	4	50	7.43E+11	7.43E+11	14
F_r	0.222	0.222	0.667	0.222	0.667	0.667	0.667
C_{crt}					0.03		
η	4	4	4	4	20	20	4
G_1	1000	1000	3.1	125	3.1	3.1	488
s_1	1	1	0.667	0.222	0.667	0.667	0.667
a_1	0.667	0.667	0.111	0.667	0.111	0.111	0.333
m	1	1	1	2	1	1	2
G_2	66, 18.4	66, 18.4	18		25	85	500
s_2	1	1	0.111		0.667	0.667	0.222
a_2	1	1	1		0.111	0.111	0.667
n	1	1	2		1.2	2	3
F_{xig}	0.03	0.03	0.015	1	0.03	0.03	0.05
F_{xgr}	0.74	0.58	0.12		0.38	0.19	0.5
F_{ngr}	0.74	0.58					
Ref.	22	22	21	14	19	19	16

Table 7-2, part 5

	RX-HD (ANFO)	TNT cast	TNT	TNT/Al5	TNT/Al10
	overdriven	Two-term initiation	Two-term supracomp	Three-term initiation	Three-term initiation
ρ_o	1.32	1.61	1.645	1.635	1.670
R_{1e}	100	17.98	171.01	202.8	202.8
R_{2e}	-0.026959	-0.931	-0.03745	-0.0375	-0.0375
R_{3e}	1.53E-05	1.83E-05	1.53E-05	1.54E-05	1.54E-05
R_{5e}	9.8	6.2	9.8	10.0	10.0
R_{6e}	0.98	3.1	0.98	1.0	1.0
ω_e	0.5647	0.8926	0.5647	0.5675	0.5675
c_{ve}	2.717E-05	2.050E-05	2.717E-05	2.713E-05	2.713E-05
T_o	298	298	298	298	298
P_k	0.200	0.281			
D	7.0	6.845	6.93	6.80	6.80
R_{1p}	4.8245	3.712	33.94889	19.736	17.653
R_{2p}	0.14104	0.032306	0.821662	1.466	0.535
R_{3p}	5.5E-06	3.0E-06	6.0E-06	5.7E-06	4.5E-06
R_{5p}	5.075	4.15	8.3	8.8	7.4
R_{6p}	2.0	0.95	2.8	3.4	2.4
ω_p	0.55	0.30	0.60	0.57	0.45
c_{vp}	1.0E-05	1.0E-05	1.0E-05	1.0E-05	1.0E-05
Q_r	0.048	0.07	0.058	0.076	0.082
P_a	0.16	0.21	0.180	0.195	0.190
F_q	25	50	50	50	50
F_r	0.667	0.222	0.667	0.667	0.667
C_{crt}					
η	4	4	4	4	4
G_1	0.4	40	360	360	360
s_1	0.667	0.222	1.0	1	1
a_1	0.667	0.667	0.667	0.667	0.667
m	1	1.2	1.2	1.2	1.2
G_2				90, 25	90, 25
s_2				1	1
a_2				1	1
n				1	1
F_{xig}	0.16	1	0.03	0.03	0.03
F_{xgr}	1		1	0.85	0.70
F_{ngr}				0.85	0.70
Ref.	26	14	20	22	22

Chapter 8. Thermochemical Codes

1. Descriptions of the Codes

Besides the hydrocode, the other major class of explosive code is the thermochemical code. These codes start with an explosive of given composition, density, and heat of formation and calculate the products at various relative volumes along with their pressures and energies. The models assume thermodynamic equilibrium and are based on thermodynamic data tables. The codes know nothing about chemical kinetics.

The most generally used code is TIGER. It has two different submodels: the BKW (for Becker, Kistiakowsky, and Wilson) and the JCZ3 (for Jacobs, Cowperthwaite, and Zwisler). The BKW dates to World War II and calculates a Gas Law compressibility,[1–4]

$$PV/RT = 1 + x\exp(\beta x), \tag{1}$$

where

$$x = \kappa \sum_i x_i k_i / V(T+\vartheta)^{\alpha}. \tag{2}$$

Here, P is the pressure, V the molar volume of the detonation products, T the temperature, R the gas constant, x_i the mol fraction of component i, and the rest are constants—with the k_i known as covolumes because they mock up the molar volumes occupied by the compounds.

The Tiger JCZ3 code sought to be more physical by including intermolecular Lennard-Jones potentials between the various gaseous species.[5] A single gaseous phase was created, and each product species has the two Lennard-Jones constants, which should be directly derivable from data. Both models are able to handle liquid and solid phases created at high temperature separately from the gas phases. A liquid like water that condenses at low temperature is not handled accurately and is better left as vapor. Both models are quick and can be run on a PC386 in a few minutes. Only gaseous C, H, N, O, and F compounds are available in JCZ3, although the list could be extended. It is common in JCZ3 to ignore gaseous species that we don't have and run with a condensed one (e.g., Al_2O_3) that does not require Lennard-Jones constants.

The new CHEQ (for chemical equilibrium) code, created by Francis Ree, was a considerable extension of JCZ3, and was again based on intermolecular potentials.[6,7] The code is unusual in being able to calculate the equilibrium properties of nonsoluble phases of gaseous and solid detonation products. The

goal of CHEQ is to be a truly scientific code for explosives. However, the CHEQ code takes overnight to two days on a MIPPS2000 to obtain the CJ point and the adiabat. It has been rewritten for general use in windows format by A. Nichols.[8] Because it is slow, CHEQ will not be used for the rough performance calculations on new compounds. Its greatest power lies in its ability to predict the detailed shape of the adiabat with some hope of being correct. CHEQ2.5 is used here. Also included for comparison are recent results by G. Kerley using PANDA, the Sandia National Laboratories' (SNL) analog of CHEQ.[9,10]

For quick calculations, TIGER is still the best code. However, it comes in many versions, in addition to the basic choice of BKW or JCZ3. BKW can be used as BKWR (for revised) and BKWS (for SNL). The difference lies mainly in the basic constants, which are listed in Table 8-1. The thermodynamic libraries are also slightly different, even though they are fits of the literature JANNAF data. Also, the LLNL PC program is slightly different from the SNL Sun/Cray program—so the platform should be mentioned. This lack of standardization has followed TIGER throughout its life as a public domain code.

The BKWR version is old and was created to produce accurate detonation velocities and pressures.[11] Both the constants (α is 0.5, β 0.is 176, κ is 11.80, and Θ is 1850 K) and the covolumes were arrived at by fiddling over time. However, the C-J detonation temperatures are about a thousand degrees too low, and the energies of detonation, E_d, at v ~ 2 to 7 are uniformly about 10% too high. J. Kury fixed these discrepancies by using 1.763 g/cc PETN as a standard. At v = 2.2, the standard cylinder JWL for PETN gives E_d(PETN, cylinder) = 6.51 kJ/cc, while E_d(PETN, BKWR) = 7.30 kJ/cc. This ratio of 0.89 is applied to the BKWR value for an unknown explosive, also at v = 2.2 to obtain

$$E_d\,(\text{BKWR corrected}) = \frac{E_d\,(\text{PETN, cylinder})}{E_d\,(\text{PETN, BKWR})}\,E_d\,(\text{BKWR}) \qquad (3)$$

This effectively lowers all detonation from $2 < v < 7$ energies by 10%. For the total energy of detonation, E_o, the cylinder and BKWR values are 10.80 and 10.68 kJ/cc, so that the correction is negligible.

To summarize, the calculated BKWR energies for PETN are corrected at each of the three cylinder volumes as listed below.

	Det. energies (kJ/cc)		
Relative Volume	BKWR calculated	BKWR corrected	Ratio
2.2	7.30	6.51	0.892
4.1	8.81	7.87	0.893
6.5	9.39	8.55	0.910

(4)

This method is an awkward but effective correction to BKWR, which was originally designed for detonation velocities and pressures, so that it will now handle energies. This arrangement has persisted because the energy of detonation has not been considered a prime variable for matching until now.

The low detonation temperatures were noticed by Hobbs and Baer at SNL, and they recently created the new version of BKWS.[12–15] The covolumes are listed in Table 8-1 and differ from the LLNL set. The thermodynamic library is different as well. The constants α, β, κ, and Θ were first set in BKWS at 0.5, 0.174, 11.85, and 5160 K and have since been reset to 0.5, 0.298, 10.5, and 6620 K. The temperatures were raised by increasing Θ, and the energies of detonation decreased as a result. This allows the calculated energies of detonation to be used without correction.

Hobbs and Baer also used a generating algorithm to turn out a large number of covolumes for compounds and free radicals from all over the periodic table, although the constants have been derived solely for CHNO explosives. Thus, TIGER can be run on all kinds of reactions, whether detonating or not.

2. Comparison of Code Results

We shall now compare the thermochemical code results for a set of homogeneous explosives listed in Tables 8-2 and 8-3. The code results are compared with detonation velocities measured in the cylinders and total energies of detonation measured by calorimetric detonation.[16] The energy of detonation, E_d, at some given volume is determined from the equation

$$E_d = \left(\frac{u}{u\,(\text{PETN})}\right)^2 E_d\,(\text{PETN}). \tag{5}$$

The cylinder velocities are given by u. The codes are run with all species frozen into final equilibrium at 1800 K. All the codes in Tables 8-2 and 8-3 were run on the PC with the LLNL TIGER program. SNL constants and library were used for BKWS. The minimum library listed in Table 8-1 was used. Although Hobbs and Baer list library data for many radicals, these are passed through quickly by TIGER and add nothing to the result except running time, while increasing the probability of a crash. If a solid final species was likely, no gaseous intermediates were used. All water was allowed to go only to gas because partial condensation often occurs in the code. The presence of formic acid, HCOOH, is essential in the library or the detonation velocity jumps to large and unrealistic values.

The results of Tables 8-2 and 8-3 show that the TIGER codes produce results as good as the larger CHEQ and PANDA codes do. Earlier in this

report we calculated total energies of detonation to within ±10% assuming incomplete burning of CO. With the TIGER codes, we can improve this to about ±5%, at least for these explosives. Within the three versions of TIGER, JCZ3 is slightly off on detonation velocity, which could be fixed by renormalizing. BKWS is certainly more realistic with hotter temperatures, and there is no need to fudge the energies, but the spread of energy results in BKWS is larger than for BKWR. Worse yet, some favorite explosives do not fare well. JCZ3 has another problem, seen when we compare the energies at v = 2.2 and 6.5. The average energy in JCZ3 moves 7% (from –1 to +6), whereas the 4% seen in the other codes is more reasonable. Hence, JCZ3 dumps its energy too fast.

The thermochemical code calculates the C-J pressure—the true equilibrium value. A benefit of the fudged energies in BKWR is that the calculated C-J pressure is generally close to the measured detonation or JWL pressures. However, the C-J pressures calculated by JCZ3 and CHEQ are low, as seen in this table.

	BKWR	JCZ3	CHEQ
Average	1	–10	–13
Std. dev.	9	11	20
No. larger	8	3	2
No. smaller	12	17	18

(6)

This pressure is important because it defines the starting point of the adiabat. For 1.763 g/cc PETN, the standard JWL C-J point is 31.5 GPa at a volume, v_{cj}, of 0.739. In CHEQ, it is 29.3 GPa at 0.763. The thermochemical code cannot see nonequlibrium processes that could cause the actual measured detonation pressure to be higher.

Finally, we consider the C-J temperatures for which the measurements will really be adiabat temperatures. Measured temperatures are obtained from a multifrequency optical measurement in the visible region. Little data exists, and it is not clear how to interpret it. At the very least, the entire time track needs to be shown, and this is a rare occurrence. For example, Kato et al. show detonated TNT of 1.51 g/cc rising to a peak at about 3600 to 4000 K over 0.5 μs.[17] The TNT then decays to 2500 to 2700 K at about 2.5 μs. The experiment stops there, with the temperature still declining. They appear to show a 2800-K calculated adiabat temperature, but there is no way to tell how they got it. The predicted tempera-tures for 1.6 g/cc TNT are BKWR 2670 K, JCZ3 3070 K, and CHEQ 3820 K. This is the origin of the statement that BKWR is too low and the other two are at least reasonable. However, we cannot tell

where the adiabat point is in the data. The 3800-K high point might be the adiabat point, but some think this is a hot-spot effect.

3. Detonation Temperature for Nitromethane

Eventually, measured temperatures may be good enough to use to calibrate thermochemical codes. Nitromethane (NM) is a popular substance for measuring detonation temperatures because it is transparent and the light is easily collected. Kato et al. reviewed eleven literature measurements and found a value of 3500 ± 200 K.[18] They measured NM at five wavelengths from 0.55 to 0.95 μm and obtained values of 3400 ± 50 K. All standard deviations are probably precision rather than accuracy. Their value was the maximum measured at time zero, and they followed the decay of the Taylor wave for 2 μs.

A good detonation temperature has recently been optically measured for (unactivated) nitromethane by Choong-Shik Yoo of H Division.[19] The intent was to create the pressure plateau of supracompression, discussed as the best detonation-point searching tool in Chapter 6. Four shots were run on the H-Division two-stage gas gun. A 4-mm-thick aluminum flyer hit a sample cell made of a 2-mm aluminum buffer plate, 6 mm of nitromethane, and a 2-mm sapphire window. The diameter of the NM was 19 mm so that it took 1.5 μs for the edge effects to reach the sample center. Four flyer velocities of 3.11, 2.88, 2.55, and 2.24 mm/μs were used.

The experiment was modeled in the LLNL 1-D code using the NM JWL presented in Chapter 5. The JWL carried the assumptions that the NM detonates at time zero and that the detonation pressure is 12.0 GPa. Above this pressure, a totally flat pressure plateau is obtained using the JWL. Just below the detonation pressure, the code again shows a flat plateau but with a small spike at the start. Thus, finding the detonation point in the code would be difficult, going by just the pressure traces.

Fig. 8-1 shows the optical results of the nitromethane experiment in terms of temperature. All three runs were above the 12.0-GPa cylinder detonation pressure, as calculated by the 1-D code. The supracompression plateau is very obvious, and it shortens as one drops toward the detonation point. The lowest flyer velocity failed to detonate the nitromethane and so confirmed the presence of the detonation point at a slightly higher pressure. The preliminary plateau results from this work are as follows:

Shot no.	Flyer velocity (mm/μs)	1-D pressure (GPa)	1-D relative volume	Average meas. temp. (K)	Time meas. (μs)
1	3.11	16.0	0.657	3967 ± 18	0.69
2	2.88	14.7	0.679	3904 ± 19	0.59
3	2.55	12.8	0.713	3886 ± 40	0.34
Cylinder C-J		**12.0**	**0.731**	**3840**	
4	2.24	11.2	0.749		

(7)

The standard deviations represent precision.

We extrapolate linearly to the expected JWL pressure at 12.0 GPa and obtain

$$T_p = 3840 \text{ K} \tag{8}$$

for NM. Although this is really a detonation or, at best, an adiabat temperature, it is tempting to use it as a code calibration of the C-J temperature. CHEQ at 3770 K is closest in predicting this result and BKWR, as expected, is worst.

It is interesting to speculate whether the 400-K difference between the Taylor wave and the supracompression experiments is real. C. Tarver notes that the initial hottest temperatures may be missed in the Taylor wave measurement because it decays so quickly. However, the supracompression plateau could last long enough for carbon to precipitate, thereby releasing energy that pushes the temperature up.

4. Freezing the Compositions

A command in TIGER freezes the compositions at the arbitrary temperature of 1800 K. This prevents the carbon monoxide from reacting all the way to CO_2. We recall that BKWR is always cold and CHEQ is hot, so that the 1800-K freeze in effect freezes over a wide range of "real" temperatures. Below, we compare CHEQ runs with Ornellas' calorimetry in mols gas per mol explosive.

Explosive	Approx. density (g/cc)	Carbon monoxide		
			CHEQ	
		Meas'd	Freeze	Eqm
BTF	1.85	4.6	3.9	0.6
FEFO	1.61	1.9	1.8	0
HMX	1.89	1.1	1.6	0
HMX	1.19	2.7	2.6	0.1
HNB	1.96	0.3	0	0
HNS	1.68	4.7	5.9	1
NM	1.13	0.6	0.6	0
PETN	1.76	1.7	1.6	0
TNT	1.63	2.0	2.4	0.2

(9)

The measured and 1800-K frozen CHEQ runs agree, but the CHEQ runs allowed to react to equilibrium down to low temperature have almost no carbon monoxide left. All the samples listed above were heavily confined within the calorimeter so that the reshocking at the calorimeter wall is thought not to raise the temperature above 1500 to 1800 K.[16] The reshock model could profitably be run again in more detail.

Table 8-4 shows the detailed compositions for TIGER BKWR and CHEQ for three explosives at the C-J point, the 1800-K freeze point, and at equilibrium at 1 atm. The latter two points are on the adiabat. Our intent is to guess the kinetics. We see that the results of TIGER and CHEQ are in agreement for each explosive but the kinetics differ. The kinetics may be summarized as follows:

PETN:	at C-J	have CO_2 + HCOOH	
	to 1800 K	HCOOH —> CO + H_2O	
	to equilibrium	2CO + H_2O —> CO_2 + CH_4	(10)
BTF:	at C-J	have C + CO_2	
	to 1800 K	C + CO_2 —> 2CO	
	to equilibrium	2CO —> C + CO_2	(11)
TATB:	at C-J	have C + CO_2	
	to 1800 K	no change	
	to equilibrium	2C + H_2O —> CO_2 + CH_4	(12)

The reactions between 1800 K and the one-atmosphere equilibrium represent the kinetics that we freeze without the physical understanding of why.

5. Phase Transitions and Look-Up Tables From CHEQ

CHEQ's specialty is calculating multiple phases. CHEQ has aroused interest in the solid graphite-to-diamond transition and the splitting of nitrogen-water into two gas phases.

The precipitation of carbon is well-known and necessary if no oxygen is there to burn it; the presence of diamonds in detonation soot has also been seen in TNT and TATB-based explosives.[20] Steinberg and Ree suggested that the presence of the diamond-graphite transition can be seen in the initial density-detonation velocity curve.[21,22] PETN, for example, shows an absolutely straight line for detonation velocity vs sample density, but no one expects carbon precipitation in this oxygen-rich explosive. A different result appears for HMX and RDX, for which a small change-of-slope appears between 1.0 and 1.5 g/cc.[22,23]

Can the phase transition actually be seen in an explosive? The effect of this phase transition in TATB has been calculated by A. Nichols using CHEQ2.5 and the results are in Table 8-5. The three combinations tried are (1) all carbon phases in equilibrium, (2) diamond only, and (3) graphite only. The mixed-phase and diamond-only phase begin at the same C-J point because diamond is the high-pressure equilibrium phase. In these runs, the N_2-H_2O was allowed to separate into two phases. The diamond-only model has a C-J point 3 GPa lower than the graphite-only, but this would be hard to check, given the problems we have in determining where the LX-17 detonation pressure is. The detonation energies offer a better chance. The percent comparison with the mixed-phase carbon model gives these results:

	% E_d (kJ/cc)		
Carbon phases	v = 1. 2	v = 2.2	v = 6.5
Diamond: mixed	–2	–3	–2
Graphite: mixed	8	3	2

(13)

An all-graphite version of TATB at 8% should be obvious near the C-J point, and the study of plates should answer the question. All other points with a 2 to 3% difference are more difficult but should also be possible.

The phase splitting of nitrogen-water into a nitrogen-rich gas phase and a water-rich gas phase is more controversial because doubts exists as to whether or not there is time for phase separation in a detonation. The phase splitting has been measured isothermally and reversibly to 830 K and 2.1 GPa.[24–26] These pressures are far too low to be easily extrapolated to the explosive regime. Fig. 8-2 shows the phase diagram as calculated by CHEQ. The two-phase line is that for a 50-50 mol% overall gaseous combination. The isothermal data are

hardly to be found. The dashed lines are the adiabats for dense HMX and TATB, where two phases are calculated by CHEQ. As their pressures drop, the two phases merge and one is created. Steinberg sought to find the nitrogen-water transition for HMX at about 1.5 g/cc with a C-J pressure vs density plot, but he concluded that the evidence was ambiguous.[23] Recently, Koshi et al. added evidence to support the presence of the phase transition. They performed a Monte Carlo calculation on up to 256 particles and found that phase separation occurred in tens of picoseconds—certainly a fast time and one that would cause phase separation in a real explosive.[27]

We now run TATB again in CHEQ with both N_2-H_2O phases and with only phase allowed. In these runs, the carbon has the mixed phase capability. The detailed results are listed in Table 8-5, and the percent energy comparisons are:

	% E_d	(kJ/cc)	
N_2-H_2O phases	v = 1. 2	v = 2.2	v = 6.5
One-phase:	0.8	0.0	–0.2
Two-phase			

(14)

The code says that phase separation of nitrogen and water will not be measurable in TATB.

Haselman, van Thiel, and Ree first incorporated the phase transitions into the EOS for LX-14 and LX-17. Their presence may be seen in the function $\gamma = -\partial \ln P/\partial \ln v$ as shown in Fig. 8-3 using CHEQ2 in 1991. For LX-17, the higher temperature dip is assigned to the graphite-diamond phase transition and the lower temperature one to the nitrogen-water transition.[28] The situation is reversed for LX-14, which burns hotter, although Fig. 8-3 shows the two transitions merged into one large dip. Also shown is the JWL no. LH for LX-17, which is smooth and peaks near $v \sim 1$.

The dips in γ correspond to blips in the adiabat pressure, which appear small but might affect the detonation energy. Clearly, a JWL cannot reproduce blips, and this has led to the Look-Up Table. Fig. 8-4 shows the difference between the adiabat pressure calculated by the JWLs and those calculated from the Look-Up Tables for LX-14 and LX-17. The pressure differences are up to 0.9 GPa, and two separate features may seen in LX-17. The Look-Up Tables that generated these pressures were built from the output of CHEQ2.

Table 8-6 shows the Look-up Tables derived from CHEQ by L. Haselman for LX-14 and LX-17. These may be used, with an interpolation routine, to generate the Principal Adiabat described in Chapter 1. From Table 8-6, we note that the function f falls, as expected, from a higher value at small volumes. It passes through a minimum and rises again at large volumes. We recall from Chapter 2 that f should approach ω and be constant at large volumes. It does not

in this table because of the definition of the adiabat energy, E_s. CHEQ calculates an internal energy per unit mass, E_i, which is converted into the energy of detonation per cc, E_d, by

$$E_d = E_i\rho_o + H_f, \tag{15}$$

where H_f is the heat of formation. In Eq. (15), E_d and E_i are positive, according to the convention of this report. Of necessity, however, H_f retains the negative chemist's convention—which is the reason for the plus sign in Eq. (15). (CHEQ actually uses negative values of E_d and E_i,).

The total energy of detonation, E_o, is found from Eq. (15) using the value of E_i at 1 atm. If we define the adiabat energy by

$$E_s = E_o - E_{d(v)}, \tag{16}$$

we will obtain a function for f, the quantity in the Look-Up Table, that has a minimum at large volumes.

In the JWL, however, we recall that E_o is obtained at $v \longrightarrow \infty$ where $P \longrightarrow 0$, and this sets $E_s = 0$. We therefore define $E_o(\infty)$, which would be the energy of detonation, at $v \longrightarrow \infty$. Then,

$$E_s = E_{o(\infty)} - E_d, \tag{17}$$

and f will now be constant at large volumes as expected. For 1.763 g/cc PETN in CHEQ, E_o is 10.36 kJ/cc, and $E_o(\infty)$ is 11.00 kJ/cc. This adds a large 0.64 kJ/cc to the adiabat energy everywhere, and it creates a near-constant value of f of

$$f(\text{PETN}) = 0.289 \pm 0.004, \quad 19 < v < 1780. \tag{18}$$

The added energy in adjusting the adiabat energy back to 1 atm is larger in CHEQ, where it is supposed to be accurate, than it is in the JWL, where a convergent integral at $v \longrightarrow \infty$ is required. In other words, the JWL pressure is deliberately made to decrease faster at large volumes to make simple integration possible.

6. References

1. M. Cowperthwaite and W. H. Zwisler, *Tiger Computer Program Documentation,* Stanford Research Institute Publication Z106, 1973.

2. R. D. Cowan and W. Fickett, *J. Chem. Phys.* **24,** 932 (1955).

3. M. Finger, E. Lee, F. H. Helm, B. Hayes, H. Hornig, R. McGuire, M. Kahara, and M. Guidry, "The Effect of Elemental Composition on the Detonation Behavior of Explosives," *Proceedings of the Sixth Symposium (International) on Detonation,* Coronado, CA, August 24–27, 1976 (Office of Naval Research, Arlington, VA, ACR-221), pp. 710–722.

4. C. L. Mader, "Numerical Modeling of Detonations," University of California, Berkeley, 1979, pp. 412–448.

5. M. Cowperthwaite and W. H. Zwisler, "The JCZ Equations of State for Detonation Products and their incorporation into the Tiger Code," *Proceedings of the Sixth Symposium (International) on Detonation,* Coronado, CA, 24–27 August 1976 (Office of Naval Research, Arlington, VA ACR-221), pp. 162–172.

6. F. H. Ree, *J. Chem. Phys.* **81,** 1251 (1984).

7. F. H. Ree, *J. Chem. Phys.* **84,** 5845 (1986).

8. A. L. Nichols III and F. H. Ree, *CHEQ 2.0 User's Manual,* Lawrence Livermore National Laboratory, Livermore, CA, UCRL-MA-106754 (1990).

9. G. I. Kerley, "Theoretical Equations of State for the Detonation Products of Explosives," *Proceedings Eighth Symposium (International) on Detonation,* Albuquerque, NM, July 15–19, 1985, p. 540.

10. G. I. Kerley and T. L. Christian-Frear, "Prediction of Explosive Cylinder Tests using Equations of State from the PANDA Code," preprint, private communication , 1993.

11. M. Finger, E. Lee, F. H. Helm, B. Hayes, H. Hornig, R. McGuire, M. Kahara, and M. Guidry, "The Effect of Elemental Composition on the Detonation Behavior of Explosives," *Proceedings Sixth Symposium (International) on Detonation,* Coronado, CA, August 24–27, 1976, p. 710.

12. M. L. Hobbs and M. R. Baer, *Nonideal Thermoequilibrium Calculations using a Large Product Species Data Base,* Sandia National Laboratories, Albuquerque, NM, SAND92-0482 (1992).

13. M. L. Hobbs and M. R. Baer, "Calibration of the BKW-EOS and Application to Aluminized Composite Explosives," *5th International Conference of the Groupe de Travail de Pyrotechnie Euro Pyro 93,* (1993) p. 1.

14. M. L. Hobbs and M. R. Baer, "Calibrating the BKW-EOS with a Large Product Species Data Base and Estimated C-J Properties," *Tenth International Detonation Symposium,* Boston, MA, (1993), preprint.

15. M. L. Hobbs and M. R. Baer, Sandia National Laboratories, Albuquerque, NM, private communications, 1992–1993.

16. D. L. Ornellas, *Calorimetric Determinations of the Heat and Products of Detonation for Explosives: October 1961 to April 1982,* Lawrence Livermore National Laboratory, Livermore, CA, UCRL-52821 (1982).

17. Y. Kato, N. Mori, H. Sakai, T. Sakurai, and T. Hikita, "Detonation Temperature of Some Liquid and Solid Explosives," *Proceedings Ninth Symposium (International) on Detonation,* Portland, OR, August 28–September 1, 1989, II, pp. 939–946.

18. Y. Kato, N. Mori, H. Sakai, K. Tanaka, T. Sakurai, and T. Hikita, "Detonation Temperature of Nitromethane and some Solid High Explosives," *Proceedings Eighth (International) Symposium of Detonation,* Albuquerque, NM, July 15–19, 1985, pp. 558–566.

19. C.-S. Yoo, Lawrence Livermore National Laboratory, Livermore, CA, to be published.

20. N. R. Greiner, D. S. Phillips, J. D. Johnson, and F. Volk, *Nature* **333,** 440 (1988).

21. F. Ree, *J. Thermo. Phys.* **36,** 3373 (1987).

22. D. J. Steinberg, "Comparison of Experimental Data on Detonation Velocity and Chapman-Jouget Pressure vs Initial HE Density with Predictions from Ree's Model Equation of State," *Proceedings Eighth (International) Symposium of Detonation,* Albuquerque, NM, July 15–19, 1985, pp. 513–520.

23. M. van Thiel and F. H. Ree, *J. Appl. Phys.* **62,** 1761 (1987).

24. M. L. Japas and E. U. Franck, *Ber. Bunsenges. Phys. Chem.* **89,** 793 (1985).

25. M. G. E. van Hinsburg, R. Verbrugge, and J. A. Schouten, *Eleventh Symposium on Thermophysical Properties,* Boulder, CO, June 23–27, 1991.

26. M. Costantino and S. F. Rice, *J. Phys. Chem.* **95,** 9034 (1991).

27. M. Koshi, H. Matsui, T. Saito, and K. Takayama, "A Theoretical Study for Gas-Gas Separation in High Temperature and High Pressure Fluid," *Tenth International Detonation Symposium,* Boston, MA, July 12–16, 1993, Paper Summaries, pp. 118–121.

28. M. van Thiel, memo to L. Haselman, April 22, 1991.

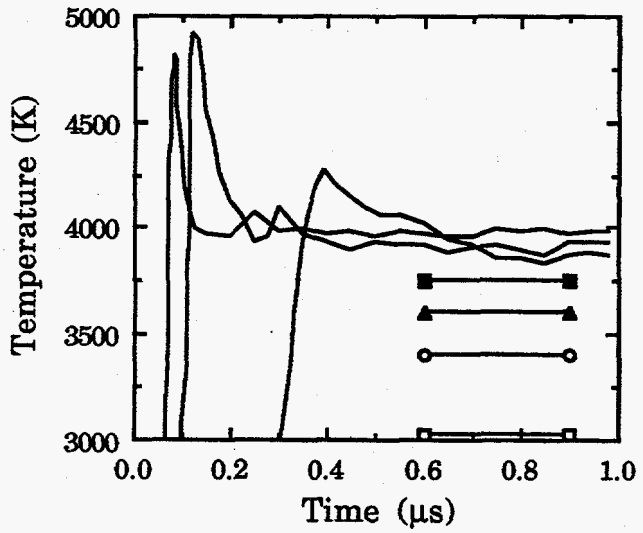

Fig. 8-1. Measured spectral emission data for temperature for the three supracompression runs above the detonation pressure of nitromethane. From left to right, the pressures are 16.0, 14.7, and 12.8 GPa. The averaged data are extrapolated to 12.0 GPa to obtain a detonation temperature of 3840 K. From top to bottom, the code results are from CHEQ, JCZ3, BKWS and BKWR.

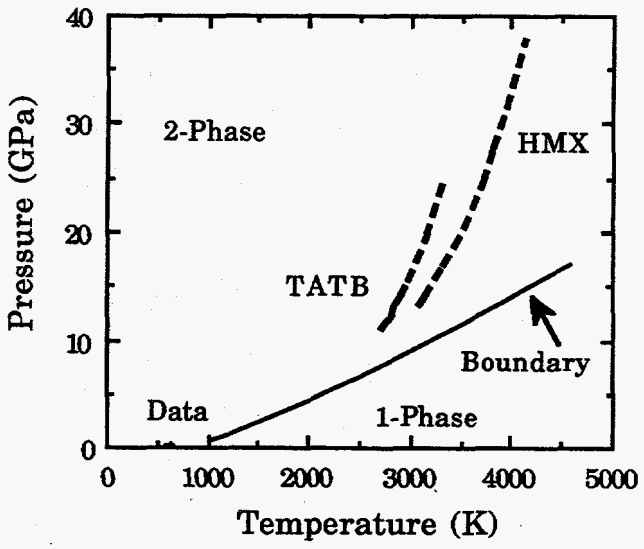

Fig. 8-2. CHEQ's predictions of N_2-H_2O phase separation. The line represents the separation in a 50-50 mol% mix of nitrogen and water, with the two-phase region at the top. The measured data are shown in the blip at the far left. The calculated two-phase lines in detonating HMX and TATB are shown by the two dashed lines. At lower pressures, one-phase behavior results.

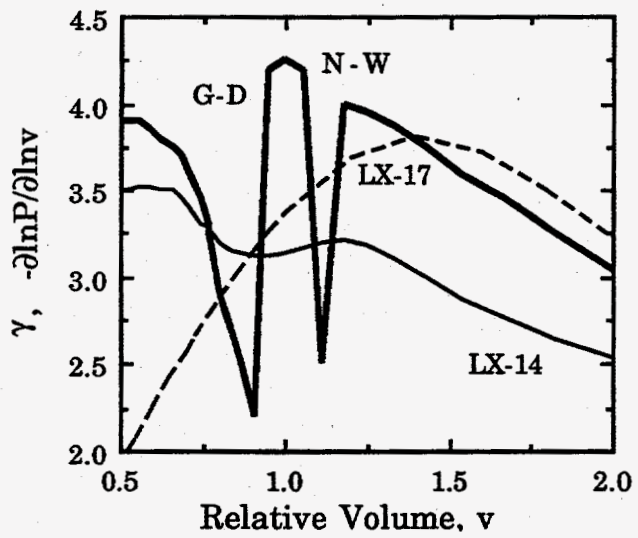

Fig. 8-3. Adiabatic γ, equal to –∂lnP/∂lnv, as a function of the relative volume for LX-14 and LX-17. The solid lines are the predictions from CHEQ. For LX-17 (heavy line), the graphite-diamond (G-D) and nitrogen-water (N-W) phase transitions are indicated. The dotted line is the LH JWL for LX-17.

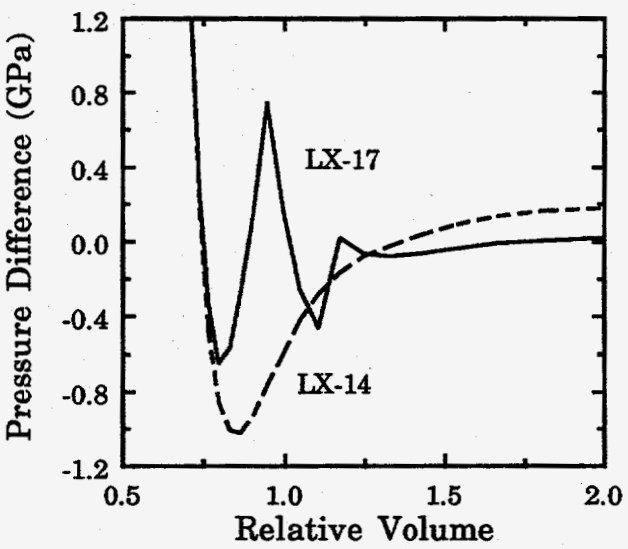

Fig. 8-4. Pressure difference between the Look-Up Table and the JWL for LX-14 and LX-17 as a function of relative volume. The pressure blips are the result of the suspected phase transitions. Confirming the existence of these blips is a challenge for the future.

Table 8-1. Constants used in the two versions of BKW and JCZ3. The constants α, β, κ, and Θ define the version of BKW. The other constants go into the respective libraries. The elements are C, H, N, O, F, Cl, Al, Li, Na, K, and Zr. The abbreviation A is Angstroms.

		LLNL BKWR	SNL BKWS	JCZ3- both libraries	
BKW defining constants	α	0.5	0.5		
	β	0.176	0.298		
	κ	11.8	10.5		
	Θ (K)	1850	6620		
		Covolumes (A^3)		r_o (A)	e_o (K)
Libraries- Common gases	CH_3OH		800		
	CH_4	550	493	4.29	154
	CO	440	614	4.05	120
	CO_2	610	663	4.20	200
	H_2	98	153	3.34	37
	H_2O	270	376	3.35	138
	HCN	986	892		
	HCOOH	722	865	4.15	462.5
	N_2	404	376	4.05	120
	NH_3	384	418	3.35	138
	NO	386	394	3.97	105
	O_2	325	316	3.73	132
Other gases	CCl_4	1840	1840		
	CF_4	1100	1260	5.00	220
	Cl_2	532	872	4.61	336.9
	F_2	387	343	3.50	200
	HCl	643	570		
	HF	389	351	3.30	100
Condensed species	Al_2O_3	Li_2O	Na_2O	AlF_3	
	C	Li_2CO_3	ZrO_2	KF	
	K_2CO_3	LiOH		LiF	
	K_2O	Na_2CO_3		NaF	

Table 8-2. Comparison of experimental cylinder detonation velocities and the calorimetric total detonation energies with the values calculated by five thermochemical codes. The %-calculated compares the measured value with the calculated value (calculated value in the denominator).

		Detonation velocity					Total energy of detonation			
Explosive	Density (g/cc)	% cf. BKWR	% cf. BKWS	% cf. JCZ3	% cf. CHEQ	% cf. PANDA	% cf. BKWR	% cf. BKWS	% cf. JCZ3	% cf. CHEQ
BTF	1.852	2	4	-4	2	–1	3	–2	9	1
1,2-DP	1.26	–3	4	–3	–4		12	7	5	–3
FEFO	1.607	2	1	–1	–2		–7	–3	–4	–5
HMX	1.893	0	–3	0	–3	0	–4	–2	1	–2
HMX	1.188	–4	–1	0	–3	–1	–6	–4	–3	–3
HNB	1.965	6	6	4	7	1	–2	–1	2	5
HNS	1.655	1	–1	3	2		2	–9	12	7
HNS	1.001	–5	–4	–5	–9	–2	–1	–13	5	–4
NM	1.13	–6	–5	3	0	1	–10	–8	–2	–4
PETN	1.763	–1	–5	2	–1	0	–5	–3	–1	–2
PETN	1.503	–1	–3	3	0	1	–2	–1	–1	2
RX-23-AA	1.424	2	0	8	2	1	1	2	4	–4
RX-23-AB	1.356	1	–3	5	2	1	5	7	7	10
RX-23-AC	1.136	–1	6	23	–1	1	–8	–5	–9	–12
TATB	1.86	–4	–6	–3	–4	–6	9	–7	6	–3
TNT	1.632	2	–1	8	5	1	–9	–8	17	–1
Average		–1	–1	3	0	0	–1	–3	3	–1
Stdev		3	4	7	4	2	6	5	7	5

Table 8-3. Comparison of experimental cylinder detonation velocities at relative volumes of 2.2 and 6.5 with the values calculated by five thermochemical codes. The %-calculated compares the measured value with the calculated value (calculated value in the denominator). The cylinder velocities-squared have been set with PETN energies to calculate all other detonation energies.

	Energy of detonation at v = 2.2					Energy of detonation at v = 6.5				
Explosive	% cf. BKWR	% cf. BKWS	% cf. JCZ3	% cf. CHEQ	% cf. PANDA	% cf. BKWR	% cf. BKWS	% cf. JCZ3	% cf. CHEQ	% cf. PANDA
BTF	0	–6	–12	–2	–4	4	–3	0	1	3
1,2-DP	–17	15	3	5		–7	18	7	11	
FEFO	–13	–7	–7	–2		–7	–2	0	1	
HMX	–7	–6	–6	–3	0	–1	–2	2	2	6
HMX	3	–1	5	18	4	7	4	11	15	9
HNB	–1	–1	0	12	13	1	1	6	11	11
HNS	–6	–14	–10	–1		0	–9	2	0	
HNS	–10	–17	–8	5	–10	–4	–12	1	2	–3
NM	–9	–10	–2	9	0	–6	–6	4	8	5
PETN	0	–5	3	10	7	0	–3	6	10	8
PETN	–1	–5	4	18	11	2	–1	9	14	11
RX-23-AA	4	2	11	10	6	10	8	17	15	14
RX-23-AB	1	–2	6	28	6	6	3	11	39	8
RX-23-AC	–4	2	18	18	1	1	4	17	16	8
TATB	–3	–14	–9	–7	–9	0	–12	–3	–8	–7
TNT	–5	–12	–8	0	–3	1	–7	4	–3	2
Average	–4	–5	–1	7	2	0	–1	6	8	6
Stdev	6	8	8	10	7	5	8	6	11	6

Table 8-4. Product compositions from TIGER, CHEQ, and calorimeter measurement. The sequence in time is the C-J point, the 1800-K freeze, and the unfrozen 1-atmosphere equilibrium point. The latter two are on the Principal Adiabat. CHEQ gives the phase of carbon as diamond (d), graphite (g), and liquid (l). All units are in mol per mol of initial explosive.

			Product concentration (mol/mol)					
Condition			CO	CO_2	C	CH_4	H_2O	N_2
PETN	C-J	BKWR	1.8	3.2	0.0	0.0	3.9	1.9
1.74	C-J	CHEQ	0.4	4.0	0.6(d)	0.1	3.7	1.9
g/cc	freeze 1800 K	BKWR	1.2	3.7	0.0	0.1	3.4	2.0
	freeze 1800 K	CHEQ	1.6	3.4	0.0	0.0	3.6	2.0
	calorimeter	**measd**	**1.6**	**3.3**	**0.0**	**0.0**	**3.5**	**2.0**
	eqm 1 atm	CHEQ	0.0	4.4	0.2(g)	0.3	3.2	2.0
	eqm 1 atm	BKWR	0.0	4.5	0.0	0.5	3.0	2.0
BTF	C-J	BKWR	0.4	2.8	2.8	0.0	0.0	3.0
1.86	C-J	CHEQ	0.8	2.6	2.6(l)	0.0	0.0	3.0
g/cc	freeze 1800 K	BKWR	3.1	1.4	1.4	0.0	0.0	3.0
	freeze 1800 K	CHEQ	3.9	1.1	1.1(g)	0.0	0.0	3.0
	calorimeter	**measd**	**2.9**	**1.6**	**1.6**	**0.0**	**0.1**	**2.9**
	eqm 1 atm	CHEQ	0.6	1.7	2.7(g)	0.0	0.0	3.0
	eqm 1 atm	BKWR	0.0	3.0	3.0	0.0	0.0	3.0
TATB	C-J	BKWR	0.6	1.3	4.1	0.0	2.7	2.9
1.83	C-J	CHEQ	0.0	1.6	4.4(d)	0.0	2.8	2.9
g/cc	freeze 1800 K	BKWR	0.3	1.6	4.1	0.0	2.7	2.9
	freeze 1800 K	CHEQ	0.8	1.5	3.6(g)	0.2	2.3	2.9
	calorimeter	**measd**	**0.4**	**2.0**	**3.6**	**0.0**	**2.1**	**2.3**
	eqm 1 atm	CHEQ	0.0	1.7	4.1(g)	0.2	2.6	3.0
	eqm 1 atm	BKWR	0.0	3.0	1.5	1.5	0.0	3.0

Table 8-5. CHEQ runs on TATB with different phase combinations. The carbon is either in mixed equilibrium or has been constrained to be pure diamond or pure graphite. The mixed carbon runs have been done with one or two phases of nitrogen and water. the differences between the carbon phases can be measured; the differences in N_2-H_2O cannot.

Carbon	N_2-H_2O	P_{cj}	T_{cj}	E_d (kJ/cc)		
phases	phases	(GPa)	(K)	v = 1. 2	v = 2.2	v = 6.5
Mixed	Two-phase	26.4	3280	2.58	5.00	6.16
Diamond	Two-phase	26.4	3280	2.54	4.84	6.03
Graphite	Two-phase	29.7	3170	2.78	5.14	6.26

N_2-H_2O	Carbon	P_{cj}	Temp.	E_d (kJ/cc)		
phases	phases	(GPa)	(K)	v = 1. 2	v = 2.2	v = 6.5
Two-phase	Mixed	26.4	3280	2.58	5.00	6.16
One-phase	Mixed	28.4	3091	2.60	5.00	6.15

Table 8-6. L. Haselman's CHEQ-based Look-Up Tables for the adiabats of LX-14 and LX-17. Pressure is in Mbars, energy in Mbar·cc/cc, detonation velocity in mm/μs, and density in g/cc. The adiabat point is in boldface. η is the inverse of v. Sub-a refers to the adiabat detonation point.

LX-14, Table no. TL

		P_a	0.3324	D	0.8815
		v_a	0.7669	ρ_o	1.835
		γ_a	3.2896	E_o	0.100
		E_a	0.1387		

v	η	γ	P_s (Mb)	E_s (Mb·cc /cc)	f
0.5000	2.00	3.51	1.4681	0.3317	2.2128
0.5263	1.90	3.51	1.2275	0.2964	2.1799
0.5556	1.80	3.52	1.0162	0.2637	2.1408
0.5882	1.70	3.52	0.8318	0.2336	2.0942
0.6250	1.60	3.51	0.6723	0.2061	2.0385
0.6667	1.50	3.51	0.5362	0.1811	1.9740
0.6897	1.45	3.46	0.4762	0.1695	1.9376
0.7143	1.40	3.39	0.4218	0.1584	1.9014
0.7407	1.35	3.31	0.3728	0.1479	1.8666
0.7669	**1.3040**	**3.29**	**0.3324**	**0.1387**	**1.8373**
0.7692	1.30	3.27	0.3291	0.1380	1.8347
0.8000	1.25	3.20	0.2895	0.1285	1.8028
0.8333	1.20	3.15	0.2541	0.1194	1.7732
0.8696	1.15	3.13	0.2222	0.1108	1.7438
0.9091	1.10	3.12	0.1934	0.1026	1.7131
0.9524	1.05	3.12	0.1673	0.0948	1.6799
1.0000	1.00	3.13	0.1437	0.0874	1.6433
1.0526	0.95	3.17	0.1224	0.0805	1.6013
1.1111	0.90	3.20	0.1032	0.0739	1.5511
1.1765	0.85	3.21	0.0860	0.0677	1.4934
1.2500	0.80	3.18	0.0708	0.0620	1.4280
1.3333	0.75	3.10	0.0577	0.0567	1.3587
1.4286	0.70	2.99	0.0467	0.0517	1.2896
1.5385	0.65	2.87	0.0375	0.0471	1.2234
1.6667	0.60	2.76	0.0298	0.0428	1.1607
1.8182	0.55	2.64	0.0235	0.0388	1.1008
2.0000	0.50	2.53	0.0183	0.0350	1.0451
2.2222	0.45	2.41	0.0141	0.0315	0.9931
2.5000	0.40	2.29	0.0106	0.0281	0.9465
2.8571	0.35	2.17	0.0079	0.0248	0.9056
3.3333	0.30	2.05	0.0057	0.0216	0.8710

LX-17, Table no. L15

		P_a	0.255	D	0.7600
		v_a	0.7676	ρ_o	1.900
		γ_a	3.3037	E_o	0.069
		E_a	0.0986		

v	η	γ	P_s (Mb)	E_s (Mb·cc /cc)	f
0.5000	2.00	3.90	1.2813	0.2564	2.4991
0.5263	1.90	3.90	1.0471	0.2259	2.4400
0.5556	1.80	3.90	0.8461	0.1983	2.3702
0.5882	1.70	3.85	0.6773	0.1736	2.2953
0.6250	1.60	3.80	0.5363	0.1514	2.2143
0.6667	1.50	3.75	0.4196	0.1316	2.1258
0.6897	1.45	3.70	0.3698	0.1225	2.0814
0.7143	1.40	3.60	0.3257	0.1140	2.0406
0.7407	1.35	3.45	0.2871	0.1059	2.0077
0.7676	**1.3027**	**3.3037**	**0.2550**	**0.0986**	**1.9848**
0.7692	1.30	3.25	0.2533	0.0982	1.9835
0.8000	1.25	2.90	0.2231	0.0909	1.9631
0.8333	1.20	2.70	0.1981	0.0839	1.9681
0.8696	1.15	2.50	0.1765	0.0771	1.9901
0.9091	1.10	2.20	0.1577	0.0705	2.0325
0.9524	1.05	4.20	0.1419	0.0640	2.1094
1.0000	1.00	4.25	0.1159	0.0579	1.9998
1.0526	0.95	4.20	0.0934	0.0525	1.8748
1.1111	0.90	2.50	0.0747	0.0476	1.7440
1.1765	0.85	4.00	0.0646	0.0430	1.7677
1.2500	0.80	3.95	0.0509	0.0388	1.6396
1.3333	0.75	3.87	0.0396	0.0351	1.5053
1.4286	0.70	3.75	0.0304	0.0318	1.3683
1.5385	0.65	3.60	0.0231	0.0288	1.2333
1.6667	0.60	3.45	0.0174	0.0263	1.1036
1.8182	0.55	3.25	0.0129	0.0240	0.9798
2.0000	0.50	3.05	0.0095	0.0220	0.8667
2.2222	0.45	2.85	0.0069	0.0202	0.7641
2.5000	0.40	2.60	0.0050	0.0185	0.6719
2.8571	0.35	2.30	0.0035	0.0170	0.5940
3.3333	0.30	2.00	0.0025	0.0156	0.5340

Table 8-6, part 2

v	η	γ	P_s (Mb)	E_s (Mb·cc /cc)	f	v	η	γ	P_s (Mb)	E_s (Mb·cc /cc)	f
4.0000	0.25	1.91	0.0039	0.0185	0.8467	4.0000	0.25	1.75	0.0017	0.0142	0.4926
5.0000	0.20	1.77	0.0026	0.0153	0.8402	5.0000	0.20	1.55	0.0012	0.0128	0.4672
6.6667	0.15	1.66	0.0016	0.0120	0.8677	6.6667	0.15	1.4092	0.0008	0.0112	0.4575
10	0.10	1.64	0.0008	0.0083	0.9749	10	0.10	1.30	0.0004	0.0093	0.4649
20	0.05	1.97	0.0003	0.0037	1.3713	20	0.05	1.30	0.0002	0.0066	0.5033
100	0.01	3.09	0	0	4.0682	100	0.01	1.30	0.0000	0.0028	0.5851
1000	0.001		0	0	2.6853	1000	0.001	1.30	0.0000	0.0006	0.7352

Chapter 9. Composite Explosives

1. The Problem of Nonreactivity

Composite explosives are mixtures in which the combination is expected to produce a positive added result. It is common to start with a conventional CHNO explosive as the base. If this explosive is oxygen-poor, an oxidizer is added. If the explosive is oxygen-rich (which seldom happens), a reducing agent is added. A special reducing agent is a metal like aluminum that takes away oxygen from the original gaseous products and prolongs the reaction from microseconds to milliseconds. Some explosives are odd mixtures of all of these.

Special types of composites may be considered. Most notable is the industrial explosive, ANFO, which is made up of two components (ammonium nitrate and fuel oil) that do not detonate separately but do detonate when mixed. Another is a combination of two CHNO explosives with widely different properties. Finally, individual compounds like TATB act like composites in the drawn-out mode of their reaction.

For all homogeneous explosives (including TATB), we have assumed that virtually all of it detonates in the cylinder so that we may take the energy obtained in the calorimeter and use it for the initial guess in the JWL. For composites, this assumption does not work well because the explosives did not fully react. They may not have reacted because:

1. The sample was small enough, i.e., less than the "infinite diameter" sample, to have size effects.

2. The particles are so large that true mixing cannot occur at the available temperatures—even in the largest possible sample. Aluminum particles covered with an oxide layer fall into this category.

When all we have is TIGER and some cylinder data, we must somehow guess our way through these two. Looking for standards becomes the first task.

2. Cylinder Data and Infinite-Size

Various cylinder data are listed in Tables 9-1 and 9-2. Compounds have these abbreviations: Al, aluminum; AN, ammonium nitrate; AP, ammonium perchlorate; CaN, calcium nitrate; EDD, ethylene diamine dinitrate; est, estane; LiP, lithium perchlorate; KP, potassium perchlorate; PE, polyethylene; RDX, cyclotrimethylene trinitramine; V, Viton; and ZrH_2, zirconium hydride.

Calorimetry data are the cornerstone of establishing a system. Unfortunately, few composites have been run. In Table 9-1, we list the available measured total energies of detonation, E_0, with water present as vapor and the PV adjustment from the measured heat. A percent comparison with TIGER BKWR is also shown. Not one of these values is anomalously high but those below –10% are suspicious. One wonders whether or not all the explosive detonated in the calorimeter. AN/TNT mixes and EAR-1 are in this category.

Table 9-2 shows detonation velocity. The measured values are compared with those from TIGER BKWR. In bold face are the runs that may be infinite-diameter results. The first type of explosive that fits this criterion is the 100-mm copper cylinder shot in a series extending from 25 mm and where the detonation velocities appear to be converging over a narrow range. Probably a 200-mm cylinder would be a little larger, but we have no data to check. A good example is LX-17, which has never been measured above 51 mm. The comparable LANL explosive, PBX-9502, shows a higher velocity at 108 mm[1] and has been used to estimate the infinite-diameter value for LX-17.

We have taken a partial and quickly available collection of cylinder data, including measured detonation velocities—velocities at v = 2.2, 4.1, and 6.5 and the JWL total detonation energy, E_0. The percent comparison with TIGER BKWR is listed. We are looking for standards in which all numbers are within 10% of the TIGER run. The very narrow set of explosives in this group include the binary organics RX-26-AF and RX-36-AH, QM-100 (ANFO at 1.25 g/cc), QM-100R (QM-100 laced with RDX), and RX-25-BF (odd mixture with ZrH_2).

In bold face are the samples thought to be close to infinite-diameter size. There are two ways to make this determination. The first is to fire several cylinder shots of different diameter and take the result from the largest—as long as the results are similar. An example is RX-11-BD, which was run in 25-, 50-, and 100-mm sizes with all detonation velocities the same. However, both the total detonation velocity and energy are 20% below the TIGER values. Clearly, something is wrong.

The second method of obtaining the infinite size detonation velocity is to fire a huge pile of the explosive—an obviously rare occurrence. Four emulsion explosives are listed in Table 9-2 and shown in Fig. 9-1; all have extreme size effects.[2–6] All are types of ANFO (ammonium nitrate (AN) plus fuel oil). These explosives are QM-100, QM-100R, 0.8 g/cc ANFO, and RX-HD. The QM-100 pair have the AN in small particle size so that the mixture is creamy. The explosive is thought to burn easily. The ANFO and RX-HD both contain AN as prill—round pellets of 1 to 2.5 mm in diameter that look like BB pellets. The fuel oil soaks to some extent into the prill and otherwise sits outside between the grains. This kind of AN does not burn easily.

The ANFO and RX-HD have been fired in huge shots at NTS: 109 tons for the ANFO and 1400 tons for the RX-HD. The first was shot above ground;

the second was fired in a cavity in the rock. These deliver detonation velocities that surely represent infinite diameter. However, the nominal explosive density is that of the average mixture in the tank truck. When it is poured into the hole trapped air can move to the top, and a density gradient in the pile is created.

We have also used the 1800-K freeze to model our cylinder results. If a large pile of explosive is confined hotter for longer, it may well burn to equilibrium. However, the emulsion explosives burn almost totally by 1800 K in TIGER so there is little difference.

Finally, we note a common property of composites shown well by RX-04-DS. Here, the detonation velocity and total energy agree with those of TIGER. However, the energies at v = 2.2 and 6.5 are quite low—caused by the long reaction time of the composite, here, aluminum with gaseous HMX reaction products. The long reaction time appears in the Cylinder Test as a small but increasing amount of reaction, so that the slope from v = 2.2 to 6.5 is less steep for the composite than for HMX. The integral that computes energy thus covers a lot of extrapolated territory.

3. Percent Detonated in a Cylinder

A crisis arises in Table 9-2: we have no good composite standards and we cannot trust the calculations. Nevertheless, people still estimate the percent reacted. Two problems illustrate the degree of accuracy.

Consider the total detonation energy, E_0. Both the TIGER BKWR value and the cylinder value are good to no better than ±10%. For the QM-100, we have 3.6 kJ/cc from the cylinder and 3.5 kJ/cc from TIGER. In terms of energy, it all reacts, so we turn to the detonation velocities. The percent detonated in the cylinder for QM-100:

$$\% \text{ detonated } \sim D/D_\infty \sim 6.258/6.5 \sim 96\%, \qquad (1)$$

where D is the detonation velocity in the cylinder and D_∞ is the velocity at infinite diameter. Eq. (1) is for emulsions in which the components do not detonate.

The second example is more common, because it is easier to tell if only a little reacts. We consider 67.7 wt% TNM / 32/3% Al. TNM was not measured in the calorimeter, so we take the cylinder value of 3.6 kJ/cc for the total detonation energy of the pure explosive. The volume fraction for TNM is 0.75, so the TNM detonation energy in the mix is 2.7 kJ/cc. The mixture energies from the cylinder and TIGER are 10.5 and 21.4 kJ/cc. We calculate

$$\% \text{ detonated } \sim (10.5-2.7)/(21.4-2.7) \sim 42\%. \qquad (2)$$

John Kury estimates that 30 to 60% is the likely spread of the result. The calculation assumes that the TNM would have detonated even if the aluminum were inert.

4. Possible Standards

If we are describe composites in thermochemical codes, we need standards that can be fired in a cylinder no larger than 102 mm in diameter, the maximum size allowed at LLNL's Site 300. From Table 9-2, these two warrant a better look.

1. Fine aluminum in HMX with an inert binder. The RX-04-DS 50-mm samples in Table 9-2 show good agreement with TIGER, and aluminum (unlike potassium) is an easy element to run. The 25-mm-diameter aluminized samples have detonation velocities of –5% compared to TIGER, whereas at 51 mm, the velocities are –2%. Many are of the opinion that 5-μm (but not 18-μm) aluminum, if under 10 wt%, should all react.[7] However, Finger et. al. calculated the percent reacted using RUBY, an ancestor of TIGER. They found 50% reacted in 25-mm-diameter cylinders and 75% reacted in 50-mm-diameter cylinders.[8] The 50% value at 25 mm was found only after 12 μs. All this lets us hope that nearly complete reaction can be seen in a 100-mm cylinder, which seems to be the lower limit of "infinite-diameter" behavior for most composites.

2. HMX/ KP with an inert binder. The lack of a size effect in the cylinder, coupled with the lack of TIGER agreement, has already been noted. Finger et. al. found nearly complete reaction after 0.5 μs with 3-μm particles, but only 60% reaction with 10-μm particles.[8] This affect seemed to extend as far as 50 vol% KP. If we select a full burn to CO_2, then one mol of HMX reacts with one mol of KP:

$$C_4H_8N_8O_8 + KClO_4 \longrightarrow 4CO_2 + 7/2H_2O + HCl + 1/2K_2O + 4N_2 \quad (3)$$

This would amount to a 65/ 30/ 5 wt% mix of HMX/ KP/ estane, which contains more HMX than many shots. Kury believes that complete burning to CO_2 does not show as increased wall velocity because the CO_2 has more internal degrees of freedom into which energy can be funneled.

John Kury notes that the energy of detonation of HMX/ KP is no more than that of pure HMX; therefore, the oxidizing power of KP is poorly used. However, the C-J temperature of HMX of 3800 K (JCZ3) can be increased, thereby possibly assisting the reaction efficiency. The explosive with the least oxygen and the highest temperature is BTF at 5000 K. To achieve burning to CO_2, we write

$$C_6H_6O_6 + 2KClO_4 \longrightarrow 6CO_2 + 2H_2O + 2HCl + K_2O. \quad (4)$$

The mix is 45/ 50 /5 wt% BTF/ KP/ estane. Unfortunately, the theoretical energy of detonation is again calculated to be unchanged, with the oxidation just replacing the lost BTF.

5. The Need for Predictive Capability

The results of Fig. 9-1 show that not one of the four ANFO mixes can be fired in a 100-mm cylinder and get the infinite diameter result. Large, expensive, and inconvenient shots are required. This shows the need for a data compilation and code that allows the calculation of size effects and run-to-detonation distances in these materials. In the meantime, all composite cylinder shots should have the end measurement for detonation front curvature taken automatically for future reference.

6. References

1. A. W. Campbell, *Propellants, Explosives, Pyrotechnics* **9,** 183 (1984).

2. F. Helm, M. Finger, B. Hayes, E. Lee, H. Cheung, and J. Walton, *High Explosive Characterization for the Dice Throw Event,* Lawrence Livermore National Laboratory, Livermore, CA, UCRL-52042 (1976).

3. Don Larson, LLNL, private communication, 1993.

4. Reported from Alpha Explosives, LaRoche Industries, Inc., Geneva, UT.

5. Reported from Ireco, Inc., West Jordan, UT.

6. Bob Rencke, Defense Nuclear Agency, Kirtland Air Force Base, Albuquerque, NM, private communication, 1993.

7. General discussion at 10th Detonation Symposium, Boston, MA, July 12–18,1993.

8. M. Finger, H. C. Hornig, E. L. Lee, and J. W. Kury, "Metal Acceleration by Composite Explosives," *Proceedings Fifth Symposium (International) on Detonation,* Pasadena, CA, August 18–21, 1970, p. 137.

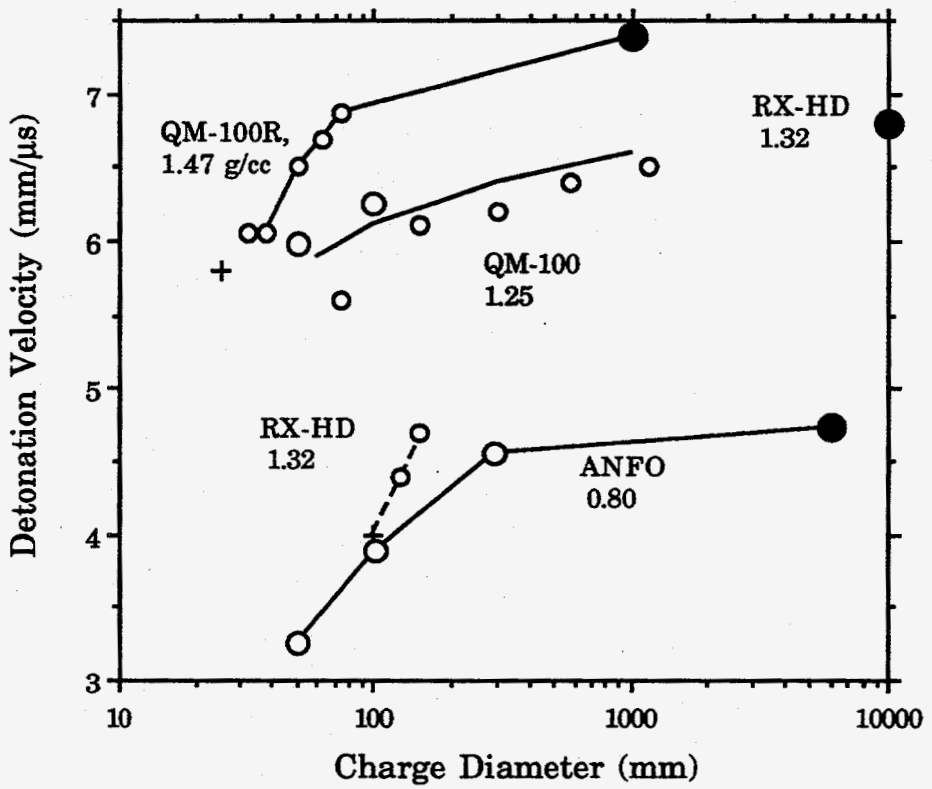

Fig. 9-1. Detonation velocity vs diameter for four emulsion explosives with extreme size effects. The curves drawn through various data points are not comparable, making prediction all but impossible. The data points indicate a bare cylinder shot without detonation (+) and with detonation (small open circles); a copper cylinder shot (large open circles); and a large-pile shot considered to represent infinite diameter (solid circles). The data points of each explosive are grouped and labeled.

Table 9-1. Comparison of total detonation energies, E_o, measured by the calorimeter and calculated by TIGER BKWR. Energies include water as the gas. An 1800-K freeze was used in the code runs.

	Explosive name	Composition wt%	Density (g/cc)	Total det energy Meas'd f. heat (kJ/cc)	Total det energy % cf. BKWR
Organic	RX-36-AA	HMX 34.56; TATB 32.21; BTF 33.23	1.813	9.5	-2
Bineries	RX-36-AF	HMX 53.51%; TATB 46.49%	1.812	9.1	0
Organic/	RX-22-AG	HMX 81.7; LP 18.3	1.91	12.4	6
Oxidizer	TNT/AN	TNT 80.3; AN 19.7	1.583	6.8	-3
	EAR	EDD 43.04; AN 41.36; RDX 15.60	1.593	6.6	-5
	EAR	EDD 43.04; AN 41.36; RDX 15.60	0.994	4.2	-3
	AN/TNT	AN 58.7; TNT 41.3	1.614	6.4	-11
	AN/TNT	AN 60.3; TNT 39.7	1.604	6.1	-13
	AN/TNT	AN 61.4; TNT 38.6	1.616	6.3	-11
	AN/TNT	AN 61.4; TNT 38.6	0.886	3.4	-6
	AN/TNT	AN 81.1; TNT 18.9	1.621	5.5	-16
Organic/	RX-04-DS	HMX 81.0: Al 9.9; Viton 9.1	1.933	12.7	-3
Reducer	TNM/Al	TNM 67.7; Al 32.3	1.828	21.2	0
	TNM/C	TNM 83; C 15; Cabosil 2	1.67	11.3	-1
Organic/	EAR-1	EDD 41.1; AN 40.9; RDX 11.9; Al 6.2	1.624	7.2	-15
Oxidizer/	RX-25-BF	HMX 37.0; AP 36.9; ZrH_2 22.1, est 4.0	2.15	11.2	-5
Reducer	RX-25-BF	HMX 37.0; AP 36.9; ZrH_2 22.1, est 4.0	2.15	11.2	-5

Table 9-2. Comparison of measured detonation velocities with the calculations of TIGER BKWR. Bold numbers are those thought to represent infinite diameter shots by (1) being the largest cylinder of a set or (2) an actual huge shot. Abbreviations are explained in the text. In each section, explosives are arranged in decreasing percent agreement with TIGER.

Categories	Name	Cylinder no.	Composition; wt%	Density (g/cc)	Diameter (mm)	Wall (mm)	Det velocity (mm/μs) Measd	% cf. BKWR
Standards	LX-14	three	HMX 95.5; estane 4.5	1.830	51	2.7	**8.80**	**0**
	LX-17		TATB 92.5; Kel-F 7.5	1.905	100	est	**7.69**	**–2**
	PBX-9502	LANL	TATB 95; Kel-F 5	1.886	108		**7.73**	**–2**
	LX-17	five	TATB 92.5; Kel-F 7.5	1.905	51	2.7	7.63	–3
	LX-17	453	TATB 92.5; Kel-F 7.5	1.913	25	1.4	7.59	–3
Organic Bineries	RX-36-AH	501	HMX 51.3; BTF 43.7; Viton 5.0	1.83	25	2.7	**8.511**	**2**
	RX-26-AF	455	HMX 49.3; TATB 46.6; estane 4.1	1.85	25	1.36	**8.241**	**–2**
	RX-26-AF	five	HMX 49.3; TATB 46.6; estane 4.1	1.844	51	2.7	**8.240**	**–2**
Organic/ Oxidizer	RX-11-BB	256	HMX 50; AP 40; Viton 10/ AP 5 μm	1.889	51	5.2	**8.119**	**–2**
	RX-34-AI	525	AP 52.8; BTF 47.2	1.824	25	2.6	7.435	–7
	RX-22-AG	253	HMX 73.6; LiP 25.4	1.988	25	2.6	8.426	–12
	RX-11-AF	239	HMX 52.3; KP 42.7; PE; 5.0/ KP 2.7 μm	1.994	50	5.2	7.757	–13
	RX-11-BA	301	HMX 53.9; NaP 41.1; est 5.0/ NaP 0.5 μm	2.009	51	5.2	7.859	–13
	RX-11-AI	240	HMX 52.3; KP 42.7; PE; 5.0/ KP 10 μm	1.985	51	5.2	7.630	–14
	RX-11-AF	238	HMX 52.3; KP 42.7; PE; 5.0/ KP 2.7 μm	1.994	25	2.6	7.629	–14
	RX-11-AJ	242, 243	HMX 52.3; KP 42.7; PE; 5.0/ KP 50 μm	1.992	51	5.2	7.499	–16
	RX-11-BD	380	KP 49.3; HMX 42.0; estane 8.7 / KP 3 μm	2.034	25	2.6	6.976	–22
	RX-11-BD	395	KP 49.3; HMX 42.0; estane 8.7 / KP 3 μm	2.095	51	5.1	7.083	–22
	RX-11-BD	384	KP 49.3; HMX 42.0; estane 8.7 / KP 3 μm	2.033	19	1.9	6.949	–22
	RX-34-AA	327	AN 60; TNT 40/ AN 5 μm	1.615	25	2.5	6.068	–23
	RX-34-AB	424	AN 60; TNT 40/ AN 25 μm	1.61	51	5.2	6.047	–24
	RX-34-AC	425	AN 60; TNT 40/ AN 200 μm	1.62	51	5.2	6.032	–24
	RX-11-BG	387	KP 60.0; HMX 31.6; estane 8.4/ KP 3 μm	2.103	19	1.9	6.394	–30

Table 9-2, part 2

Categories	Name	Cylinder No.	Composition; wt%	Density (g/cc)	Diameter (mm)	Wall (mm)	Det Velocity Measd	Det Velocity % cf. BKWR
Organic/ Oxidizer	RX-11-BG	383	KP 60.0; HMX 31.6; estane 8.4/ KP 3 μm	2.105	25	2.5	6.420	–30
	RX-11-BG	398	KP 60.0; HMX 31.6; estane 8.4/ KP 3 μm	2.093	51	5.2	6.533	–28
Organic / Reducer	TNM / Al	325	TNM 67.7; Al 32.3	1.828	51	5.2	6.010	1
	RX-04-DS	276	HMX 81; Al 10; Viton 9	1.896	51	5.2	8.525	–2
	RX-04-DS	255	HMX 81; Al 10; Viton 9	1.918	51	5.2	8.521	–3
	RX-03-EJ	457	TATB 73.9; Al 20.9; Kel-F 5.2	2.032	51	2.7	7.440	–3
	RX-04-BM	183, 184	HMX 81; Al 4; Viton 15	1.893	25	2.6	8.444	–4
	RX-04-BO	186, 206	HMX 71; Al 14; Viton 15	1.954	25	2.6	8.31	–5
	RX-04-BN	205	HMX 78; Al 7; Viton 15	1.913	25	2.6	8.411	–5
	RX-03-EK	456	TATB 83.2; Al 10.3; Kel-F 6.5	1.966	51	2.7	7.537	–5
	RX-04-BN	185	HMX 78; Al 7; Viton 15	1.953	25	2.6	8.418	–7
	TNM/C	475	TNM 82; C 15; Cabosil 3	1.722	51	5.2	6.124	–21
	TNM/C	485	TNM 81; C 15; Cabosil 3; glass 1	1.592	25	2.7	5.696	–22
Organic/ Oxidizer/ Reducer	RX-25-BF	477	HMX 37.0; AP 36.9; ZrH_2 22.1, est 4.0	2.15	51	2.7	7.506	2
	RX-25-BF	466	HMX 37.0; AP 36.9; ZrH_2 22.1, est 4.0	2.147	25	1.3	7.279	–2
	RX-25-BF	462	HMX 37.0; AP 36.9; ZrH_2 22.1, est 4.0	2.154	25	1.3	7.261	–2
	RX-03-ER	480	TATB 74.0; AP 12.4; Al 7.6; Kel-F 6.0	1.97	51	2.7	7.369	–9
	RX-03-EO	479	TATB 55.5; AP 24.8; Al 15.2; Kel-F 4.5	2.003	51	2.7	7.070	–10
	RX-31-AB	355	AN 51.7; NM 38.3; Al 10.0	1.485	51	5.2	6.277	–17
	RX-31-AA	354	NM 43.3; AN 31.7; Al 25.0	1.522	51	5.2	5.629	–21
	RX-25-AA	257	HMX 21.3; AP 59.4; Al 10; V 9.3/ AP 5 μm	1.966	51	5.2	6.538	–21

Table 9-2, part 3

Categories	Name	Cylinder No.	Composition; wt%	Density (g/cc)	Diameter (mm)	Wall (mm)	Det Velocity Measd	Det Velocity % cf. BKWR
Non-Detonable Reactants	QM-100	Alpha	AN 75; H_2O 18; fuel oil 5: glass 2	1.25	1220	bare	**6.5**	**–1**
	QM-100R	DNA	AN 44.5; RDX 40; H_2O 11; fuel oil 4.4	1.47	1400		**7.4**	**–4**
	RX-HD	NTS	AN 78.6; CaN 5.5; H_2O, 9.4; fuel oil 6.4	1.34	10000	contd	**6.8**	**–4**
	QM-100	582	AN 75; H_2O 18; fuel oil 5: glass 2	1.25	102	10.2	6.258	–5
	QM-100R	587,8	AN 44.5; RDX 40; H_2O 11; fuel oil 4.4	1.51	102	10.2	7.420	–5
	QM-100	581	AN 75; H_2O 18; fuel oil 5: glass 2	1.25	51	5.2	5.990	–9
	QM-100R	Ireco	AN 44.5; RDX 40; H_2O 11; fuel oil 4.4	1.47	75	bare	6.87	–11
	ANFO	NTS	AN 94.2; fuel oil 5.8	0.80	6000		**4.74**	**–12**
	ANFO	356	AN 94; fuel oil 6	0.84	292	29.9	4.564	–15
	ANFO	357	AN 94.2; fuel oil 5.8	0.82	292	29.9	4.553	–16
	ANFO	298	AN 94.8; fuel oil 5.2	0.78	102	10.2	3.890	–24
	ANFO	361	AN 94.2; fuel oil 5.8	0.80	51	5.2	3.252	–38

Appendix:
Composition and Grain Sizes of Explosives

We here describe the explosives considered from Chapters 2 to 8. Table A-1 lists the explosives and their components, along with their formulas, densities, molecular weights, and heats of formation.

Three particle sizes make up HMX going into LX-14-0: 65 wt% class A(1), 25% special class, and 10% class (2). Folding these together, we have roughly the following spectrum of grain size.[1,2] Large and small grains have been blended together for optimum packing.

Approx. grain size (μm)	Approx. wt %
0 to 50	18
50 to 70	6
70 to 200	18
200 to 400	23
400 to 600	23
600 to 1200	11

(1)

LX-14-0 is a mixture of HMX particles coated with a urethane polymer. HMX is present at 95.5 wt% ±0.5% for a lot and ±0.6% for a batch. The size spread of the particles ranges from 300 to 4800 μm.[3] It is generally assumed that the HMX particle size listed in the above table is reproduced in the formulation. All the LLNL copper-cylinder shots (nos. 353, 469, 510, 520, and 521) are LX-14-0.

LX-17 consists of TATB powder coated with Kel-F binder. The TATB shall be present in 92.5 wt% ±0.3% for the lot and ±0.5% for the batch. The first three columns of the table below lists the % particle size fractions of the virgin TATB used in the formulation. The last two columns list the % particle sizes in the final LX-17.[4]

Sieve size (μs)	TATB in LX-17-0	TATB in LX-17-1	Sieve size (μs)	LX-17
>45	40	25	4800–8000	1
20 to 45	25	25	3400–4800	9
<20	35	50	180–3400	87

(2)

We note that LX-17 has a much smaller and more uniform explosive particle size than LX-14.

Three LLNL cylinder shots used wet-aminated TATB in the form LX-17-1 (nos. 522, 523, and 554). The detonation front curvature shot (556) was also LX-17-1. The previous cylinder shots (349, 432, 434, 439, and 453) were RX-03-BB, the experimental form of LX-17 used before production. The metal plate shots include the dry-aminated product, LX-17-0, for the pta90000 series and the wet-aminated LX-17-1 for the others.

References

1. Military Specification, MIL-H-45444A, Amendment 3, Picatinny Arsenal, July 31, 1962.

2. Military Specification, MIL-H-48358, Amendment 2, Picatinny Arsenal, April 8, 1988.

3. *LX-14-0 Molding Powder,* Specification Sheet RM253683, Issue G, D. Duffek, LLNL FSCM No. 14067, January 20, 1984.

4. *LX-17 High Explosive Molding Powder,* Specification Sheet RM255117, Issue P, D. Duffek, LLNL FSCM No. 14067, August 13, 1985.

Acknowledgments

We would especially like to thank Al Nichols, Craig Tarver, and John Kury for their extensive help in compiling this work. Chapters 1 through 8 were written for the Nuclear Weapons Program; Chapter 9 was written for the Technical Maturation Fund. We would like to thank Mike Anastasio for his continued support of EOS.

Table A-1. Inventory of explosives mentioned in Chapters 1 to 7 of this report. Components are listed in wt%. Pure components used in mixtures are listed at the bottom. "S" indicates a solid, and "L" indicates a liquid. The formulas are rounded off to the nearest tenth. The asterisk indicates a theoretical material density.

Category of explosive	Common name	Chemical name	Formula		Density or TMD* (g/cc)	Molecular weight (g/mol)	Heat of formation (kJ/mol)
Standard	PETN	pentaerythritol tetranitrate	$C_5H_8N_4O_{12}$	S	1.78*	316.15	–538.5
often run	LX-14	95.5% HMX; estane 4.5%	$C_{1.5}H_{2.9}N_{2.6}O_{2.7}$	S	1.849	100.04	6.28
	PBX-9404	94% HMX; 3% NC; CEF 3%	$C_{1.4}H_{2.8}N_{2.6}O_{2.7}$	S	1.865	100.0	0.33
	RX-26-AF	49.0% HMX; 46.7% TATB; 4.3% estane	$C_{5.0}H_{7.0}N_{6.6}O_{6.6}$	S	1.868	265.7	–88.35
	LX-17	92.5% TATB; 7.5% Kel-F	$C_{2.3}H_{2.2}N_{2.2}O_{2.2}$	S	1.944	94.22	–100.6
Homogeneous	BTF	benzotrifuroxane	$C_6N_6O_6$	S	1.901*	252.11	601.7
	1,2-DP	1,2-bis (difluoroamino)propane	$C_3H_6N_2F_4$	L	1.26*	146.09	–200.8
	FEFO	bis (2-fluoro-2,2-dinitroethyl)formal	$C_5H_6N_4O_{10}F_2$	L	1.607*	320.1	–742.7
	FM-1	23% FEFO; 52% MF-1; 25% BDNPF	$C_6H_{9.1}N_4O_{10}F$	L	1.509*	316.07	–667.8
	HMX	octahydro-1,3,5,7-tetranitro-1,3,5,7-tetraocine	$C_4H_8N_8O_8$	S	1.905*	296.17	75.02
	HNB	hexanitrobenzene	$C_6N_6O_{12}$	S	2.02*	348.11	65.69
	HNS	2,2',4,4',6,6'-hexanitrostilbene	$C_{14}H_6N_6O_{12}$	S	1.74*	450.3	78.24
	NM	nitromethane	CH_3NO_2	L	1.13*	61.04	–113.1
	NNE	39% NM; 56% NP; 5% ED	$C_{2.0}H_{5.2}N_{1.1}O_{1.9}$	L	1.034*	74.04	–141.3
	PF	picryl fluoride	$C_6H_2N_3O_6F$	L	1.833*	231.1	–259.4
	RX-23-AA	79% hydrazine nitrate/21% hydrazine	$H_{4.5}N_{2.4}O_{1.6}$	L	1.424*	64.38	–125
	RX-23-AB	69% hydrazine nitrate/5% hydrazine/26% water	$H_{3.1}N_{1.0}O_{1.5}$	L	1.356*	43.20	–247
	RX-23-AC	32% hydrazine nitrate/68% hydrazine	$H_{4.1}N_{2.1}O_{0.4}$	L	1.136*	39.44	6.5
	RX-42-AB	60% nitric acid; 40% DNB	$C_{1.2}H_{1.6}N_{1.2}O_{3.2}$	L	1.542*	84.02	–143.8
	RX-42-AC	60% nitric acid; 30% DNB; 10% RDX	$C_{1.0}H_{1.6}N_{1.3}O_{3.3}$	L	1.56*	85.05	–141.9
	TATB	1,3,5-triamino-2,4,6-trinitrobenzene	$C_6H_6N_6O_6$	S	1.938*	258.16	–154.2
	TNGU	tetranitroglycoluril	$C_4H_2N_8O_{10}$	S	2.04*	322.1	50.21
	TNM	tetranitromethane	CN_4O_8	L	1.65*	196	54.39
	TNT	2,4,6-trinitrotoluene	$C_7H_5N_3O_6$	S	1.654*	227.13	–74.52

Note: The RX-23-AB composition lists burnable materials only, not water.

Table A-1, part 2

Category of explosive	Common name	Chemical name	Formula		Density or TMD* (g/cc)	Molecular weight (g/mol)	Heat of formation (kJ/mol)
Pure Components	ADNBF	7-amino-4,6-dinitrobenzofuran	$C_6H_3N_5O_6$	S	1.91*	241.1	153.9
	CEF	tris-b-chloroethylphosphate	$C_6H_{12}Cl_3O_4P$	L	1.425	285.5	–1255
	BDNPF	bis (2,2-dinitropropyl)formal	$C_7H_{12}N_4O_{10}$	L	1.39*	312.19	–597.1
	DNB	m-dinitrobenzene	$C_6H_4N_2O_4$	S	1.575*	168.11	–25.94
	estane	polyurethane polymer	$C_{5.1}H_{7.5}N_{0.2}O_{1.8}$	S	1.16	194.7	–773
	ED	ethylenediamine	$C_2H_8N_2$	L	0.900	60.11	–63.01
	H2O	water	H_20	L	1.00	18.015	–285.8
	HN	hydrazine mononitrate (w. 3.9% CH3OH)	$C_{0.1}H_{4.9}N_{2.7}O_{2.8}$	L	1.665	88.32	–250.2
	HNO3	nitric acid (100%)	HNO_3	L	1.5027	63.01	–173.2
	HYD	hydrazine (w. 0.7% H2O)	H_4N_2	L	1.011	31.88	46.23
	K-6	2-oxo-1,3,5-trinitro-1,3,5-triaza cyclohexane	$C_3H_4N_6O_7$	S	1.927*	236.1	–41.84
	Kel-F	chloro, fluoro-ethylene/vinylidine polymer	$C_8H_2F_{11}Cl_3$	S	2.02	413.5	–2418
	MF-1	(2-fluoro-2,2-dinitroethyl, 2,2-dinitropropyl)formal	$C_6H_9N_4O_{10}F$	L	1.534	316.16	–669.9
	NC	nitrocellulose	$C_{6.0}H_{7.3}N_{2.7}O_{10.4}$	S	1.656	283.9	–682
	NP	2-nitropropane	$C_3H_7NO_2$	L	0.988	89.09	–180.3
	RDX	hexahydro-1,3,5-tritnitro-1,3,5-triazine	$C_3H_6N_6O_6$	S	1.806*	222.1	61.55
	Viton A	vinylidine fluoride/hexafluoropropylene polymer	$(C_5H_{3.5}F_{6.5})_n$	S	1.85	(187.8)n	–1392